IKE Institut für Kernenergetik
und Energiesysteme

Numerical Investigation of the Turbulence Mass Transport during the Mixing of a Stable Stratification with a Free Jet

Armin Zirkel

September 2011 IKE 8 - 115

Universität Stuttgart

IKE Institut für Kernenergetik
und Energiesysteme

Numerical Investigation of the Turbulence Mass Transport during the Mixing of a Stable Stratification with a Free Jet

von der Fakultät Energie-, Verfahrens-
und Biotechnik der Universität Stuttgart
zur Erlangung der Würde eines
Doktor-Ingenieurs (Dr.-Ing.)
genehmigte Abhandlung

vorgelegt von

Dipl.-Ing. Armin Zirkel

geboren in Stuttgart.

Hauptberichter: Prof. Dr.-Ing. E. Laurien

Mitberichter: Prof. Dr.-Ing. S. Riedelbauch

Tag der Einreichung: 13.12.2010

Tag der mündlichen Prüfung: 11.05.2011

ISSN – 0173 – 6892

September 2011 IKE 8 - 115

Universität Stuttgart

Institut für Kernenergetik und Energiesysteme

Universität Stuttgart

Pfaffenwaldring 31

70550 Stuttgart

Vorwort

Die Vorliegende Arbeit entstand während meiner Tätigkeit als wissenschaftlicher Mitarbeiter am Institut für Kernenergetik und Energiessteme der Universität Stuttgart.

Mein besonderer Dank gilt Herrn Prof. Dr.-Ing. E. Laurien, dem Leiter des Lehr- und Forschungsgebiets Thermofluiddynamik, der meine Arbeit als Hauptberichter betreute. Durch sein umfangreiches Wissen und seine gezielten Fragen konnte er mich und meine Forschung immer in die richtige Richtung lenken. Dadurch trug er maßgeblich zum Gelingen meiner Arbeit bei.

Dem Leiter des Instituts für Hydraulische Strömungsmaschinen, Herrn Prof. Dr.-Ing. S. Riedelbauch, danke ich herzlich für die Übernahme des Mitberichts. Sein Interesse an meiner Arbeit und seinen kritischen Fragen und Kommentare waren sehr hilfreich.

Des weiteren danke ich der Firma ANSYS Germany für die gute Zusammenarbeit und insbesondere Herrn Guido Döbbener für die Unterstützung zu Beginn meiner Arbeit. Außerdem danke ich Herrn Dr.-Ing. Karsten Fischer der bei der Firma Becker Technologies für die THAI-Experimente verantwortlich war und mir interessante Einblicke in die Problematik aus experimenteller Sicht ermöglichte.

Meinen Kollegen danke ich für ein ausgezeichnetes Arbeitsklima und interessante wissenschaftliche Diskussionen. Dabei möchte ich mich besonders bei Herrn Dr.-Ing. Yu Zhu bedanken, mit dem ich mir das Büro geteilt habe.

Ganz besonders danke ich meiner Frau Alexandra und meinem Sohn Arthur für ihre Unterstützung und Motivation.

Stuttgart, im September 2011

Armin Zirkel

Abstract

The safety of present and future light-water reactors is a major concern of electrical utilities, politics and research institutes.

During a severe accident, hydrogen can be produced by a chemical reaction between the Zircaloy cladding and water and escape into the containment through a leak in the primary circuit. The prediction of the mass transport of hydrogen is vital for an optimised positioning of countermeasures like recombiners. It is possible that a stable stratification of hydrogen and air occurs, due to the different densities of those fluids. This stratification can be mixed with a free jet. This mixing is characterised by the time dependency of the flow, sharp velocity and density gradients as well as the non-isotropy of Reynolds stresses and turbulent mass fluxes.

With the use of a Reynolds stress turbulence model, the non-isotropic Reynolds stresses can be simulated. A similar approach is theoretically possible for the turbulent mass fluxes, but only the isotropic eddy diffusivity model is currently available in state-of-the-art cfd-software.

The shortcomings of the eddy diffusivity model to simulate the turbulent mass flux are investigated, as well as improvements with the use of a non-isotropic model. Because of the difficulties to get experimental data of flows in real containments, the THAI experimental facility was created to get experimental data for flows in large buildings. The experiments are performed by Becker Technologies. The analysis is using the experimental data of the TH20 experiment as the reference case. For safety reasons the used light gas for the experiments is helium instead of hydrogen. Due to the rotational symmetry of the geometry as well as the boundary conditions, two-dimensional simulations are performed. The grid was built following the best practice guidelines to ensure sufficient grid quality. Several simulations were carried out to investigate the numerical error caused by spatial and time discretisation.

An analysis of the currently available turbulence models shows that the eddy diffusivity model yields a poor agreement with the experimental data. This is true regardless of the used model to calculate the Reynolds stresses. Due to the time dependency of the mixing, a comparison between different simulations is not a trivial task with the exception of the time dependent helium concentration on different measuring points. Therefore a theoretical, statistically steady, two-dimensional test case was designed to enable direct comparisons of different models. With steady state results, an investigation of velocities and turbulent values, especially the turbulent mass fluxes, is possible without the need to consider the different mixing progress of a model at a given time.

A large eddy simulation is performed as reference for the investigation of the non-isotropic turbulence scalar flux model, TSF-model for short. The new TSF-model is then used to simulate the transient mixing of the TH20 experiments. Results obtained with the new model are showing an improved mixing.

Übersicht

Die Sicherheit existierender und zukünftiger Leichtwasserreaktoren ist von großem Interesse für die Gesellschaft, sowie für Politik, Energieversorgungsunternehmen und Forschungseinrichtungen. Während eines schweren Störfalls kann Wasserstoff entstehen. Dieser wird durch eine chemische Reaktion zwischen dem Wasser, welches dem Leichtwasserreaktor als Kühlmittel dient, und dem Hüllrohrmaterial Zirkaloy der Brennstäbe produziert. Durch ein Leck im Primärkreislauf kann der Wasserstoff in den Sicherheitsbehälter des Reaktors gelangen. Da ein Gemisch von Wasserstoff und Luft explosive Eigenschaften haben kann ist die Vorhersage des Stofftransports wichtig um die Gegenmaßnahmen optimal zu positionieren. Als Gegenmaßnahmen werden Rekombinatoren verwendet, die den Wasserstoff mit Sauerstoff zu Wasser rekombinieren.

Aufgrund der Dichteunterschiede von Wasserstoff und Luft ist die Bildung einer stabilen Schichtung möglich. Es besteht dann die Möglichkeit, dass diese Schichtung durch einen Freistrahl vermischt wird. Eine derartige Vermischung ist charakterisiert durch die Zeitabhängigkeit der Stömung, scharfen Geschwindigkeits- und Dichtegradienten sowie der nichtisotropie der Reynoldsspannungen und der turbulenten Massenflüsse. Ein Reynoldsspannungsmodell hat für jede Reynoldsspannung eine eigene Transportgleichung und kann daher nichtisotrope Reynoldsspannungen in einer Simulation berücksichtigen. Ein ähnlicher Ansatz ist theoretisch auch für die Berechnung der turbulenten Massenflüsse möglich. Analog zur Herleitung der Reynoldsspannungsgleichungen lässt sich auch für jeden turbulenten Massenfluß eine eigene Transportgleichung herleiten. Dadurch könnten auch hier Nichtisotropien berücksichtigt werden.

Derzeit ist nur das Isotrope Wirbeldiffusivitätsmodel in kommerzieller CFD-Software verfügbar. Das Wirbeldiffusivitätsmodel ist ein einfaches Model zu Berechnung der turbulenten Massenflüsse, welches die Wirbelviskosität zur Berücksichtigung der Turbulenz verwendet. Daher wird der Einfluss der Turbulenz in jede Raumrichtung als gleich groß angenommen.

Da in einem Sicherheitsbehälter keine schweren Störfälle experimentell untersucht werden können wird ein im Vergleich zu den Dimensionen eines realen Sicherheitsbehälters kleines Modell-Containment zur Durchführung von Experimenten verwendet. Die Messwerte, die für diese Arbeit verwendet werde kommen aus der THAI Versuchsanlage die von Becker Technologies betrieben. Das relevante Experiment ist THAI-TH20.

Aufgrund der Größe der Versuchsanlage und der langen Versuchszeit sind CFD-Simulationen des TH20-Experiement teuer und Ressourcenintensiv. Außerdem sind detaillierte Messwerte nur für die Heliumkonzentration an verschiedenen Messpunkten verfügbar. Geschwindigkeitsmessungen sind nur begenzt verfügbar. Messungen turbulenter Größen wie den turbulenten Massenflüsse sind gar nicht vorhanden. Daher ist dieses Experiment nicht besonders gut zu Turbulenzmodellierung geeignet.

Als Lösung für die Probleme des Experiments bezüglich der Turbulenzmodellierung wird ein theoretischer, zweidimensionaler, stationärer Testfall verwendet. Das Design dieses Testfalls wir diskutiert und mittels einer Dimensionsanalyse validiert.

Als Referenz für die Simulationen mit Turbulenzmodellen wird eine Large Eddy Simulation verwendet. Der Vorteil dieses Vorgehens ist die Möglichkeit eines detaillierten Einblick in alle relevanten physikalischen Größen. Das Konzept der Large Eddy Simulation für statistisch stationäre Probleme ist Stand der Technik und liefert physikalisch korrekte Ergebnisse wenn bestimmte Qualitätsanforderungen bezüglich des Rechengitters oder des Zeitschritts eingehalten werden. Die Qualität der räumlichen und zeitlichen Diskretisierung der hier verwendeten Large Eddy Simulation wird mit einer Spektralanalyse gezeigt.

Mit Hilfe des Ergebnisses der Large Eddy Simulation werden zwei Modellkoeffizienten des nichtisotropen Turbulence Scalar Flux Modells (TSF Modell) untersucht. Dabei wird der Auftriebsproduktionterm und die Druck-Scher-Korrelation modifiziert. Durch diese Modifizierung kann der turbulente Massenfluß erhöht und damit die Vermischung verbessert werden.

Die Abbildung zeigt die Heliumkonzentration an einem Messpunkt des Experiments. Wie zu sehen ist kann durch die Verwendung des TSF Modells eine deutlich bessere Vermischung erzielt werden als bei Verwendung des Wirbeldiffusivitätsmodells (EDM). Die Anhand des Testfalls bestimmten modifizierten Modellkoeffizienten werden zur Simulation des TH20-Experiments verwendet. Die verbesserte Vermischung die im stationären Testfall erzielt wird kann durch die Ergebnisse der Simulation des TH20-Experiments bestätigt werden.

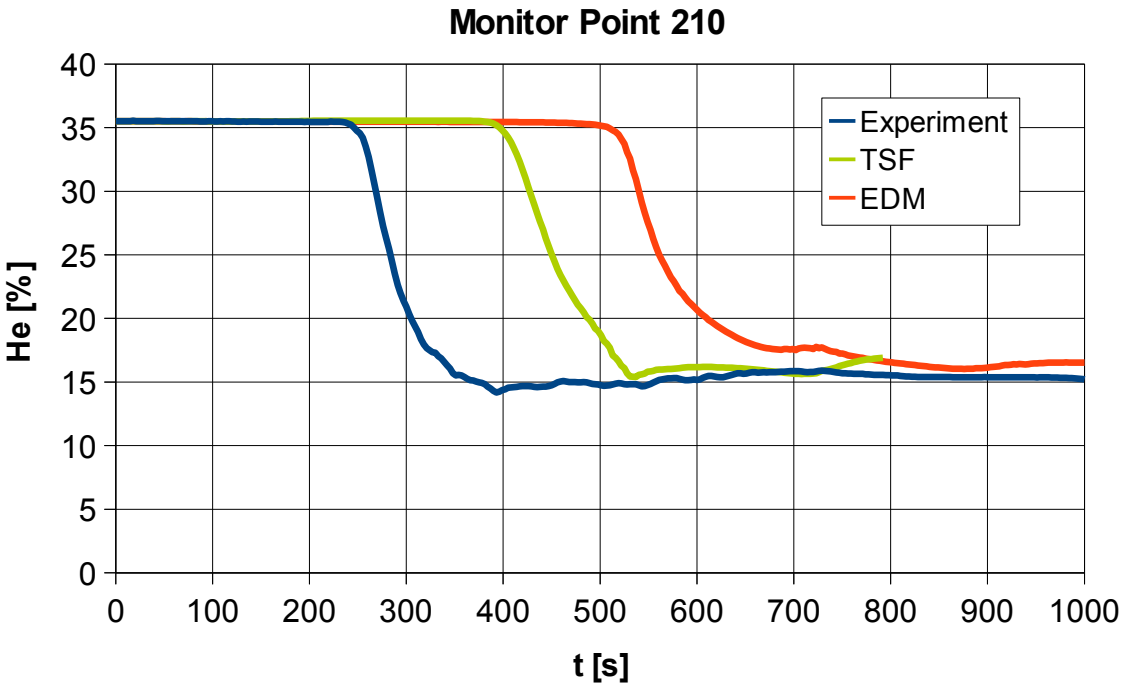

Fig. 1: Helium concentration at monitor point 210

Table of Contents

Notations and Symbols

Letters

B	buoyancy flux of the plume source $\left[\frac{kg \cdot m^2}{s^3}\right]$
C_{1Y}, C_{2Y}, C_{3Y}, C_{4Y}, C_Y, C_{YY},C_{1YY}	model coefficients of the turbulent scalar flux model
C_S	Smagorinsky constant
D	diffusion constant $\left[\frac{m^2}{s}\right]$
D_{ijk}, D_Y, D_{YY}	diffusive transport term
E	energy $[J]$
F_B	buoyant force $[N]$
f	frequency $\left[\frac{1}{s}\right]$
$f_{sig,max}$	maximum resolvable frequency of the signal $\left[\frac{1}{s}\right]$
g	gravity acceleration $\left[\frac{m}{s^2}\right]$
g_i	gravity acceleration vector $\left[\frac{m}{s^2}\right]$

G_{ij}, G_Y	buoyancy production term
k	turbulence kinetic energy $\left[\frac{m^2}{s^2}\right]$
k	wave number $\left[\frac{1}{s}\right]$
L	length $[m]$
M_f	momentum flux of the fountain $\left[\frac{kg \cdot m}{s^2}\right]$
N(u)	result of the subtraction of the of the Favre-averaged momentum equation from the original momentum equation
p	pressure $\left[\frac{N}{m^2}\right]$
P_{ij}, P_Y, P_{YY}	stress production term
Q_E	volume flux of the entrainment $\left[\frac{m^3}{s}\right]$
Q_{EU}	volume flux of the entrainment and fluid from the upper layer $\left[\frac{m^3}{s}\right]$
Q_f	volume flux of the fountain $\left[\frac{m^3}{s}\right]$
Q_{out}	volume flux leaving the tank $\left[\frac{m^3}{s}\right]$
Q_p	volume flux of the plume $\left[\frac{m^3}{s}\right]$

S_{ij}	deformation tensor
t	time $[s]$
T	time interval $[s]$
V_f	fluid volume $[m^3]$
u	velocity $\left[\frac{m}{s}\right]$
U_{up}	value of the upwind point
U_{ip}	value of the integration point
x, y, z	spatial coordinate

Dimensionless Numbers

Ar	$\frac{\Delta \rho \cdot g \cdot L^3}{\rho \cdot \nu^2}$	Archimedes number
Re	$\frac{L \cdot u}{\nu}$	Reynolds number
Ri	$\frac{g \cdot L}{u^2}$	Richardson number
Sc	$\frac{\nu}{D}$	Schmidt number

Notation Symbols

$\bar{}$	time averaged value
$\tilde{}$	Favre averaged value
$'$	fluctuating value, Reynolds averaging
$''$	fluctuating value, Favre-averaging
$\hat{}$	grid-scale value

Greek

β	volumetric expansion coefficient	
β	Blending factor	
ϵ	turbulence eddy dissipation	$\left[\frac{m^2}{s^3}\right]$
ϵ_{ij} , ϵ_{YY}	dissipation tensor	
Π_{ij} , Π_{Y}	pressure strain correlation	
ω	turbulence eddy frequency	$\left[\frac{1}{s}\right]$
$\tilde{\Phi}_i$	turbulence mass flux	$\left[\frac{m}{s}\right]$
φ	Helium mass fraction	
$\tilde{\tau}_{ij}$	Reynolds stress tensor	$\left[\frac{N}{m^2}\right]$

μ	dynamic viscosity	$\left[\frac{kg}{m \cdot s}\right]$
ν	kinematic viscosity	$\left[\frac{m^2}{s}\right]$
λ	molecular diffusivity	$\left[\frac{m^2}{s}\right]$
ρ	density	$\left[\frac{m}{s^2}\right]$
σ_t	turbulent Schmidt number	
ψ	vector from the upwind point to the integration point	
Δ	Laplace operator	
Δ	grid size	
Δ	difference	
∇	Nabla operator	

Subscripts

Air	air
exp	experimental case
He	helium
h	horizontal
i, j, k	indices of the tensor notation
max	maximum value
LES	value obtained with a LES
Mix	helium-air mixture

r, ref	reference
stat	static
steady	steady case
t	turbulent value
TSF	value obtained with the turbulence scalar flux model

Abbreviations

CCL	CFX Command Language
CFD	Computational Fluid Dynamics
DNS	Direct Numerical Simulation
EBR	Experimental Breeding Reactor
ECORA	Evaluation of Computational Fluid Dynamics for nuclear Reactor Application
EDM	Eddy Diffusivity Model
ISP	International Standard Problem
LDA	Laser Doppler Anemometry
LES	Large Eddy Simulation
LOCA	Loss of Coolant Accident
LP	Lumped Parameter
LWR	Light-Water Reactor
PIV	Particle Image Velocimetry
RANS	Reynolds Averaged Navier Stokes
RSM	Reynolds Stress Model
SGS	subgrid-scale
SST	Shear Stress Transport
THAI	Thermo-hydraulics, Hydrogen/Helium Aerosol, Iodine
TSF	Turbulence Scalar Flux
UPHI	Turbulence Mass Flux
VVER	Water Water Energy Reactor

1 Introduction

The use of nuclear fission as an electric energy source started on 20.12.1951 in Idaho, United States, where the experimental breeding reactor EBR1 produced enough electricity to light four light bulbs [1]. In 2009, about 13% of the electricity worldwide was produced by nuclear energy in 437 reactors [2]. The total generated power of those reactors was 391.5 GWe. To meet the rising energy demands while reducing the emission of greenhouse gas, new reactors are under construction all over the world. At the end of 2009, 52 reactors in 14 countries were under construction. This is a new installation of 51.2 GWe. The most important reactor type is the light-water reactor. 359 of the 437 reactors worldwide are light-water reactors. In 2009, the construction of nine new reactors started, all of them are light-water reactors [3].

The possibility of a climate change due to an increased concentration of greenhouse gas in the atmosphere is a major global concern. The reduction of greenhouse gas emission combined with an increasing demand of energy in the future makes the expansion of secure and reliable energy sources with low greenhouse gas emission necessary. Nuclear energy generation meets all those criteria. Unlike wind or solar energy it can produce with full capacity independent on environmental influences. The greenhouse gas emission per kilowatt-hour of the total nuclear energy production chain is among the lowest, even compared to renewables [4]. On the other hand, the problem of nuclear waste exists and no final solution has been found yet.

However, the safety of nuclear power generation is discussed controversially. Two major accidents happened at nuclear power stations in the past. On 28 March 1979 a loss of coolant accident (LOCA) at the Three Mile Island Nuclear Generating Station in Harrisburg, a light-water reactor, caused a partial melt-down of the reactor core. On 26 April 1986 a reactivity accident in Chernobyl caused the explosion of the reactor. The Chernobyl reactor is a water-cooled and graphite-moderated reactor without containment. After the accident in Chernobyl no serious accidents or significant radiation exposure to workers or the public have occurred for almost 25 years [5]. But on 11 March 2011 an earthquake and the following tsunami caused a serious accident in four of the six reactors of the Fukushima Daiichi power plant in Japan.

Nuclear power generation can nevertheless be considered a very safe technology if the design and the operation of the power plant is performed accordingly. An accident similar to Chernobyl is physically not possible in a light-water reactor of 'western' type, due to a negative void coefficient [6]. The Three Mile Island accident showed, that the safety systems worked very well to protect the environment and many important lessons have been learned to improve the safety of light-water reactors [7]. The accident in Fukushima is not totally investigated and understood yet, but it appears that the dimensioning of the tsunami protection

walls was very insufficient.

So, a LOCA is possible and many investigations have been performed to prevent or control a LOCA and therefore to ensure and improve the safety of nuclear power plants. Because of the seriousness of a LOCA, those investigations are continuously repeated with new methods and technology and new investigations are started.

1.1 Motivation

During a severe accident in a light-water reactor, hydrogen can be produced by a chemical reaction between the Zircaloy cladding and water, $Zr + 2H_2O \rightarrow ZrO_2 + 2H_2$.

The hydrogen can then escape into the containment through a leak in the primary circuit. The presence of hydrogen can lead to combustion processes which is a potential danger for the integrity of the containment. The prediction of the mass transport of hydrogen is vital for an optimised positioning of countermeasures like recombiners.

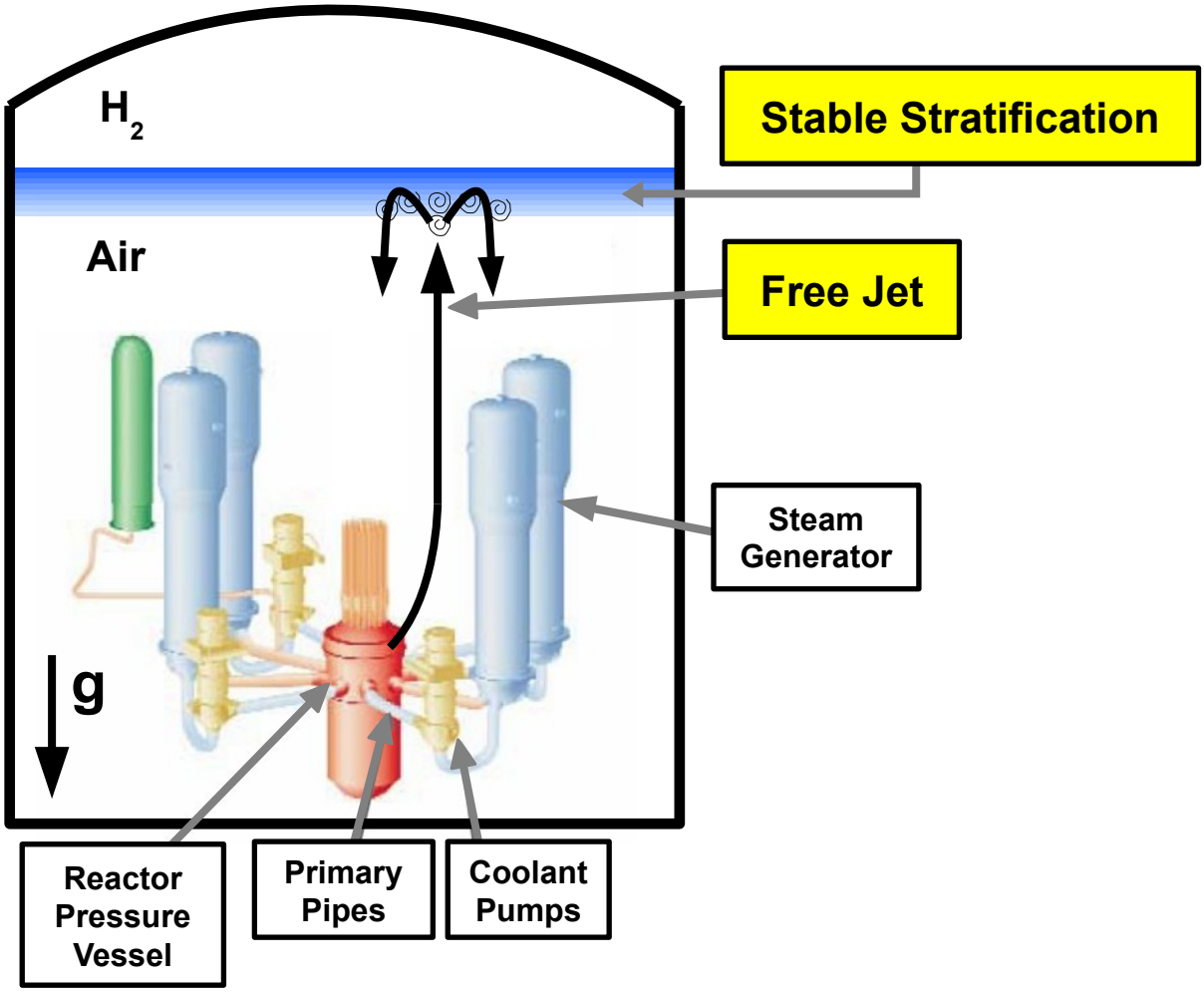

Fig. 2: Stable Stratification inside a Containment

Lumped parameter (LP) codes have been developed, verified and used to analyse and predict transport processes within a containment [8][9]. These models are based on mass and energy budgets between given control volumes inside a containment building. They can provide valuable information about complex flows, such as mixing, condensation and aerosol transport. However, flow models are often specialised to a narrow range of application and the user influence is rather large. This includes, but is not limited to, numerical parameters and calculation grids. Recently, methods of computational fluid dynamics (CFD) have also been used to simulate containment flows [10][11]. They are based on temporally averaged mass, momentum and energy conservation equations, which appear as a set of coupled partial differential equations.

The international standard problem 47 (ISP-47) has the main objective to evaluate the capability of LP and CFD codes to predict the hydrogen distribution under LOCA conditions [12]. A possible distribution of hydrogen and air is a stable stratification, due to the different densities of those fluids (Fig. 2). This stable stratification can then be mixed by a free jet caused by a leak in the primary circuit.

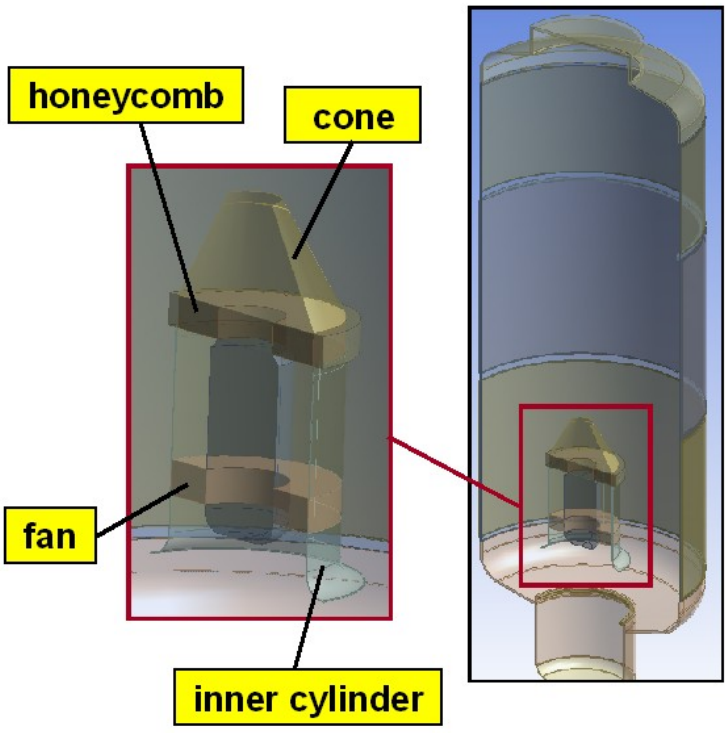

Fig. 3: Model of the TH20 configuration of the THAI vessel

The gathering of experimental data of this processes in a real containment is not easily accomplished. Therefore a model containment is used to realise measurements of mixing processes in large buildings. The TH20 experiments were performed in the THAI testing

facility to investigate the mixing of a stable stratification with a free jet, as described above [13]. The abbreviation THAI stands for Thermal-hydraulics, Hydrogen/Helium, Aerosol, Iodine. Fig. 3 shows a 3D model of the TH20 configuration of the THAI vessel.

The height of the vessel is 9.2 m and the diameter is 3.2 m. A fan is located in the inner cylinder to generate the free jet. Honeycomb and cone were installed to reduce the influence of the fan on the jet concerning radial and circumferential velocities as well as swirl.

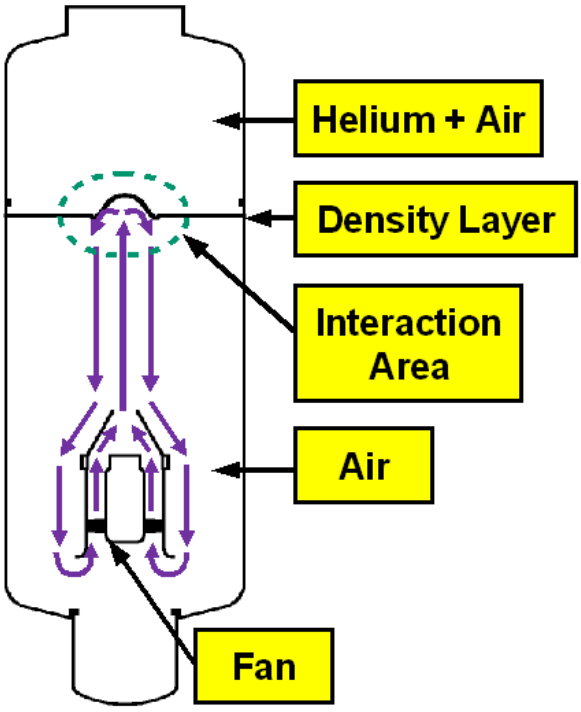

Fig. 4: Scheme of the TH20 experiment

Before the actual experiment, helium is carefully injected to form a light gas cloud of helium and air in the upper vessel. Helium is chosen as a replacement for hydrogen due to safety reasons. Because the fluid with the lesser density is on top of the denser fluid, the stratification is stable. After the injection is concluded, the fan starts to generate the free jet. It tries to penetrate the light gas cloud, but due to the stability of the stratification it is redirected instead. This happens in the interaction area, see Fig. 4. During the redirection process, the jet intakes helium and is slowly eroding the stratification. The mixing of a stable stratification with a free jet is characterised by the time dependency of the flow, sharp velocity and density gradients as well as the non-isotropy of Reynolds stresses and turbulent mass fluxes.

The outcome of the ISP-47 was that the currently available turbulence models are not capable to predict this non-isotropic mixing process. Fig. 5 shows a representative comparison of the helium mixing in the upper vessel between experiment and simulation.

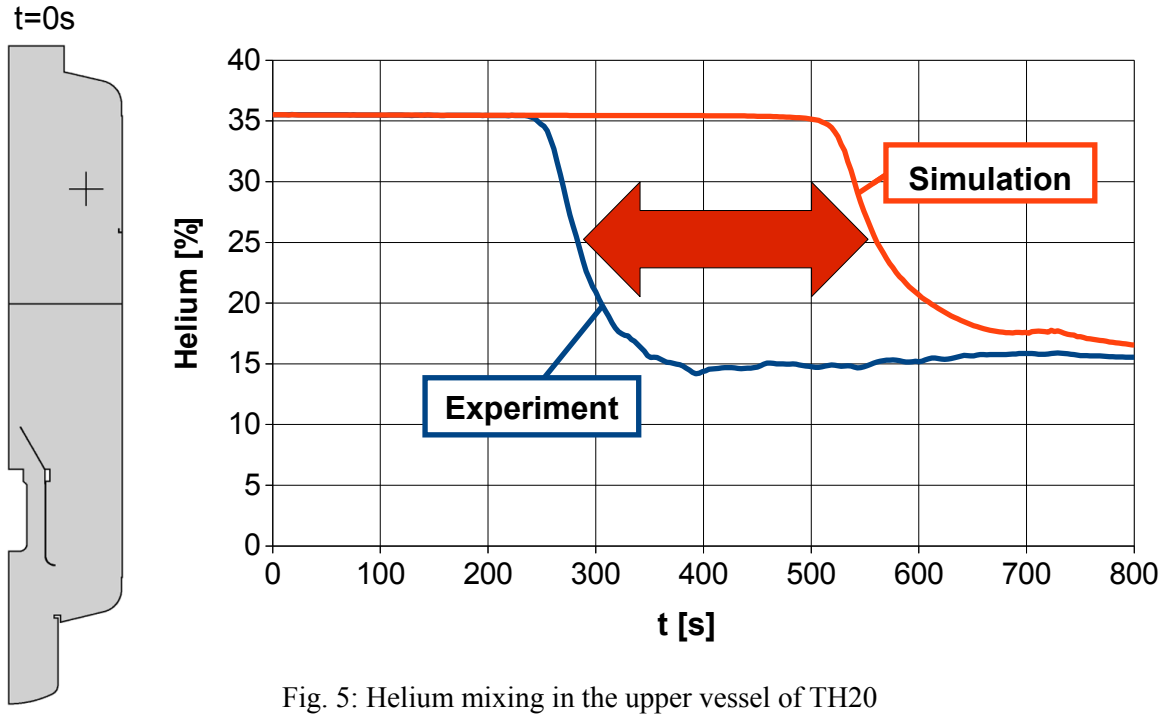

Fig. 5: Helium mixing in the upper vessel of TH20

The assumed shortcoming of the available models is the absence of a sufficient treatment of the non-isotropy of the turbulent scalar fluxes. While the Reynolds stress models (RSM) are capable to consider non-isotropic Reynolds stresses, they still use an isotropic eddy viscosity model to calculate the turbulent scalar fluxes.

1.2 State of Research and Development

In this chapter, the state of research and development concerning containments, stably stratified flows and free jets will be discussed. The chapter about the investigation of containment flows is arranged according to the experimental facility. Many investigations of stable stratifications and free jets have been done for containment flows. They will be discussed in the chapter about containment investigations with the corresponding experimental facility if applicable and not in the chapters about free jet or stable stratification investigation.

1.2.1 Investigation of Containments

The containments of nuclear reactors have been the subject of several investigations. There are four important experimental facilities in Europe to get experimental data for flows in large buildings. The TOSQAN (Fig. 6, left) and MISTRA (Fig. 6, right) experimental facilities have been used for step one of the ISP-47 [12].

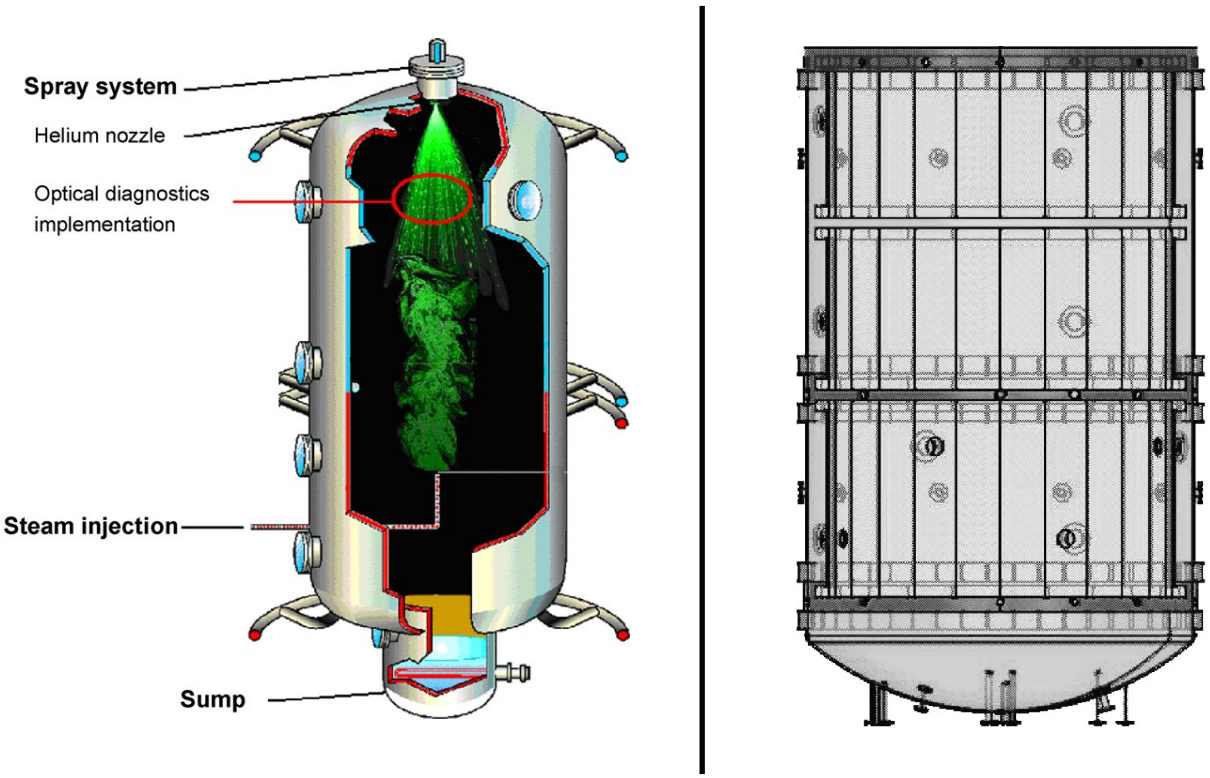

Fig. 6: TOSQAN (left) and MISTRA (right) experimental facilities ([29], [28])

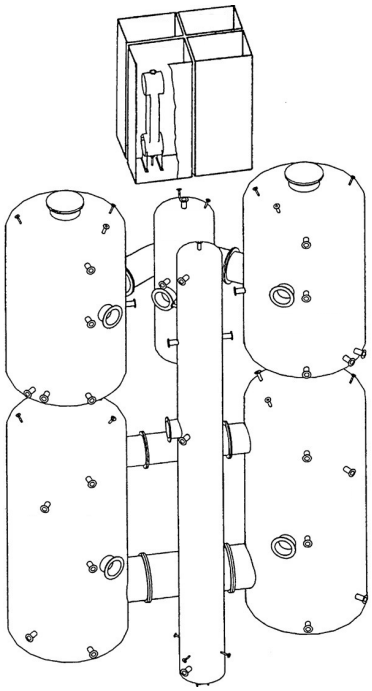

Fig. 7: PANDA experimental facility [23]

The TOSQAN model containment is a cylinder with a volume of 7 m³ made of stainless steel. The temperature of the wall can be controlled. The top and bottom parts of the wall, called the hot wall, can be heated and have the same temperature. The middle part, called the cold wall, is used as a condensation area and can have different lower temperatures. 14 windows are installed to enable visual measurement techniques like Particle Image Velocimetry (PIV) or Laser Doppler Anemometry (LDA). Temperature measurement is realised through 90 thermocouples fixed on steel rods.

MISTRA is also a cylindrical stainless steel vessel, but with a volume of 99.5 m³, a height of 7.3 m and a diameter of 4.25 m. Three different condensers are installed at various heights. Step two of ISP-47 used the THAI experimental facility, a steel vessel with a volume of 60 m³, which is described in chapter 1.1 (Fig. 3).

The fourth large scale testing facility is called PANDA (Fig. 7). It was originally designed and used to investigate containment system behaviour of advanced LWR designs of General Electric [14]. PANDA consists of six different cylindrical pressure vessels with a total volume of 460 m³. It is designed for 10 bar and 200 °C maximum operating conditions. Water, steam or gas can be added or removed to any of the six vessels.

The PANDA facility was used by Zboray and Paladino [14] to perform a series of 24 experiments concerning basic gas transport and mixing phenomena. This includes flow configurations where the gas transport is driven by a plume or jet injection of superheated or saturated steam. The experiments have been designed as validation cases for simulation tools to predict those phenomena and have well defined initial and boundary conditions.

In an earlier experiment, Paladino et al. [15] used the PANDA facility to investigate the mixing and stratification induced by a three-gas mixture plume. For the first part of this experiment, the PANDA vessels have been filled with air followed by an injection of a helium-steam mixture. In the second part, only steam was injected. The resulting flow showed complex structures consisting of free rising plumes, change from a buoyant plume to a negative buoyant plume, multi layer stratifications and more.

Another PANDA experiment for code validation carried out by Paladino [16] was aimed to investigate the behaviour of large-scale gas mixing, stratification and transport, driven by low momentum buoyant steam plumes. The plumes are rising near the wall. Two cases have been investigated. In the first case, the injected steam remained superheated during the experiment. In the second case, condensation was allowed. Both tests are characterised by the same initial Froude number.

Bandurski et al. [17] investigated the influence of the distribution of non-condensible fluids, e.g. hydrogen or helium, on the performance of passive containment condensers in PANDA. Gas mixing and stratification have been examined in this experiment. It was found, that the non-condensible fluids can accumulate in suitable regions due to gas stratification.

Simulations of basic gas mixing tests with condensation in the PANDA have been carried out by Andreani [18] using the GOTHIC code. Three of the tests featured vertical injection and one test was performed with a horizontal jet. The injected fluid was either saturated steam or a superheated mixture of steam and helium. The initial fluid in the vessel was air. The calculation domain was a three-dimensional representation of the PANDA facility with a

coarse grid. The results showed a partial good agreement with the experiment, but also showed the need for a grid refinement to resolve complex local flow pattern like the erosion of the interface between layers of different gas composition.

In another work, Andreani and Paladino [19] investigated the gas mixing and transport in the PANDA facility. The used software was GOTHIC with coarse grids. The investigated flow phenomena are the flow structures in the injection vessel, the building of a stratification in the injection vessel, the inter-compartment gas transport and the building of a stratification in the connected vessel. The injection of the steam/air or steam/helium mixture was done by near-wall injection, central vertical injection or with a horizontal jet. The outcome of this analysis was that GOTHIC can be used with confidence with coarse grids to predict flows in large buildings. However, this approach is not sufficient to predict the erosion of stratifications with an impinging jet. This is consistent with the work mentioned before [18]. In both cases the use of the GOTHIC code on a coarse grid shows a weakness to predict the behaviour of a stratified flow.

Auban et al. [20] focused their experimental work on gas mixing and stratification on two buoyant free jets, which are horizontally injected into a PANDA vessel. The initial and boundary conditions are well defined to make the experiments relevant for code validation.

Scheuerer et al. [21] evaluated computational fluid dynamics software for nuclear reactor safety applications, which is abbreviated ECORA, to develop best practise guidelines for an efficient use of CFD for reactor safety tasks. This work was not exclusively for containment analysis. Work packages two to four evaluated CFD methods for the simulation of the primary loop. In work package six and seven the applicability of CFD methods for containment flows was evaluated and validated with selected PANDA experiments. The priority was given to low momentum horizontal injections in a vessel without condensation. The calculations have been performed with CFX-4, FLUENT and TONUS.

The ECORA best practise guidelines [22] that have been applied by Scheuerer et al. [21] give a definition of errors in CFD simulations, as well as guidelines to handle or avoid those errors. Five different error categories are discussed. The first error category is the numerical error, which consists of solution error, spatial and time discretisation error, iteration error and rounding error. The other four categories are modelling errors, user errors, application uncertainties and software errors.

Grid generation is given special attention in the best practise guidelines in order to minimise the spatial discretisation error. This includes, but is not limited to avoiding grid stretching, jumps in grid density or computational cells which are not orthogonal to the fluid flow. Finally a grid dependency study is recommended to ensure that the result does not depend on the grid. This is done by comparing results obtained on grids with significantly different numbers of cells. If the result doesn't change from a grid to a more refined grid it is grid independent because the grid has no influence on the result.

Another major issue discussed in the best practise guidelines is the selection of the turbulence model. This is not a trivial task, as the applicability of each turbulence model strongly depends on the actual flow situation. For example, the k-ε model yields better results in a free flow without wall influence and a k-ω model is better capable to predict near-wall flows. As

discussed in chapter 1.1, some problems cannot sufficiently be predicted with currently available turbulence models.

The best practise guidelines [22] have been used by Andreani et al. [23] for an benchmark exercise. Four CFD codes have been used to simulate two PANDA experiments. The used codes are ANSYS CFX4, ANSYS CFX5, ANSYS FLUENT and TONUS. The chosen PANDA experiments feature low momentum horizontal near wall steam injections into one PANDA vessel initially filled with air. It turned out that the application of the best practise guidelines in regard of grid generation greatly improved the results. But the application is resource intensive, especially the grid dependency study.

Struder et al. [24] carried out an experimental program to investigate stratification break-ups induced by mass. The experiments have been performed in the PANDA and MISTRA facilities. An aim of this project was to provide high-quality measurement data as a basis for CFD model verification. It was found that depending on the interaction Froude number, different flow regimes can be identified. Those include pure diffusive mixing, global dilution and slow erosion. It was concluded that the experiments, especially the tests LOWMA3 in MISTRA and ST1-7 in PANDA, can be regarded as a good database for CFD model verification.

Work towards a CFD-grade database was done by Paladino et al. [25]. The PANDA facility was used to create this experimental database that covers basic containment phenomena. These phenomena, like gas mixing, transport, stratification or condensation are driven in the PANDA test by large scale jets or plumes. Several simulations with GOTHIC, CFX-4 and CFX-5 have been compared to experimental data to demonstrate that the spatial and temporal resolution of the measurement grid is sufficient for CFD model verification.

During step one of the ISP-47 several CFD and lumped parameter codes have been used to simulate experiments of the MISTRA facility [26]. The first major achievement of ISP-47 step one is the demonstration of the possibility to perform repeatable measurements on certain flow phenomena. The experiments investigated the interaction between injection and wall condensation, the impact of helium on the saturation profiles of the used condensers and the transient effect of helium addition on the wall condensation. The blind calculations of this experiments showed that reasonable results can be obtained with the lumped parameter codes, given a sufficient fine nodalisation. The CFD codes have weaknesses, due to the absence of a bulk condensation model.

Tkatschenko et al. [27] concluded in their work on the MISTRA part of ISP-47, that the MISTRA facility is well designed to support further code development for containment applications. To provide relevant data for code validation, well defined boundary conditions are ensured, as well as the reproducibility of the experiments.

Povilaitis et al. [28] used the containment code system COCOSYS to simulate MISTRA experiments in which atmospheric mixing is enhanced by installed water sprays. It was investigated how different experimental parameter and modelling assumptions influence the de-pressurisation rate.

To analyse the heat and mass transfer between spray droplets and gas mixtures of air and steam or air, steam and helium, Porcheron et al. [29] performed spray tests in the TOSQAN

experimental facility, denoted TOSQAN 101 and TOSQAN 101He. Detailed measurements of droplet velocities, gas temperature, gas volume concentration or vessel pressure have been done. This data is intended to be used for CFD code development and validation. Mimouni et al. [30] used the data from TOSQAN 101 and TOSQAN 113 to implement a spray model into the three-dimensional Neptune CFD code.

TOSQAN 101 and 113 have also been used by Babic et al. [31] to investigate the influence of containment spray on the mixing of a stratified atmosphere and on atmosphere de-pressurisation with CFX4.4. As part of their investigation, they incorporated a Lagrangian droplet-tracking model into CFX4.4 by means of user defined functions. It was possible for them to get a reasonable agreement with the measured data, reproducing the non-homogeneous structure of the gas atmosphere.

In order to evaluate the effects of the spray system during a LOCA in an AP1400 containment, Kim et al. [32] used the CFD code GASFLOW to simulate the TOSQAN 101 experiment. It was found out, that the spray model implemented in the GASFLOW code can reasonably resolve a two-phase flow with steam condensation by spray droplets. The following investigation of the AP1400 containment concluded with the result that the control of the spray system during an accident is important to ensure hydrogen safety.

Another hydrogen risk analysis with CFD methods was performed by Kudriakov et al. [33]. They used several experimental data sets from the large scale facilities TOSQAN, MISTRA and THAI to validate the physical and numerical models implemented in version v2006.1 of the TONUS CFD code.

In the TOSQAN part of ISP-47 wall condensation, steam injection into air or air/helium atmospheres and buoyancy effects were measured using well-defined initial and boundary conditions [34]. Detailed gas velocity and concentration fields were obtained during this exercise. The lumped parameter and CFD codes were capable of reproducing the global thermal hydraulic part of wall condensation in the presence of non condensable gases like helium at steady state. The results for the transient stratification showed differences between codes and experimental data.

The mixing of a helium stratification with steam in the THAI testing facility was simulated by Babic et al. [35] using CFX4.4. Steam condensation on the walls was modelled as a sink of mass and energy. Sacrifices in regard of the grid quality had been made due to long simulated transients. However, the results showed a reasonable agreement with the experimental data.

A detailed investigation of the momentum transport of three-dimensional containment flows was carried out by Zirkel et al. [36]. The aim was the analysis and validation of turbulence models for flows in complex geometries with different rooms and obstacles. The underlying experiment was the THAI TH18 experiment in which the THAI vessel was separated into two rooms by the installation of a condensate tray around the inner cylinder. Following the best practise guidelines [22] a grid dependency study was performed with the result of a grid independent solution in the upper vessel. However, the flow appeared to be too complicated for state of the art CFD possibilities despite a good agreement of the SST model with the experiment in the upper vessel. It is suggested that the validation process for CFD models for complex phenomena should first focus on the correct prediction of separated effects.

While all the mentioned investigations are either for a generic containment or for European or American light-water reactors, Heitsch et al. evaluated hydrogen mitigation measures in a VVER-440/213 containment using CFD methods [37]. The VVER (Water-Water-Energy-Reactor) is a pressurised water reactor, designed in Russia. The used CFD codes were GASFLOW, ANSYS FLUENT and ANSYS CFX. It turned out that the CFD code can be successfully used for these simulations. The advantage of CFD codes over lumped parameter codes is the capability to predict the appearance of stratified flows without the necessity for predefined assumptions.

1.2.2 Investigation of Free Jets

Free jets in general are a well known kind of flow. In his book “Turbulent Jets”, Rajaratnam [38] gives a broad overview over different jets. The discussed jets are

- plane turbulent free jet
- circular turbulent free jet
- radial jet
- compound jets
- plane turbulent shear layers
- axisymetric shear layers
- circular jets with swirl
- confined jets
- jets in cross-flow
- plane turbulent wall jets
- axisymetric wall jets
- plane compound wall jets
- three-dimensional

The circular round jet or round jet is emerging from a round opening with a certain diameter, as for example the nozzle in the TH20 experiment [13]. After leaving the nozzle, the core of the jet has a region of undiminished velocity in the shape of a cone, the so called potential core (Fig. 8). The region from the nozzle to the end of the potential core is the flow development region. The region downstream of the potential core is the region of fully developed flow.

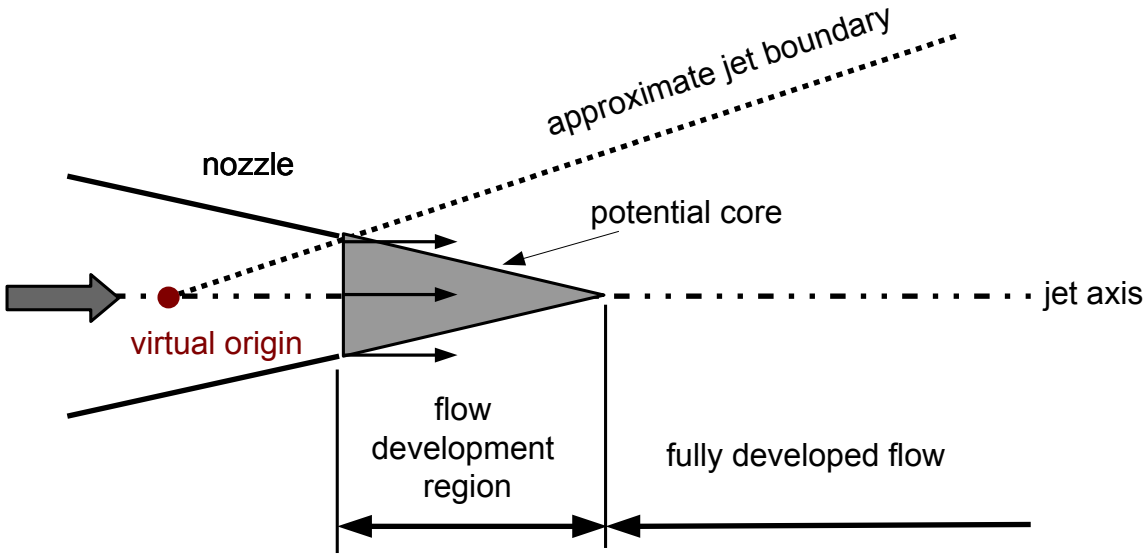

Fig. 8: Definition sketch of a round jet after [38]

The effects of initial conditions on a circular jet have been investigated by Antonia and Zhao [39]. Two jets were measured. One originated from a contraction with a laminar top hat profile, the other from a pipe with a fully developed turbulent mean velocity profile. It turned out, that both jets reach the same state of self-preservation after approximately the same development length. A possible explanation of Antonia and Zhao was, that the large-scale anisotropy is not dependent on the initial condition and therefore the same for both jets.

Xu and Antonia [40] used a smooth contraction nozzle and a long pipe as origins for their free jet measurements. The long pipe delivered a fully developed flow. Both jets had the same Reynolds number. The smooth contraction jet developed and approached self-preservation faster than the pipe jet. Different turbulent structures have been found responsible for this different behaviour of the jets.

The dependence of the near field flow of isothermal, incompressible turbulent round free jets of air on the upstream nozzle shaping was experimentally investigated by Quinn [41]. A sharp-edged orifice and a contoured nozzle have been used as origin for the jets. The Reynolds number was the same for both cases. The resulting energy spectra showed large coherent structures for both jets with greater energy in the sharp-edged orifice flow. In this case, the mixing rate was also larger.

Mi et al. [42] measured the effect of the initial condition of jet on its mixing behaviour. They used a smooth contraction nozzle, a sharp-edged orifice and a long pipe. The measurement was carried out using qualitative flow visualisation as well as quantitative measurements of the temperature on the centreline. The results showed the best mixing for the sharp-edged orifice jet and the worst mixing for the long pipe jet. This confirms the results of Xu and Quinn [40][41]. This impact of the origin of the jet is important for the modelling of the TH20 experiment.

An comprehensive investigation of a turbulent jet issuing from a sharp-edged orifice was also carried out by Mi et al. [43] using PIV measurements. They showed strongly three-

dimensional flow structures for the orifice jet. It turned out, that the upstream conditions have an influence on the exit turbulence intensity at the orifice. These influences are propagated downstream.

Malmström et al. [44] measured the centreline velocity decay in axisymmetric jets. It was examined if the diffusion of the jet depends on the outlet velocity. The investigated outlet velocity range was between 0 m/s and 12 m/s. It was found out, that the centreline velocity decay coefficient decreases with a decreased outlet velocity. This effect started below 6 m/s.

Some detailed experiments to investigate the effects of the Reynolds number on the development of a round free jet have been made by Fellouah et al. [45]. The investigated Reynolds numbers, based on the jet exit mean velocity and the nozzle diameter, are $6 \cdot 10^3$, $10 \cdot 10^3$ and $30 \cdot 10^3$. It was measured which impact the Reynolds number has on the mean velocity profiles, turbulence intensity profiles and velocity spectra. Flying and stationary hot-wire measurements have been performed. The results showed a close coupling between the mean velocity distribution, the turbulence intensity and the Reynolds shear stress. The impact of the Reynolds number varies with the region of the jet. Those effects are mostly visible in the shear layer region, where moments are high. The length of the potential core decreases with increasing Reynolds number. The downstream variation of the mean centreline velocity does not depend on the Reynolds number in the near-field.

Antoine et al. [46] measured the turbulent transport of a passive scalar in a round jet. Despite being injected into a co-flow of the same fluid, the usual velocity turbulent characteristics, like the second-order moments or Reynolds shear stresses are comparable to a free jet which is injected into a static fluid. The reduction of the jet spreading rate is the major visible impact of the co-flow as well as an enhanced mixing. The enhancement of the mixing causes higher longitudinal and radial turbulent fluxes.

A numerical study of an axisymetric turbulent jet discharging into a co-flowing stream was carried out by Mahmoud et al. [47]. The investigation comprised velocity ratios from 0 to ∞. Two different CFD-codes have been used, FLUENT 6.2 and an in-house code, to perform RANS-simulations (Reynolds-averaged Navier-Stokes). The used turbulence models are the k-ε and a Reynolds Stress (RS) model. It turned out that both models and codes were capable to reproduce average and turbulent flow sizes of underlying experimental data.

Wilkening et al. [48] investigated the mixing of a free helium jet with RANS simulations. The helium jet is released into the Battelle model containment which is filled with air. The Battelle facility has a volume of 560 m³ and the velocity of the helium jet is 42 m/s. Two different grids have been used, a pure tetrahedral grid and a finer hybrid grid with prism layers to refine the near-wall region and a better resolution of the jet. The used turbulence models are the k-ε and the shear stress transport model (SST model). The results showed a strong dependency on the used grid and turbulence model. Better agreement with the experiments could be obtained with the finer grid and the SST turbulence model. The reason for the advantage of the SST model is the use of its k-ω model in the near-wall region.

Three cases of turbulent round free jets with variable density discharging from a straight circular pipe have been studied by Wang et al. [49]. The used numerical approach was the large eddy simulation (LES). Three different fluid pairs have been used, resulting in three

density ratios. Helium/air has a density ratio of 0.14, air/air has 1.0 and carbon-dioxide/air has 1.52. The respective Reynolds numbers are $7 \cdot 10^3$, $21 \cdot 10^3$ and $32 \cdot 10^3$. The comparison of statistical quantities, e.g. streamwise velocity or radial profiles of Reynolds stress, showed a generally good agreement with the experimental data. It was further revealed that a region of strong stream-wise vorticity exists beside the shear layer region in the helium jet, but not in the CO_2 jet.

Large eddy simulations of heated and cooled plane and round jets have been performed by Foysi et al. [50]. The initial momentum flux was kept constant for all cases. Experiments and simulations showed, that the half-width of the jet grows linearly in the stream-wise direction x. Another similarity is, that the decay of the lighter jet happens faster than the decay of the heavier jet. However, the centreline velocity decay of the round and the plane jet is different. Whereas the round jet decays with $\frac{1}{x}$ for all density ratios, the plane jet seems to have two self-similar scalings, depending on the density ratio. For small density ratios or incompressible jets, the decay rate is $\frac{1}{\sqrt{x}}$. The heated jet decays with $\frac{1}{x}$ similar to the round jet.

Ranga Dinesh et al. [51] studied the intermittency in a turbulent round jet with large eddy simulations considering different inlet conditions. The quality of the LES was ensured with a comparison to experimental data. The probability density functions for the velocity and the passive scalar showed a change from a Gaussian distribution to a delta function with increased radial distance. The calculated intermittency factor showed a similar variation at different axial locations. The inlet condition was altered by the addition of a circular bluff body. This alteration changed the probability density functions of the velocity and the passive scalar. The intermittency values of velocity showed differences in the near field close to the centreline of the jet.

The capability of the large eddy simulation approach to predict a particle-laden turbulent axisymetric free jet was shown by Almeida et al.[52]. It turned out, that the effect of the carrier gas on the particles and vice versa is captured correctly by the large eddy simulation with the use of a new stochastic subgrid-scale closure. In addition to the two phase flow, large eddy simulations for a single phase jet showed a good agreement with experimental data using established subgrid-scale models.

A direct numerical simulation (DNS) of a turbulent free jet was performed by Boersma et al. [53]. Special attention was given to the boundary conditions, because the lateral boundary conditions must allow entrainment to the flow, so-called traction free boundary conditions. It was shown, that these boundary conditions lead to a correct representation of the velocity near the lateral boundary of the jet. The results yielded by a DNS with a top-hat initial velocity profile shows good agreement with experimental data. An analysis of the direct numerical simulations with two different initial conditions could not find a universal self-similarity of a jet but showed the importance of the correct scaling for the comparison of free jets.

A combined numerical and experimental investigation of hydrogen and helium jets in order to study the dynamics of transient concentration fields has been performed by Chernyavsky et al.

[54]. The underlying physical problem is the release of hydrogen from a pressurised storage tank into air at Mach numbers of ~0.3. The experiment consisted of PIV measurements of a free jet. The numerical investigation consisted of large eddy simulations, which showed good agreement with the experiment. The variance of the mass fraction at the centreline indicated strong mixing extending through the domain. Simulation and experiment showed, that exact self-similarity was not reached due to buoyancy effects.

El-Amin [55] carried out a numerical investigation of a vertical axisymetric non-Boussinesq buoyant round jet of hydrogen in air, caused by a leak in a hydrogen storage. Because a constant temperature is assumed, the density of the mixture is only a function of the concentration. The local rate of entrainment is considered to be composed of two parts, entrainment due to jet momentum and due to buoyancy. Among other quantities, like Reynolds stresses or turbulence eddy diffusivity, the turbulent Schmidt number was estimated. Also, the normal jet-feed material density and the normalised momentum flux density have been correlated.

The dependency of transient plumes and jets on the source strength was investigated by Scase et al. [56]. It turned out, that if the source momentum flux for a rising jet is decreased generically from an initial to a final value, the numerical solution contains three different regions of behaviour. The region furthest from the source remains mostly unaffected by the change in the momentum flux at the source. The region close to the source contains a steady jet based on the final momentum flux. In the transition region, a narrowing of the jet was observed, which depends on the initial condition.

1.2.3 Investigation of Stable Stratifications

A stratified flow is a phenomenon that depends on density differences and buoyancy effects. Two fluids with different densities, like cold and hot water or air and helium, can be stratified. If the lighter fluid (ρ_1) is on top of the heavier fluid (ρ_2) they form a stable stratification (Fig. 9). It is stable, because naturally the lighter fluid tends to be on top of the heavier fluid due to buoyancy.

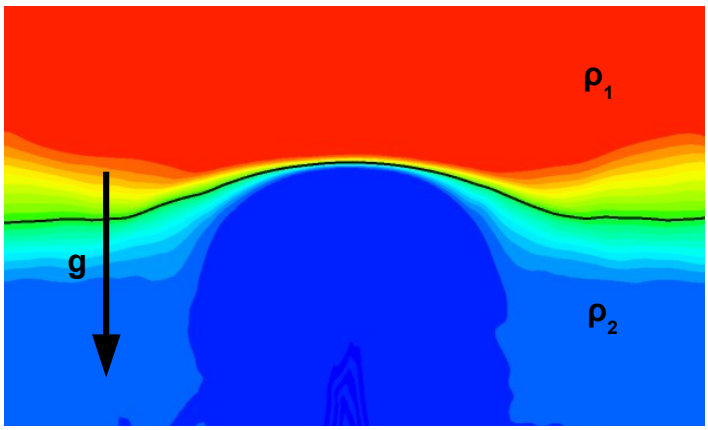

Fig. 9: Scheme of a stable stratification

An important characteristic such a stratification is its stability. It takes some effort to disturb or destroy it. If a disturbance occurs normal to the stratification, for example an impinging jet (Fig. 9), the stratification tries to restore its original shape. Another relevant characteristic is the non-isotropy associated with the stratification. The density gradient in the direction of gravity is very steep. At the same time there is almost no density gradient normal to the direction of gravity.

Density stratifications occur on very different occasions, e.g. large-scale geophysical phenomena, temperature stratifications in lakes or the forming of a light-gas cloud in the course of a loss-of-coolant accident.

Ivey et al. [57] performed laboratory-scale experiments as well as numerical calculations to investigate the turbulence mixing of density stratifications in oceans. They identified mixing due to turbulent patches that grow and decay over time. Those patches are the result of energy transport by internal gravity waves.

The interaction of a plume of warm air with a stable temperature stratification in the atmosphere above a city was investigated by Noto [58]. In laboratory-scale experiments, different flow pattern have been found. All observed flows have in common, that the stable stratification is suppressing the height of the plume and that a vortex pair is produced near the top of the plume. The flow pattern depend on the stability of the stratification and the heat rate of the plume.

Noto et al. [59] also performed a direct numerical simulation of a hot plume originating from a heated plate in a stable stratification. The quality of the DNS has been demonstrated with several energy spectra. It turned out that turbulence is suppressed at any degree of stable stratification. In a weaker stratification, turbulence is generated near the centre of the plate. But due to the suppressive effect of the stable stratification, the flow becomes laminar again. In a strong stratification the suppression of turbulence is so dominating that the flow stays laminar. Noto concluded, that the plume behaviour can be controlled with the degree of the stratification.

A stably stratified free surface open channel flow was investigated by Taylor et al. [60] with LES. The stable stratification is a result of a constant heat flux at the free surface. It was found, that a sufficient increase of the friction Richardson number, the density layer or pycnocline can change from turbulent to laminar. Another effect of the increase of the friction Richardson number is the increase of the bulk Reynolds number as well as a strengthening of the pycnocline.

The effect of the gradient Richardson number on a stable stratification as a measure of flow laminarisation was investigated by Galperin et al. [61]. It turned out, that a single critical Richardson number smaller than one at which turbulence is totally suppressed and laminarised, does not exist. Therefore, the critical Richardson number should be avoided as a criterion of turbulence extinction.

Stretch et al. [62] investigated the mixing efficiency in stratified flows with direct numerical simulations and rapid distortion theory calculations. The aim of this research was the determination of the mixing efficiency of decaying, homogeneous, stably-stratified turbulence as a function of the initial turbulence Richardson number. The investigated stratification is

caused by different salt concentrations in water. It was found, that for small Richardson numbers, the mixing efficiency can be increased by increasing the Richardson number. For larger Richardson numbers, the mixing efficiency becomes constant. In the experiments, this means Ri > 1. Further investigation on the numerical part is suggested due to quantitative deviations of both, the direct numerical simulation and the rapid distortion theory calculations compared to the experimental data.

The effect of stable stratification on turbulence anisotropy was investigated by Sarkar [63] with direct numerical simulations. Two flows have been investigated, a flow with horizontal mean shear as well as one flow with vertical mean shear. The results show that the horizontal and vertical velocity fluctuations remain coupled for either flow. One consequence of this coupling is, that vertical mixing is induced by horizontal mean shear. Another consequence is, that the vertical mixing is larger when the mean shear is horizontal, because the gravity has no damping effect on the turbulence production.

Lin et al. [64] carried out experiments to investigate the entrainment due to a turbulent fountain at a density interface. Fig. 10 shows the set-up of the experiment. Q_p is the volume flux of the plume, Q_f is the volume flux of the fountain, Q_E is the volume flux of the entrainment, Q_{EU} is the volume flux of the entrainment and fluid from the upper layer, and Q_{out} is the volume flux leaving the tank. M_f is the momentum flux of the fountain. B is the buoyancy flux of the plume source. g_1' Is the reduced gravity of the upper layer and g_2' is the reduced gravity of the lower layer. H is the height of the tank and h is the depth of the interface.

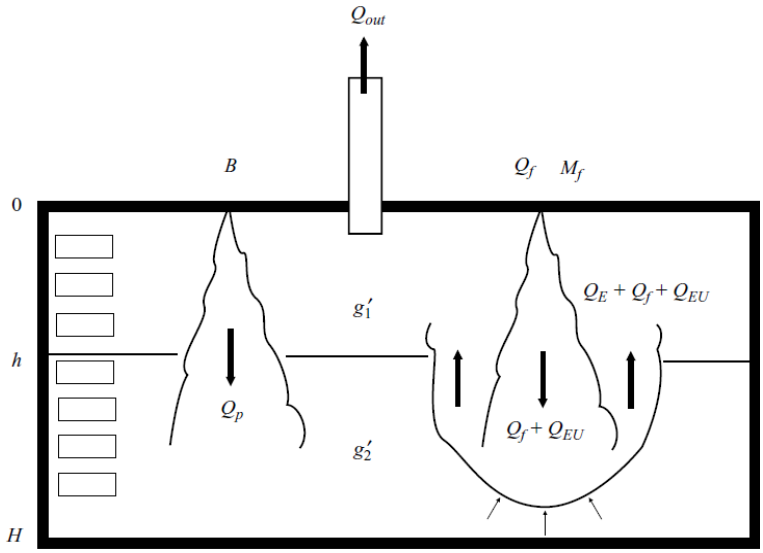

Fig. 10: Steady state mixing of a density stratification [64]

The tank is filled with water. A downward plume on the left hand side of the tank is filling the lower vessel with salt water. Because of the greater density of salt water a stable stratification is the result. A downward water fountain on the right hand side of the tank is eroding the density layer. The permanent supply with salt water and the outlet in the middle of the ceiling

enable a steady state situation.

The interaction between stratification and fountain in the experiments of Lin is comparable to the TH20 flow (Fig. 4). The major difference is that the mixing is induced by a fountain of the less dense fluid in the direction of gravity whereas in the TH20 case a jet of the denser fluid against the direction of gravity is responsible for the mixing.

1.2.4 Recapitulation

As shown in this chapter, a better and more detailed understanding of containment flows is the focus of several research activities. A broad range of different phenomena has been investigated with experimental and numerical methods. Different forms of mixing have been discussed with different grades of complexity, which includes a one-component flow in a multi-compartment containment and up to three-component flows with condensation. Steam and condensation are important issues for accident scenarios in light-water reactors, due to the large amounts of water inside the containment and its use for cooling the core. While steam and condensation are present in a real accident scenario, it is important for CFD model development to follow a stepwise approach, which includes two-phase phenomena, but focuses first on more basic flows like one-phase, two-component mixing.

Simulations of free jets yield good agreement with experiments. State-of-the-art CFD methods are capable to predict common jet and plume flows. Investigations of the impact of the origin of the jet show a considerable influence on the behaviour of the jet. The mixing rate of the jet originating from a nozzle is larger than the mixing rate of a jet originating from a long pipe.

Experiments to investigate stably stratified flows have been carried out, especially regarding flows in large buildings like reactor containments. To improve the CFD models for this type of flow is currently the focus of several projects. Experiments in the model containment facilities with well-defined boundary conditions try to generate high-quality measurement data for CFD model validation.

1.3 Mechanism of a Stable Stratification

The stability or instability of a stratification can be explained with the effect of the buoyant force F_B. In Fig. 11, a tank is shown. Two fluids with different densities, $\rho_2 > \rho_1$, are forming a stable stratification inside the tank. Now a fluid volume V_f with the higher density ρ_2 could be brought into a region with a lower density ρ_1, for example due to a free jet. Since V_f still has a higher density than its surrounding fluid, buoyancy will cause it to move back. So, the buoyant force has a stabilising effect on the stratification. This is true as long as V_f has a higher density. This means that a larger density gradient causes a more stable stratification because the buoyant force F_B on V_f is larger.

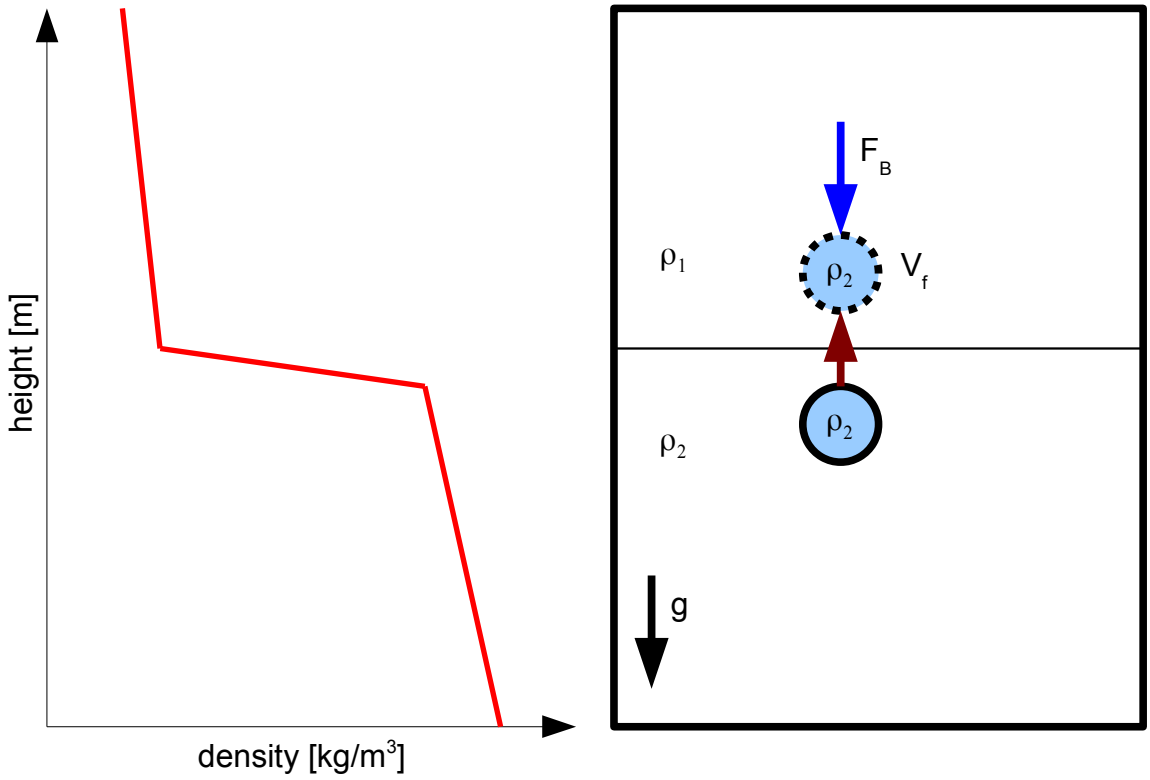

Fig. 11: Mechanism of a stable stratification

An example for an unstable stratification is the Rayleigh-Bénard convection [83]. In this case, two plates with different temperatures are responsible for the density stratification. The plate with the higher temperature is below. Therefore, the less dense fluid is below the denser fluid ($\rho_2 < \rho_1$). In the case of a unstable stratification, the buoyant force has an amplifying effect on the disturbance and is therefore destabilising.

1.4 Aim of this Study

The use of CFD methods to predict containment flows is desirable to further improve the safety of light-water reactors. One specific flow, the erosion of a stable stratification with a free jet, was investigated in the ISP 47 workshop [12] to evaluate the capabilities of currently available CFD software regarding this flow. The results of this workshop was, that the used CFD codes show poor agreement with the experimental data. The reason for this poor agreement is the inability of the CFD codes to calculate non-isotropic turbulent scalar fluxes, in this case the turbulent mass fluxes, properly. The reason for this is the isotropic eddy diffusivity model which is used to calculate the turbulent scalar fluxes.

The aim of this study is to improve the capability of CFD methods to predict the mixing of a stable stratification by using the non-isotropic turbulent scalar flux (TSF) model. This will

contribute to the improvement of the safety analysis of light-water reactors.

Modelling and simulation of a specific physical phenomenon inside a complex flow means the focus on that phenomenon and the simplification of the complex flow to make the phenomenon more accessible (Laurien [65]).

The phenomenon in question for this work is the mixing of stable hydrogen stratification with a free jet as part of a complex containment flow. Because it is not feasible to perform experiments or simulations for modelling purposes inside a real containment, the THAI model containment was used for the experiments. Here, the hydrogen was replaced with helium for safety reasons. The relevant experiment for this work is the TH20 experiment, denoted as the 'experimental case'.

By using this experiment, the flow is significantly simplified and focused on the interaction of jet and stratification. The geometry is smaller and is missing the different rooms and obstacles of a real containment, which would complicate the investigation of the flow. The rotational symmetry of the experiment is also beneficial, because it can be modelled two-dimensionally. However, the geometry is still large for CFD calculations. Another factor, that is limiting the use of the experiment for turbulence modelling, is the long transient of more than 1000 seconds. A problem of transient calculations is the needed CPU time. Long transients combined with large geometries result in expensive calculations. While CPU time is an issue, it can be mitigated by parallelization. But the greater problem, that transient flows yield for turbulence modelling, is the comparability of different calculations. While the helium concentration at a certain measurement point provides a good insight into the mixing behaviour of a turbulence model, the comparison of the spatial distribution of interesting variables, like turbulent values or velocity components, is necessary for turbulence modelling.

A theoretical, two-dimensional, steady-state test case, denoted 'steady case', is designed to enable direct comparisons between different simulations by focussing on the mixing process without considering the time. A statistically steady state is also advantageous for the post-processing of a large eddy simulation, especially to determine turbulence values (Zirkel and Laurien [67]).

Fig. 12 illustrates the simplification process. The steady case is a theoretical case without experimental data. A large eddy simulation is performed as reference. The use of a LES as reference is beneficial for turbulence modelling, as it delivers detailed information of difficult-to-measure quantities, like the turbulent scalar fluxes.

The data of the LES are used to improve the results of the turbulence scalar flux model. Selected model coefficients of the TSF model are modified. The resulting set of model coefficients is then used to simulate the experimental case to compare the result of the new model coefficients to measured data.

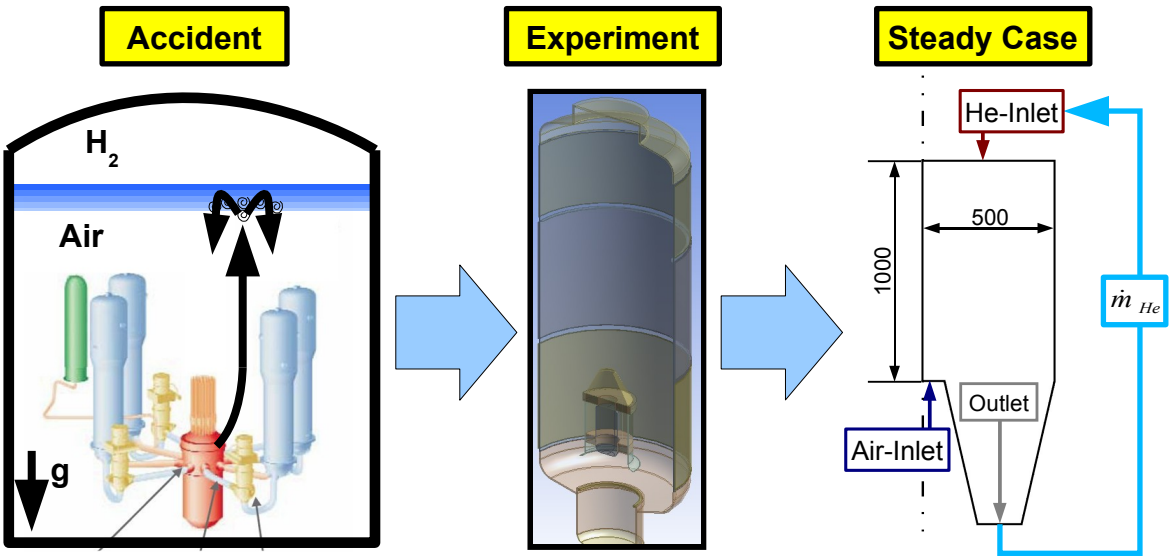

Fig. 12: Focusing on separated effects of a LOCA

2 Modelling

To investigate a physical problem with numerical methods is closely related to several modelling decisions. The steady case introduced in chapter 1.3 is a conceptional model of the TH20 experimental case. A dimension analysis for this case is discussed in this chapter. Furthermore, different turbulence models are introduced followed by a derivation of the turbulence scalar flux model. Finally, the integration domains for both cases and the corresponding boundary conditions are presented.

2.1 Dimension Analysis

2.1.1 Dimension Matrix

To ensure that the test case is a reasonable representation of the experimental case, a dimension analysis is performed to determine independent dimensionless numbers to compare those cases (Scirtes [68]). A set of seven parameters describes the experimental case at a given time. Those parameters are the length L of the jet which is the distance between the nozzle and the stable stratification, the velocity u of the jet, the density ρ, the density difference Δρ between the jet and the light-gas cloud, the viscosity ν, the gravity acceleration g and the diffusion constant D. The three base units for those parameters are [m], [s] and [kg].

Seven parameters with three base units means that there are four independent dimensionless numbers. The expected relevant dimensionless numbers for this dimension analysis are describing the relevant physical phenomena of turbulence and buoyant forces. The Reynolds number Re is the ratio of inertial forces to viscous forces and a value for the turbulence. The Richardson number Ri is the ratio of potential to kinetic energy. The Archimedes number Ar is the ratio of buoyancy forces to friction forces. The Schmidt number Sc is the ration of convective to diffusive mass transport.

L	u	ρ	Δρ	ν	g	D	Re	Ri	Ar	Sc
m	$\frac{m}{s}$	$\frac{kg}{m^3}$	$\frac{kg}{m^3}$	$\frac{m^2}{s}$	$\frac{m}{s^2}$	$\frac{m^2}{s}$	$\frac{L \cdot u}{\nu}$	$\frac{g \cdot L}{u^2}$	$\frac{\Delta\rho \cdot g \cdot L^3}{\rho \cdot \nu^2}$	$\frac{\nu}{D}$

Table 1: Parameters for the dimension analysis

To prove that the dimensional numbers are independent, the determinant of the dimension matrix must be different from zero. The dimension matrix (Fig. 13) is the correlation of the describing parameters and the base units and dimensionless numbers.

	L	u	ρ	$\Delta\rho$	ν	g	D
m	1	1	−3	−3	2	1	2
s	0	−1	0	0	−1	−2	−1
kg	0	0	1	1	0	0	0
Re	1	1	0	0	−1	0	0
Ri	1	−2	0	0	0	1	0
Ar	3	0	−1	1	−2	1	0
Sc	0	0	0	0	1	0	−1

Fig. 13: Dimension matrix

Every parameter has its column and every base unit and dimensionless number has its row. The values of the matrix are the exponents with which the base units appear in the dimension of the parameter or the exponent with which the parameter appears in a dimensionless number. For example, velocity has the dimension m/s. So the value for meter is 1 and for second -1. Velocity appears with the exponent 1 in the Reynolds number and with -2 in the Richardson number. The determinant of the dimension matrix is -56. So it is demonstrated, that the dimensionless parameters are independent.

2.1.2 Parameters

The length of the free jet, which is the distance between the nozzle outlet and the stable stratification, is the characteristic length.

$$L_{steady} = 0.66\,m\,;\, L_{\exp} = 2.27\,m$$

The maximum velocity of the free jet is taken as the characteristic velocity.

$$u_{steady} = 2.013\frac{m}{s};\, u_{\exp} = 1.827\frac{m}{s}$$

Reference density is the density of air, $\rho_{Air} = 1.185\frac{kg}{m^3}$. For the density differences, the density of the light gas cloud is necessary. In the test case, the light gas cloud is pure helium with a density of $\rho_{He} = 0.1785\frac{kg}{m^3}$. In the TH20 case, the light gas cloud has 36% helium and a density of $\rho_{He} = 0.84\frac{kg}{m^3}$

The characteristic density difference is the difference between air and the light gas cloud.

$$\Delta\rho_{steady} = \rho_{Air} - \rho_{He} = 1.0065\frac{kg}{m^3};\, \Delta\rho_{\exp} = \rho_{Air} - \rho_{Mix} = 0.345\frac{kg}{m^3}$$

The kinematic viscosity is

$$\nu_{steady}=\frac{1}{2}\left(\nu_{Air}+\nu_{He}\right)=\frac{1}{2}\left(1.545\cdot10^{-5}\frac{m^2}{s}+10.4202\cdot10^{-5}\frac{m^2}{s}\right)=5.9826\cdot10^{-5}\frac{m^2}{s}$$

$$\nu_{\exp}=\frac{1}{2}\left(\nu_{Air}+\nu_{Mix}\right)=\frac{1}{2}\left(1.545\cdot10^{-5}\frac{m^2}{s}+2.183\cdot10^{-5}\frac{m^2}{s}\right)=1.864\cdot10^{-5}\frac{m^2}{s}$$

The gravity constant is $g=9.81\frac{m}{s^2}$ and the diffusion constant for helium and air $D=26.5\cdot10^{-4}\frac{m^2}{s}$ (Bird et al. [69]).

2.1.3 Dimensionless Numbers

Table 2 shows the dimensionless numbers for both cases. The Reynolds number indicates a fully turbulent flow for both cases. The Richardson number shows a slight dominance of the potential energy in both cases. The Archimedes number in both cases is very large. This stands for a domination of the buoyancy forces. The Schmidt number is almost the same for both cases.

	Re	Ri	Ar	Sc
steady case	$2.22\cdot10^4$	1.6	$6.69\cdot10^8$	0.02
experimental case	$2.22\cdot10^5$	6.67	$7.8\cdot10^{10}$	0.01

Table 2: Dimensionless numbers

2.2 Favre-averaged Navier-Stokes Equations

The basic equations of fluid dynamics are the Navier-Stokes equations (Siekmann and Thamsen [70], Rodi [71]). They consist of the continuity equation for the conservation of mass and equations for the conservation of momentum. In the present case of a single phase mixture of different fluids, the Navier-Stokes equations are complemented with the conservation of species concentration. Since the problem is isothermal, the energy conservation equation is not considered. For an incompressible flow, they are as follows.

Continuity equation:

$$\frac{\partial u_i}{\partial x_i}=0 \qquad (2\text{-}1)$$

Momentum equations:

$$\rho\left(\frac{\partial u_i}{\partial t}+u_j\frac{\partial u_i}{\partial x_j}\right)=-\frac{\partial p}{\partial x_i}+\frac{\partial \tau_{ji}}{\partial x_j}+g_i\left(\frac{\rho-\rho_r}{\rho_r}\right) \tag{2-2a}$$

$$\tau_{ij}=\mu\left(\frac{\partial u_i}{\partial x_j}+\frac{\partial u_j}{\partial x_i}\right) \tag{2-2b}$$

Concentration equation:

$$\frac{\partial \varphi}{\partial t}+u_i\frac{\partial \varphi}{\partial x_i}=\lambda\frac{\partial^2 \varphi}{\partial x_i \partial x_i} \tag{2-3}$$

The Navier-Stokes equations are capable of completely describing a flow given a sufficiently fine grid. This approach is called a direct numerical simulation (DNS). For most engineering applications the instantaneous behaviour of single eddies is not important. So a statistical investigation of a flow is sufficient. The commonly used approach is the Reynolds averaging, where a value is separated into a time averaged mean component and a fluctuating component.

$$u=\bar{u}+u' \tag{2-4}$$

The time averaging is defined as follows.

$$\bar{u}=\frac{1}{T}\cdot\int_0^T u\cdot dt \tag{2-5}$$

For flows with changing density, the Favre mass-averaging is advantageous (Wilcox [72]).

$$\tilde{u}=\frac{\overline{\rho u}}{\bar{\rho}} \tag{2-6}$$

To perform a Favre averaging of the conservation equations, the flow properties are decomposed as follows.

$$\begin{aligned}\rho&=\bar{\rho}+\rho'\\ p&=\bar{p}+p'\\ u&=\tilde{u}+u''\\ \varphi&=\tilde{\varphi}+\varphi''\end{aligned} \tag{2-7}$$

Using (2-6) and (2-7) on (2-1), (2-2) and (2-3) results in the Favre-averaged Navier-Stokes equations.

Continuity equation:
$$\frac{\partial \tilde{u}_i}{\partial x_i} = 0 \tag{2-8}$$

Momentum equations:
$$\bar{\rho}\left(\frac{\partial \tilde{u}_i}{\partial t} + \tilde{u}_j \frac{\partial \tilde{u}_i}{\partial x_j}\right) = -\frac{\partial \bar{p}}{\partial x_i} + \frac{1}{\partial x_j}\left(\overline{\tau_{ji}} - \overline{\rho u_j'' u_i''}\right) + g_i\left(\frac{\rho - \rho_r}{\rho_r}\right) \tag{2-9}$$

Concentration equation:
$$\bar{\rho}\left(\frac{\partial \tilde{\varphi}}{\partial t} + \tilde{u}_i \frac{\partial \tilde{\varphi}}{\partial x_i}\right) = \frac{\partial}{\partial x_i}\left(\lambda \frac{\partial \tilde{\varphi}}{\partial x_i} - \overline{\rho \varphi'' u_i''}\right) \tag{2-10}$$

These equations are similar to the base equations except for the additional turbulent terms in the momentum and concentration equation. The momentum equations now have the Reynolds Stress tensor,

$$\tilde{\tau}_{ij} = \overline{-\rho u_i'' u_j''} \tag{2-11}$$

and the concentration equation contains the turbulent mass flux vector

$$\tilde{\Phi}_i = \overline{-\rho \varphi'' u_i''} \tag{2-12}$$

The fluctuation terms are determined with turbulence models.

2.3 Reynolds Stress Model

The isotropic Boussinesq approach to model the Reynolds Stress tensor is widely used, for example in two equation turbulence models (Jones and Lentini [73], Menter [74]). But it is not suitable for non-isotropic problems because the effect of the turbulent structures on the mean flow depends on their direction (Laurien and Wintterle [75]). The secondary flow in a non-circular pipe for example is a result of non-isotropic Reynolds stresses. Two-equation models are also insufficient for flows with strongly bent streamlines.

To take non-isotropic effects into account, the Reynolds stress models have a transport equation for every Reynolds stress (Speziale et al. [76]). Those transport equations are derived by subtracting the Favre-averaged momentum equation (2-9) from the momentum equation (2-2) for the x_i and the x_j momentum. The resulting equation $N(u)$ for the component *i* is multiplied with the fluctuating velocity u'' for the component *j* and vice versa. The

sum of both is then Reynolds averaged.

$$\overline{N\left(u_i\right)u_j'' + N\left(u_j\right)u_i''} = 0 \tag{2-13}$$

Because of the Reynolds averaging, every term with only one fluctuating component is zero. The remaining products of fluctuating velocities, which are the components of the Reynolds stress tensor, are forming the transport equations. There are nine equations of which six are different, due to symmetry.

$$\frac{\partial \tilde{\tau}_{ij}}{\partial t} + \tilde{u}_k \frac{\partial \tilde{\tau}_{ij}}{\partial x_k} = D_{ijk} + P_{ij} + \epsilon_{ij} + \Pi_{ij} + G_{ij} \tag{2-14}$$

The right side of the Reynolds stress equations consists of the diffusive transport D_{ijk}, the stress production P_{ij}, dissipation tensor ϵ_{ij}, the pressure strain correlation Π_{ij} and the buoyancy production G_{ij}.

The diffusive transport consists of the turbulent diffusion and the pressure diffusion.

$$D_{ijk} = \bar{\rho} \frac{\partial \overline{u_i'' u_j'' u_k''}}{\partial x_k} + \frac{\partial \overline{p'' u_j''}}{\partial x_i} + \frac{\partial \overline{p'' u_i''}}{\partial x_j} \tag{2-15}$$

The stress production term is a source term for the production or destruction of turbulence. It can have an amplifying or a damping effect on the Reynolds stresses.

$$P_{ij} = \bar{\rho}\left(\tilde{\tau}_{ik} \frac{\partial \tilde{u}_j}{\partial x_k} + \tilde{\tau}_{jk} \frac{\partial \tilde{u}_i}{\partial x_k} \right) \tag{2-16}$$

ϵ_{ij} is the viscous dissipation. In a laminar flow it can be neglected, but dissipation caused by the fluctuations in a turbulent flow has to be considered.

$$\epsilon_{ij} = 2\mu \overline{\frac{\partial u_i''}{\partial x_k} \frac{\partial u_j''}{\partial x_k}} \tag{2-17}$$

The pressure-strain correlation Π_{ij} considers the interdependency of pressure and velocity fluctuations. It is not a source of turbulence, but describes a redistribution of the Reynolds stresses.

$$\Pi_{ij} = -\overline{p\left(\frac{\partial u_i''}{\partial x_j} + \frac{\partial u_j''}{\partial x_i} \right)} \tag{2-18}$$

Turbulence production due to buoyancy effects is considered in the buoyancy production term.

$$G_{ij} = \beta\left(g_i \tilde{\Phi}_j + g_j \tilde{\Phi}_i\right) \tag{2-19}$$

2.4 Turbulent Scalar Flux Model

Similar to the modelling of the Reynolds stresses, a simple model which is using the eddy viscosity is widely used to calculate the turbulent scalar fluxes.

$$\tilde{\Phi}_i = \frac{\nu_t}{\sigma_t} \cdot \frac{\partial \tilde{\varphi}}{\partial x_i} \tag{2-20}$$

This is the eddy diffusivity model (EDM), where the spatial gradient of the concentration $\frac{\partial \tilde{\varphi}}{\partial x_i}$ is multiplied with the eddy diffusivity $\frac{\nu_t}{\sigma_t}$. The eddy diffusivity is the eddy viscosity ν_t divided by a turbulent Schmidt number σ_t which is constant. This approach cannot take non-isotropy into account, which is present in a stratified flow, because with the eddy viscosity the same turbulent value is used for every spatial direction.

Similar to the Reynolds stress equations, the exact equations for the turbulent scalar fluxes can be derived (Rodi [71]). The momentum equation (2-2) for the component *i* is

$$N(u_i) = \rho \frac{\partial u_i}{\partial t} + \rho u_k \frac{\partial u_i}{\partial x_k} + \frac{\partial p}{\partial x_k} - \rho \nu \frac{\partial^2 u_i}{\partial x_k^2} - g\left(\frac{\rho - \rho_r}{\rho_r}\right) \tag{2-21}$$

and the concentration equation (2-3) is

$$N(\varphi) = \rho \frac{\partial \varphi}{\partial t} + \rho u_k \frac{\partial \varphi}{\partial x_k} - \rho \lambda \frac{\partial^2 \varphi}{\partial x_k^2} \tag{2-22}$$

$N(u_i)$ is multiplied with the fluctuating scalar φ'' and $N(\varphi)$ with the fluctuating velocity u_i''. The sum is then Reynolds averaged.

$$\overline{N(u_i)\varphi'' + N(\varphi)u_i''} = 0 \tag{2-23}$$

$$\begin{aligned}
&\overline{N(u_i)\varphi'' + N(\varphi)u_i''} \\
&= \\
&\overline{\rho\varphi''\frac{\partial u_i}{\partial t}} + \overline{\rho\varphi'' u_k \frac{\partial u_i}{\partial x_k}} + \overline{\varphi''\frac{\partial p}{\partial x_k}} - \overline{\varphi''\mu\frac{\partial^2 u_i}{\partial x_k^2}} - \overline{\varphi'' g\left(\frac{\rho-\rho_r}{\rho_r}\right)} \\
&+ \\
&\overline{\rho u_i''\frac{\partial \varphi}{\partial t}} + \overline{\rho u_i'' u_k \frac{\partial \varphi}{\partial x_k}} - \overline{\rho u_i''\lambda\frac{\partial^2 \varphi}{\partial x_k^2}}
\end{aligned} \tag{2-24}$$

First the unsteady term:

$$\begin{aligned}
\overline{\rho\varphi''\frac{\partial u_i}{\partial t}} + \overline{\rho u_i''\frac{\partial \varphi}{\partial t}} &= \bar{\rho}\left(\overline{\varphi''\frac{\partial\left(\tilde{u}_i + u_i''\right)}{\partial t}} + \overline{u_i''\frac{\partial\left(\tilde{\varphi}+\varphi''\right)}{\partial t}}\right) \\
&= \bar{\rho}\left(\overline{\varphi''\frac{\partial u_i''}{\partial t}} + \overline{u_i''\frac{\partial \varphi''}{\partial t}}\right) \\
&= \bar{\rho}\frac{\partial \overline{u_i''\varphi''}}{\partial t} = \bar{\rho}\frac{\partial \tilde{\Phi}_i}{\partial t}
\end{aligned} \tag{2-25}$$

The convective term:

$$\begin{aligned}
\overline{\rho\varphi'' u_k\frac{\partial u_i}{\partial x_k}} + \overline{\rho u_i'' u_k\frac{\partial \varphi}{\partial x_k}} &= \overline{\rho\varphi''\left(\tilde{u_k}+u_k''\right)\frac{\partial\left(\tilde{u}_i+u_i''\right)}{\partial x_k}} \\
&\quad + \overline{\rho u_i''\left(\tilde{u_k}+u_k''\right)\frac{\partial\left(\tilde{\varphi}+\varphi''\right)}{\partial x_k}} \\
&= \bar{\rho}\left(\overline{\varphi''\tilde{u_k}\frac{\partial u_i''}{\partial x_k}} + \overline{u_i''\tilde{u_k}\frac{\partial \varphi''}{\partial x_k}}\right) \\
&\quad + \bar{\rho}\left(\overline{\varphi'' u_k''\frac{\partial u_i''}{\partial x_k}} + \overline{u_i'' u_k''\frac{\partial \varphi''}{\partial x_k}}\right) \\
&\quad + \bar{\rho}\left(\overline{\varphi'' u_k''\frac{\partial \tilde{u}_i}{\partial x_k}} + \overline{u_i'' u_k''\frac{\partial \tilde{\varphi}}{\partial x_k}}\right) \\
= \bar{\rho}\tilde{u_k}\frac{\partial\left(\overline{u_i''\varphi''}\right)}{\partial x_k} &+ \bar{\rho}\frac{\partial\left(\overline{u_i''\varphi'' u_k''}\right)}{\partial x_k} + \bar{\rho}\left(\overline{\varphi'' u_k''}\frac{\partial \tilde{u}_i}{\partial x_k} + \overline{u_i'' u_k''}\frac{\partial \tilde{\varphi}}{\partial x_k}\right)
\end{aligned} \tag{2-26}$$

Here, the continuity equation is used $\frac{\partial(\overline{u_k''})}{\partial x_k}=0$:

$$\bar{\rho}\frac{\partial(\overline{u_i''\varphi''u_k''})}{\partial x_k}=\bar{\rho}\,\overline{u_k''}\frac{\partial(\overline{u_i''\varphi''})}{\partial x_k}+\bar{\rho}\,\overline{u_i''\varphi''}\frac{\partial(\overline{u_k''})}{\partial x_k} \tag{2-27}$$

The viscous term follows the same pattern.

$$-\overline{\varphi''\mu\frac{\partial^2 u_i}{\partial x_k^2}}-\overline{\rho\,u_i''\lambda\frac{\partial^2\varphi}{\partial x_k^2}} \;=\; -\rho(\nu+\lambda)\overline{\frac{\partial u_i''}{\partial x_k}\frac{\partial\varphi''}{\partial x_k}} \tag{2-28}$$

The buoyancy production term is again derived with the use of $\beta=\frac{\rho'}{\varphi''}$.

$$\begin{aligned}-\overline{\varphi''\left(\frac{\rho-\rho_r}{\rho_r}\right)g_i} \;&=\; -\overline{\varphi''(\rho+\rho')g_i}\\ &=\; -\overline{\varphi''\rho'g_i}\\ &=\; -\beta\,g_i\overline{\varphi''^2}\end{aligned} \tag{2-29}$$

In the buoyancy production, the scalar fluctuation $\overline{\varphi''^2}$ appears, which needs an additional transport equation.

Combining all parts results in the exact transport equations for the turbulent scalar flux.

$$\begin{aligned}\frac{\partial\tilde{\Phi}_i}{\partial t}+\tilde{u_k}\frac{\partial\tilde{\Phi}_i}{\partial x_k} \;=\; &-\frac{\partial}{\partial x_k}\left(\overline{u_i''\varphi''u_k''}+\frac{1}{\bar{\rho}}\delta_{ik}\overline{p'\varphi''}\right)\\ &-\left(\overline{\varphi''u_k''}\frac{\partial\tilde{u}_i}{\partial x_k}+\overline{u_i''u_k''}\frac{\partial\tilde{\varphi}}{\partial x_k}\right)\\ &-\beta\,g_i\overline{\varphi''^2}+\frac{1}{\bar{\rho}}\overline{p'\frac{\partial\varphi''}{\partial x_i}}\\ &-(\nu+\lambda)\overline{\frac{\partial u_i''}{\partial x_k}\frac{\partial\varphi''}{\partial x_k}}\end{aligned} \tag{2-30}$$

The equation for the scalar fluctuation $\overline{\varphi''^2}$ can be derived in a similar way as the equations for $\overline{u_i''\varphi''}$ using equations (2-3) and (2-10).

$$\frac{\partial\overline{\varphi''^2}}{\partial t}+u_i\frac{\partial\overline{\varphi''^2}}{\partial x_i}=-\frac{\partial}{\partial x_i}\left(\overline{u_i''\varphi''^2}\right)-2\tilde{\Phi}_i\frac{\partial\tilde{\varphi}}{\partial x_i}-2\lambda\overline{\frac{\partial\varphi''}{\partial x_i}\frac{\partial\varphi''}{\partial x_i}} \tag{2-31}$$

Following the modelling approach of Rodi [71][77], the TSF model is

$$\frac{\partial \tilde{\Phi}_i}{\partial t}+\tilde{u}_k\frac{\partial \tilde{\Phi}_i}{\partial x_k} \;=\; P_Y+G_Y+D_Y+\Pi_Y \tag{2-32}$$

The terms on the right-hand side are as follows.

Mean-field production:
$$P_Y=-\tilde{\tau}_{ij}\frac{\partial \tilde{\varphi}}{\partial x_j}-\tilde{\Phi}_j\frac{\partial \tilde{u}_i}{\partial x_j} \tag{2-33}$$

Buoyancy production:
$$G_Y=-\left(1-C_{3Y}\right)\beta\frac{\overline{\varphi''^2}}{\bar{\rho}}\left(\frac{\partial \bar{p}_{stat}}{\partial x_i}+\rho_{ref}\,g_i\right) \tag{2-34}$$

Diffusive transport:
$$D_Y=\frac{\partial}{\partial x_j}\left[\left(\mu+\frac{2}{3}C_Y\frac{k^2}{\epsilon}\bar{\rho}\right)\frac{\partial}{\partial x_j}\left(\frac{\tilde{\Phi}_i}{\bar{\rho}}\right)\right] \tag{2-35}$$

Pressure-scalar gradient correlation:
$$\Pi_Y=-C_{1Y}\frac{\epsilon}{k}\tilde{\Phi}_i-C_{2Y}\tilde{\Phi}_j\frac{\partial \tilde{u}_i}{\partial x_j}-C_{4Y}\tilde{\Phi}_j\frac{\partial \tilde{u}_j}{\partial x_i} \tag{2-36}$$

The preliminary values for the model coefficients are $C_{1Y}=2.9$, $C_{2Y}=0.4$, $C_{3Y}=0.55$, $C_{4Y}=0.0$ and $C_Y=0.15$. The variance $\overline{\varphi''^2}$ in the buoyancy production is considered with

$$\frac{\partial \overline{\varphi''^2}}{\partial t}+\tilde{u}_j\frac{\partial \overline{\varphi''^2}}{\partial x_j} \;=\; P_{YY}+D_{YY}+\epsilon_{YY} \tag{2-37}$$

The terms on the right-hand side are as follows.

Mean-field production:
$$P_{YY}=-2\tilde{\Phi}_j\frac{\partial \tilde{\varphi}_l}{\partial x_j} \tag{2-38}$$

Diffusive transport:
$$D_{YY}=\frac{\partial}{\partial x_j}\left[\left(\mu+\frac{2}{3}C_{YY}\frac{k^2}{\epsilon}\bar{\rho}\right)\frac{\partial}{\partial x_j}\left(\frac{\overline{\varphi''^2}}{\bar{\rho}}\right)\right] \tag{2-39}$$

Dissipation:

$$\epsilon_{YY} = -2C_{1YY}\frac{\epsilon}{k}\overline{\varphi''^2} \tag{2-40}$$

The preliminary values for the model coefficients are $C_{YY} = 0.2$ and $C_{1YY} = 1.0$.

2.5 Filtered Navier-Stokes Equations

A Large Eddy Simulation (LES) is directly simulating the large, energy bearing eddies. A subgrid-scale (SGS) model is used for the small eddies, which cannot be resolved by the grid. To assure a resolution of all large eddies, the grid must be sufficiently fine to resolve the inertial range. Fig. 14 shows an energy spectrum, energy E over wave number k with the three characteristic regions, the large eddies, the inertial range and the dissipation range. The dashed line marks a desirable resolution of the grid.

To perform a LES, a filter is used for the Navier-Stokes equations, that filters out scales smaller than the grid size. The transport values are separated into a grid-scale and a subgrid-scale part.

$$u_i = \hat{u}_i + \dot{u}_i \quad , \quad p_i = \hat{p}_i + \dot{p}_i \quad , \quad \varphi = \hat{\varphi} + \dot{\varphi} \tag{2-41}$$

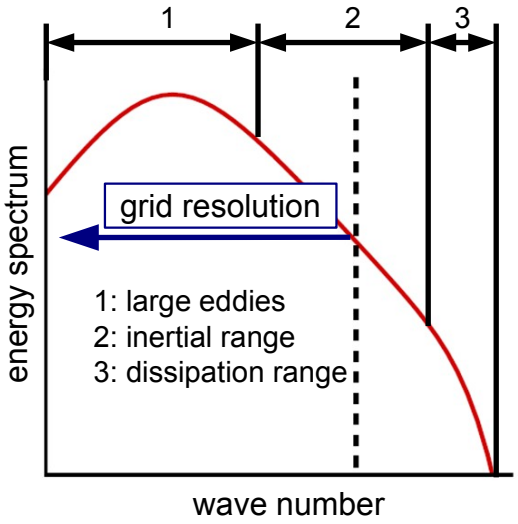

Fig. 14: Energy Spectrum

After the filtering (Fröhlich [78], Wilcox [72]), the filtered Navier-Stokes equations can be written as

Continuity equation:

$$\frac{\partial \hat{u}_i}{\partial x_i} = 0 \tag{2-42}$$

Momentum equations:

$$\frac{\partial \hat{u}_i}{\partial t} + \frac{\partial \left(\hat{u}_i \hat{u}_j \right)}{\partial x_j} = -\frac{\partial \hat{p}}{\partial x_i} + \frac{\partial \left(2\nu \hat{S}_{ij} \right)}{\partial x_j} - \frac{\partial \hat{\tau}_{ij}}{\partial x_j} \tag{2-43}$$

$\hat{\tau}_{ij}$ is modelled with the Smagorinski subgrid-scale model.

$$\hat{S}_{ij} = \frac{1}{2}\left(\frac{\partial \hat{u}_i}{\partial x_j} + \frac{\partial \hat{u}_j}{\partial x_i} \right) \quad , \quad \hat{\tau}_{ij} = 2\hat{\nu}_t \hat{S}_{ij} \tag{2-44}$$

$\hat{\nu}_t$ is the Smagorinsky eddy viscosity. Together with the Smagorinsky constant C_s and the grid size Δ, it can be modeled as:

$$\hat{\nu}_t = \left(C_s \Delta \right)^2 \sqrt{S_{ij} S_{ij}} \tag{2-45}$$

2.6 Integration Domain and Boundary Conditions

The correct choice of the integration domain and the boundary conditions is crucial for a successful simulation. In this chapter, the integration domains and boundary conditions for the simulation of the experiment and the steady case will be discussed.

2.6.1 Experiment

For the numerical investigation, the TH20.8 experiment is used as the experimental case. As shown in Fig. 3 (page 3), the geometry of the experiment is rotational symmetric. This is also true for the experimental boundary conditions. Therefore a two-dimensional integration domain is used to simulate the experiment (Fig. 15, left). The two-dimensional domain is realised with a 1° wedge with a thickness of 1 cell. The right-hand side of Fig. 15 shows the initial radial helium concentration at a given height. The used fluid is a variable composition mixture containing air as ideal gas and helium. The helium concentration is the passive scalar transported by the concentration equation and air is constraint. Buoyancy must be considered due to the variable density. The reference density for the buoyancy treatment is $0.179 \frac{kg}{m^3}$ and the gravity constant is $g = 9.81 \frac{m}{s}$. The initialisation and reference pressure is 1.168 bar. The initialisation temperature is 24.3°C.

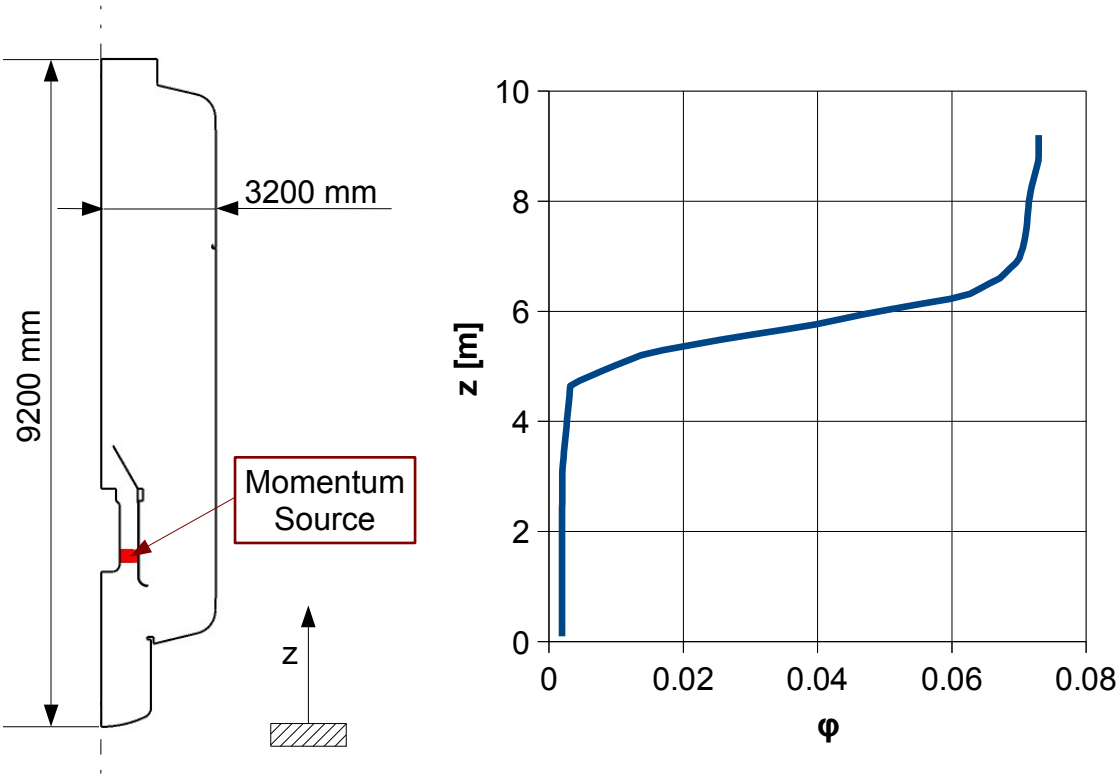

Fig. 15: Experimental Case: integration domain (left) and initial helium distribution (right)

The first approach to generate the jet was to replace the inner part of the inner cylinder with an outlet boundary at the bottom of the inner cylinder and a velocity inlet boundary condition at the top of the nozzle. The helium is transferred from the outlet to the inlet, to prevent a loss of helium. A problem with this approach is that the influence of the increasing helium concentration on the generation of the jet cannot be covered. The fan, which is responsible for the jet generation, is applying a pressure gradient on the fluid. It acts as a momentum source. If the density of the fluid decreases with an increasing concentration of helium, the volumetric flow rate will increase. This results in a greater jet velocity. Another minor problem is the shift of helium between outlet and inlet. Because the helium is bypassing the interior of the inner cylinder it is faster at the inlet than in reality. This can influence the result, because a higher helium concentration of the jet means a less sharp density gradient between jet and density layer, which results in a better mixing, which in turn leads to a higher helium concentration at the outlet. This effect is cumulative and can influence the result given the long transient.

An additional problem is associated with the nozzle as origin of the jet. As discussed in chapters 1.2.2 and 1.2.4, the mixing rate of a jet originating from a nozzle is larger compared to a long pipe as origin. The so called 'vena contracta' effect appears if the origin of a jet is a nozzle or orifice and must also be considered. Vena contracta is the constriction and acceleration of a jet depending of the opening angle of the nozzle (Alan Fox and Robert McDonald [79]).

Fig. 16 shows the behaviour of the jet close to the outlet of the nozzle dependent on the

opening angle. Here, 90° is a long pipe and 0° an orifice. The velocity scale shows the maximum 10% of the stream-wise velocity. It can be seen, that the long pipe jet has already reached its maximum velocity at the outlet and shows no constriction. Decreasing the opening angle towards an orifice increases the constriction. Here, the jet is accelerating after leaving the nozzle or orifice. This effect cannot be captured if the measured velocity profile is the boundary condition at top of the nozzle, because the resulting jet can only decelerate after the boundary where the real jet will accelerate after leaving the nozzle.

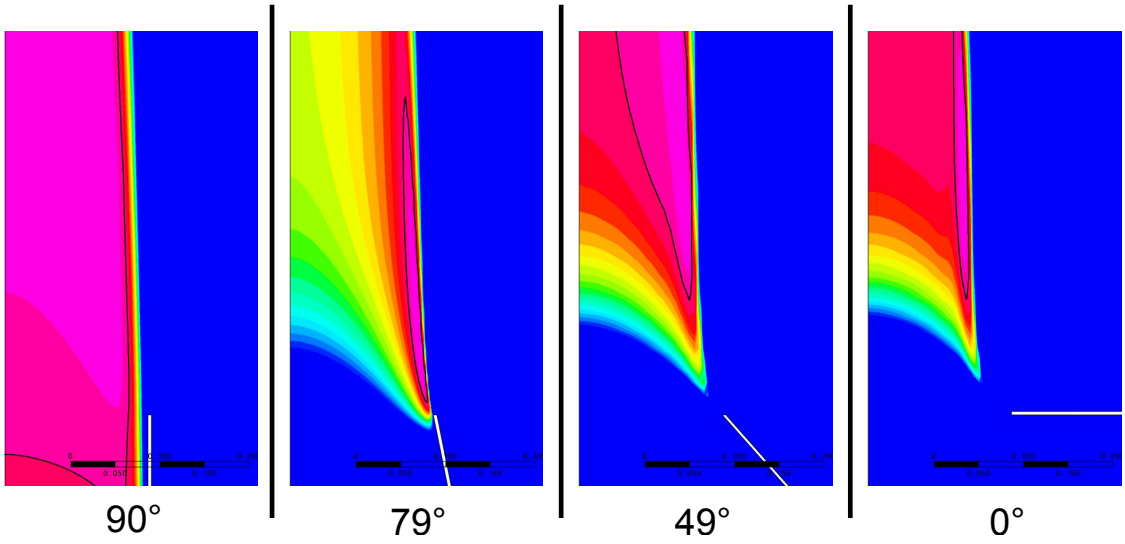

Fig. 16: Change of the stream-wise velocity of a jet depending on the origin

To solve those problems, the interior of the inner cylinder is also part of the integration domain and there are no inlet or outlet boundaries. The fan is modelled as a momentum source. The volume of the fan in the 2D-wedge is $3.3 \cdot 10^{-4} m^3$ and the applied momentum is $10.43 \frac{kg}{m^2 s^2}$, which is determined iteratively using velocity measurements of a pilot test of the inner cylinder. All walls are modelled smooth without slip. Symmetry boundary conditions are used for the symmetry axis and the sides.

2.6.2 Steady Case

For the steady case, two integration domains are used. A two-dimensional domain is used for the RANS-simulations and a three-dimensional domain for the large eddy simulation.

Fig. 17 shows the geometry of the steady case with the inlet and outlet boundaries on the left-hand side and the initial helium distribution on the right-hand side. The geometry of the steady state is a round cylinder with 1000 mm height and a radius of 500 mm. The air-inlet has a radius of 100 mm. The outlet is modelled as a nozzle to ensure a smooth outflow and to prevent non-physical behaviour, like recirculation across the outlet.

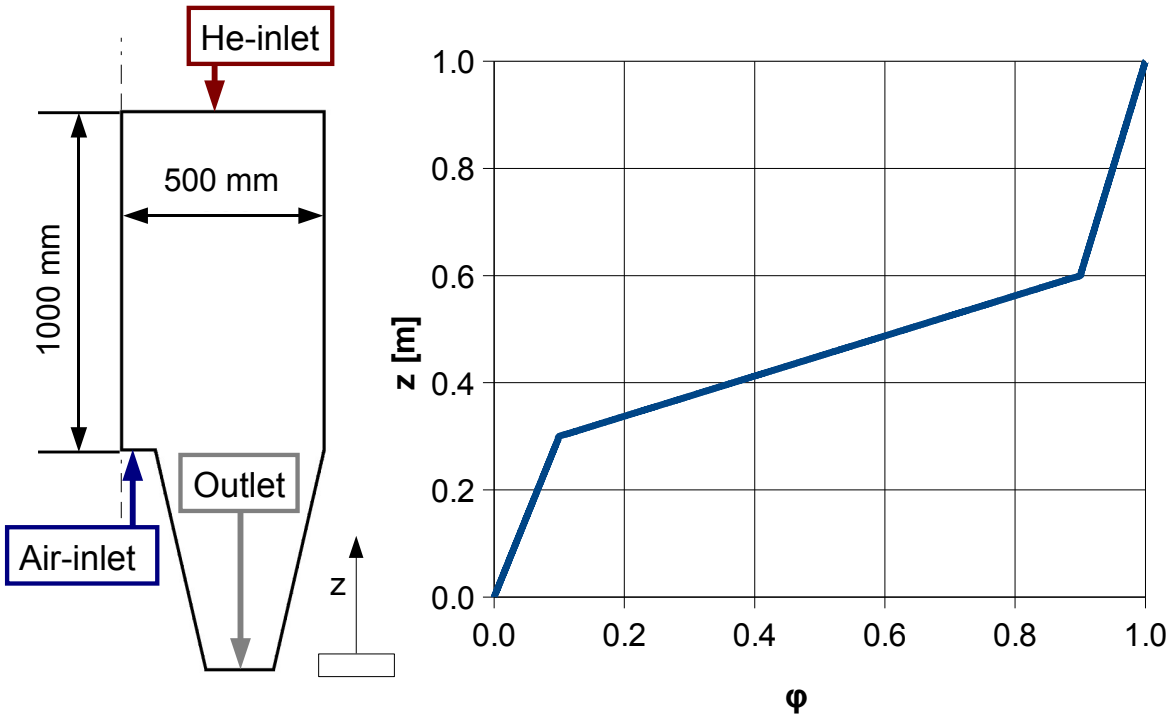

Fig. 17: Steady Case: integration domain (left) and initial helium distribution (right)

The boundary condition at the air inlet is a constant velocity of $2\frac{m}{s}$ with low turbulence intensity. The effects at the origin of the free jet in the experimental case, like the 'vena contracta' effect, can be neglected in the steady case. This is possible, because the reference investigation, the large eddy simulation, has the same boundary conditions as the simulations with RANS-models, and the influence of the origin of the jet on the mixing of the stable stratification is not the focus of this work.

The boundary condition at the helium inlet is a mass flow of helium. The mass of helium flowing into the domain is equal to the mass of helium leaving the domain through the outlet. This way a steady state will be reached after a certain time. Using this approach to model the helium inlet provides a quantity to measure the quality of the mixing, since the helium mass flow increases with a better mixing.

Another approach to model the helium inlet would be a constant mass flow of helium, adjusted to the expected quality of the mixing. Using this approach gives an optically accessible way to measure the quality of the mixing, since the final density layer will be closer to the helium inlet, the better the mixing is. But there are several problems. The helium mass flow can not be determined a priori. So an initial simulation with the variable helium inlet has to be performed, to get an idea about the range of the helium mass flow. All simulations have to use the same helium mass flow to ensure comparability. This yields problems if the results of the used turbulence models deviates much. Finally, experience showed that the constant helium boundary needs significantly more time to converge than the

variable boundary.

The initial helium distribution (Fig. 17, right) has a sharper density gradient and a larger helium concentration in the upper part compared to the experimental case. This leads to a more stable stratification and is necessary to keep the integration domain this small. If the stratification is less stable, the interaction area between jet and stratification consumes more space which would result in a larger integration domain and a longer simulation time. This would negate one important advantage of the steady state.

A summary of the initial and boundary conditions can be found in appendix A1.

3 Numerical Method

All simulations are carried out with the commercial CFD software ANSYS CFX. ANSYS CFX is a general purpose CFD suite containing a physics pre-processor, a numerical finite volume solver and a post-processor. The first simulations of the experimental case and the test simulations of the steady case have been carried out with version 11. All other simulations were performed with version 12. The use of the customised solver executable to use the TSF model is explained in appendix A2.

3.1 Numerical Parameters

In this chapter, the numerical parameters will be presented, as well as necessary set-up preparations for post-processing. The physical parameters, the boundary conditions, have been discussed in chapter 2.6. First, the parameters for the experimental case will be explained, following by the steady case. The chapter will be concluded with the numerical parameters of the large eddy simulation.

3.1.1 Experimental Case and two-dimensional Steady Case

The numerical parameters to simulate the experimental case are the same with and without using the TSF model except the changes to the CCL to activate the TSF model. It is a transient calculation with a constant time step of 0.01 s and an initial time step of 0.001 s. The transient scheme is first order backward Euler. The first order transient scheme is necessary to ensure a stable run with the customised solver.

Buoyancy production and dissipation are activated for the turbulence model. In the solver control, the turbulence numerics are set to first order.

The spatial advection scheme is high resolution. The choice of a spatial advection scheme in CFX is realised through a blending factor β. This factor is blending between a first and a second order upwind differencing scheme.

$$U_{ip} = U_{up} + \beta \nabla U \cdot \Delta \psi \tag{3-1}$$

U_{ip} is the value of the integration point, U_{up} is the value of the upwind point, ∇U is the average value of the adjacent nodal gradient and ψ is the vector from the upwind node

to the integration point [80]. So with β=1 it is a second order upwind scheme. Because it is unbounded it may lead to non-physical oscillations in regions of rapid solution variation. The high resolution scheme is of second order where possible, with β=1. To prevent the non-physical oscillations it is decreasing the value of β where necessary.

The maximum number of iterations (coefficient loops) per time step is 20, the minimum number of iterations is two. The convergence criterion is a maximum residuum of 10^{-3}.

An important step for the post-processing of the experimental case is the definition of monitor points for the helium concentration. The position of those points is the position of the measuring points in the experiment, see Fig. 18. Using the monitor points, the mixing of helium can be analysed during the solver run. It would be possible to generate the mixing curves later with the CFX post-processor, but this requires transient result files in the frequency of the desired resolution of the curves. So it is highly recommended to use the monitor points, because here the values of every time step are available.

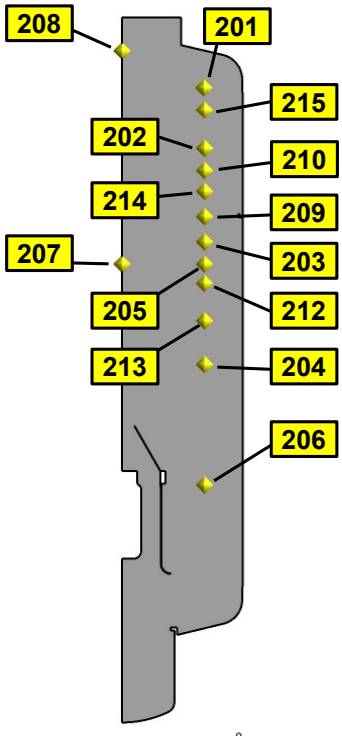

Fig. 18: Position of the monitor points in the experimental case

The numerical set-up for the two-dimensional steady case is similar to the set-up of the experimental case. It is also a transient calculation with the same time step of 0.01 seconds. Once it reaches the steady state, small fluctuations of certain values, like Reynolds stresses can occur. Therefore a transient averaging of those values can be performed, since the average value is constant due to the steady state.

3.1.2 Steady Case – Large Eddy Simulation

The numerical set-up for the large eddy simulation is characterised by the aim to resolve the three-dimensional eddies in space and time. This leads to considerably higher computational effort compared to a RANS simulation, because a LES needs a much finer and three-dimensional grid and a smaller time step size.

For the transient set-up, the total time of the LES is 20 seconds calculated with a time step of a millisecond. The second order backward Euler scheme is used for the time discretisation. After 10 seconds, a statistically steady state is reached. Transient averaging for post-processing and statistics is done over the last 10 seconds.

The spatial advection scheme is the central differences scheme.

As convergence criterion a maximum residuum of 10^{-3} is used. The maximum number of iterations per time step is 10. Due to the large computational effort for a large eddy simulation, the number of iterations has to be more limited than for RANS simulations. However, there have been no convergence issues with the smaller iteration limit.

For post-processing purposes, several preparations have to be done. To investigate the quality of the LES, a spectral analysis has to be performed (see chapter 2.5 and Fig. 14). To do so it is mandatory to define monitor points in the integration domain to monitor at least the velocity and the helium concentration. Fig. 19 shows the distribution of the monitor points for the LES. The horizontal position is at x=0 m and at x=0.3 m. The vertical position is at z=0.2 m, z=0.4 m, z=0.6m and z=0.8m. This distribution ensures time resolved data at various positions inside and beside the jet as well as below and above the density layer.

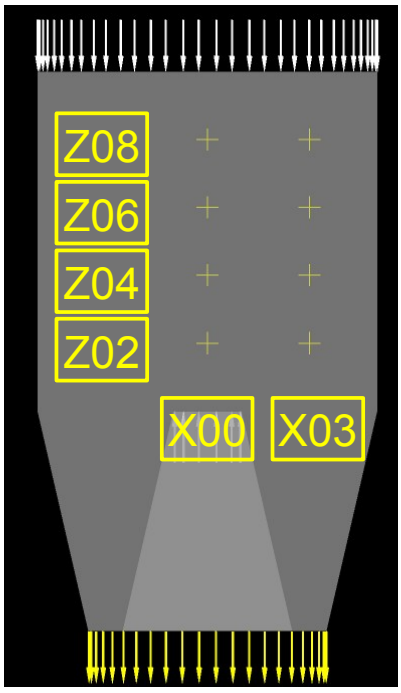

Fig. 19: Monitor Points of the Steady Case LES

It is necessary to have the data of every time step available to resolve the fluctuations with higher frequencies. It would be unreasonable to get this data through transient result files, due to the size of the files (500 MB) and the necessity to save every time step. The needed hard-drive space to have a transient result file every time step for the desired ten seconds statistical time would be approximately 5 TB (10 s * 1000 1/s * 500MB). Another issue would be the time to write the files to the hard-drive during the solver run and the time to load the files during post-processing.

Another mandatory preparation is the definition of a vector to access the turbulent scalar fluxes. They can only be accessed statistically by means of transient averaging since they are fluctuating values and the mean value has to be subtracted. This is an important reason to have a statistically steady case for the large eddy simulation. A transient simulation would require a spatial averaging to access the fluctuating scalar fluxes. This could be done circumferentially. The problem with this approach would be the low number of grid points to get information from near the symmetry axis and the jet.

To calculate the turbulent scalar fluxes, an expression for every spatial direction has to be defined as the product of velocity component and helium mass fraction.

- UX = Velocity u * He.Conservative Mass Fraction

VX and WX are defined similar to UX for their velocity component.

Next, an additional variable needs to be defined, here named UPHI.

- Variable Type: Specific
- Units: [m / s]
- Tensor Type: Vector

In the definition of the fluid models, the components of the vector must be defined as the respective expression. Finally, this vector, the velocity components and the helium mass fraction have to be assigned for transient averaging.

The turbulence mass fluxes can be post-processed by subtracting the product of the transient averaged velocity and helium mass fraction from the transient average of the product of both values. For example in x-direction:

- UPHI.Trnavg X - (Velocity.Trnavg X * He.Conservative Mass Fraction.Trnavg)

Or in a general formulation without using the CFX expression language:

$$\tilde{\Phi}_i = \overline{u_i \varphi} - \bar{u}_i \cdot \bar{\varphi} \tag{3-2}$$

This is true, because if the transient averaging interval is sufficiently large, $\overline{u_i''} = 0$ and $\overline{\varphi''} = 0$.

$$\overline{u_i\varphi} - \bar{u}_i \cdot \bar{\varphi} = \overline{\left(\bar{u}_i + u_i''\right)\left(\bar{\varphi} + \varphi''\right)} - \bar{u}_i \cdot \bar{\varphi}$$

$$= \bar{\bar{u}}_i \cdot \bar{\bar{\varphi}} + \overline{u_i'' \cdot \bar{\varphi}} + \overline{\bar{u}_i \cdot \varphi''} + \overline{u_i'' \cdot \varphi''} - \bar{u}_i \cdot \bar{\varphi} \tag{3-3}$$

$$= \overline{u_i'' \cdot \varphi''} = \tilde{\Phi}_i$$

3.2 Grids

A major factor which contributes to the quality of a simulation is the calculation grid. This is especially important for a large eddy simulations, but the solution of RANS simulations depends on the grid as well.

In this chapter, the two-dimensional calculation grids for the experimental and the steady case as well as the three-dimensional grid for the large eddy simulation will be discussed. Block structured grids are used. The blocking strategy is discussed in detail because the necessary block structure is not trivial for the experimental case. The grids presented in this chapter are built following the best practise guidelines introduced in chapter 1.2.1 [22].

3.2.1 Experimental Case

To build a hexahedral grid for a pipe or similar round domain, a block structure is necessary. Not doing so would lead to degenerated elements at places where the hexahedral cells doesn't fit due to the radius as indicated by the four squares on the left hand side of Fig. 20. To solve this problem, a block structure can be utilised. The so called O-grid is a block structure of five blocks to fit a hexahedral grid into a pipe (Fig. 20, right). Responsible for the name is the shape of the central block. For other applications, fractions of an O-grid can be used. The most notable structures for the experimental case are the C-grid, which is the half of an O-grid, and the L-grid, which is a quarter of an O-grid.

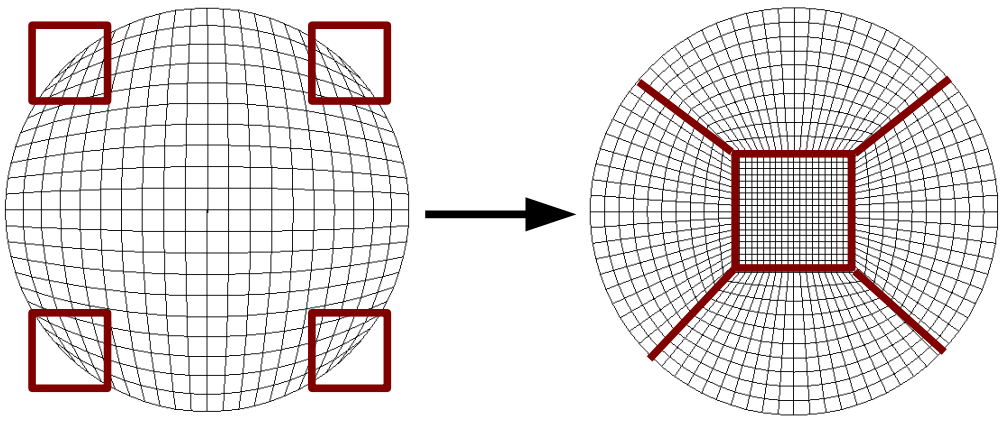

Fig. 20: left: hexahedral-grid with degenerated cells; right: O-grid structure

The geometry of the experimental case needs a nested arrangement of two C-grids and a L-grid. The left hand side of Fig. 21 illustrates the three grid types. The first C-grid is placed at the wall of the vessel (red line in Fig. 21). The second C-grid is used to describe the inner part of the inner cylinder (green line in Fig. 21). Finally the L-grid describes the wall of the inner cylinder and the shear layer of the free jet (blue line in Fig. 21).

The right hand of Fig. 21 side shows a magnification of the actual implementation of the blocking in the area around the inner cylinder. Here, the bottom part of the L-grid is visible on both sides of the wall of the inner cylinder. The C-grid inside the inner cylinder reaches up to the outlet of the nozzle. This is necessary for the grid quality inside the nozzle, because this part of the inner C-grid shares the same number of nodes with the wall of the nozzle. The actual grid in the area of the inner cylinder is shown in Fig. 22. The grid is refined towards the wall. Another refinement can also be seen in Fig. 22, the area of the jet and the interaction with the stable stratification above the inner cylinder.

The final grid has 31094 elements. A grid dependency study has been performed. According to the best practice guidelines, the grid was strongly refined to 74854 elements. Then, the refined grid was refined a second time to 310467 elements, which is ten times the original grid. It turned out, that the original grid with 31094 elements is sufficient because the use of a finer grid yields the same results.

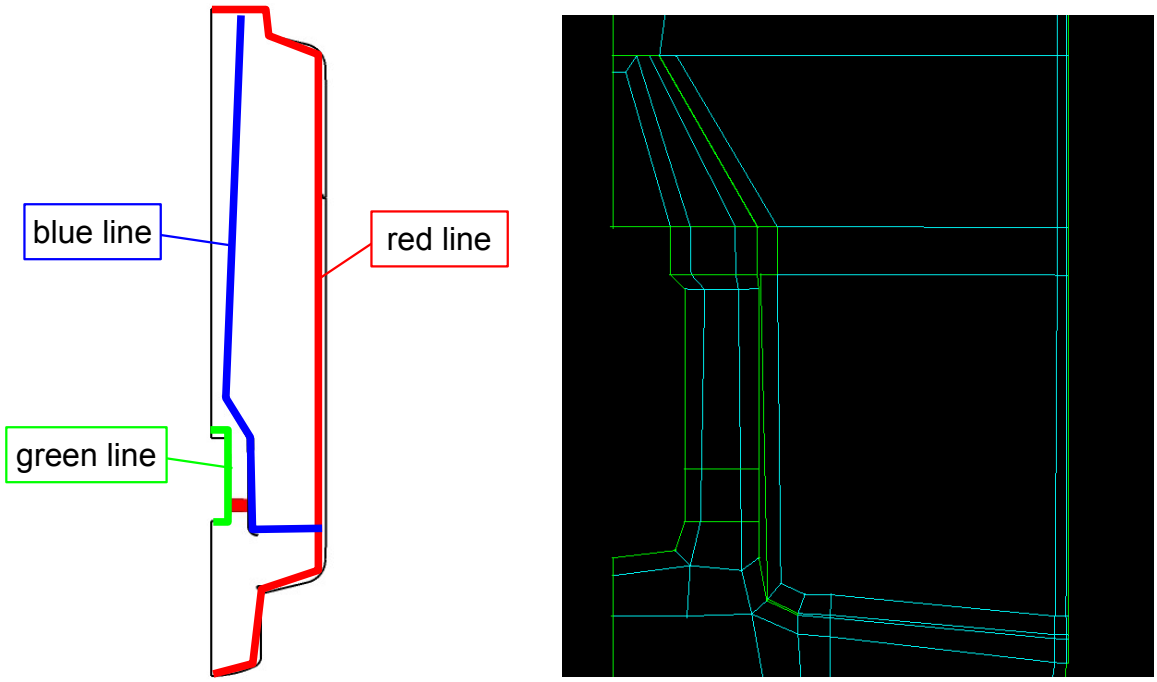

Fig. 21: left: blocking strategy for the experimental case; right: close-up view of the inner cylinder

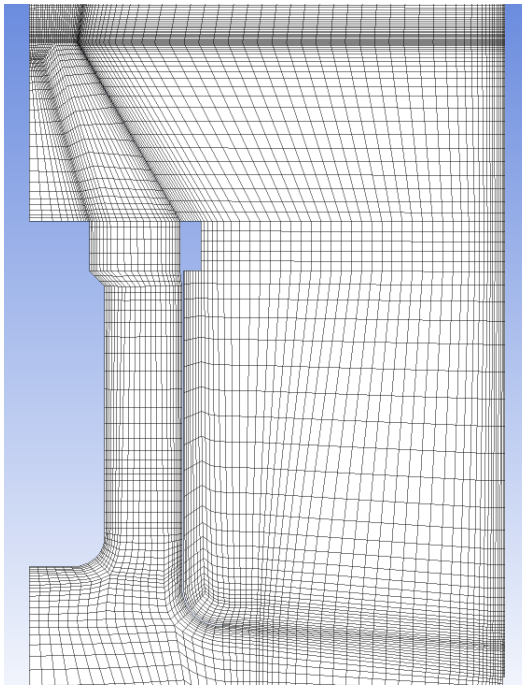

Fig. 22: Grid in the area of the inner cylinder of the experimental case

3.2.2 Steady Case

One design goal of the two-dimensional steady case was to make a high-quality, equidistant grid possible without the need for many elements.

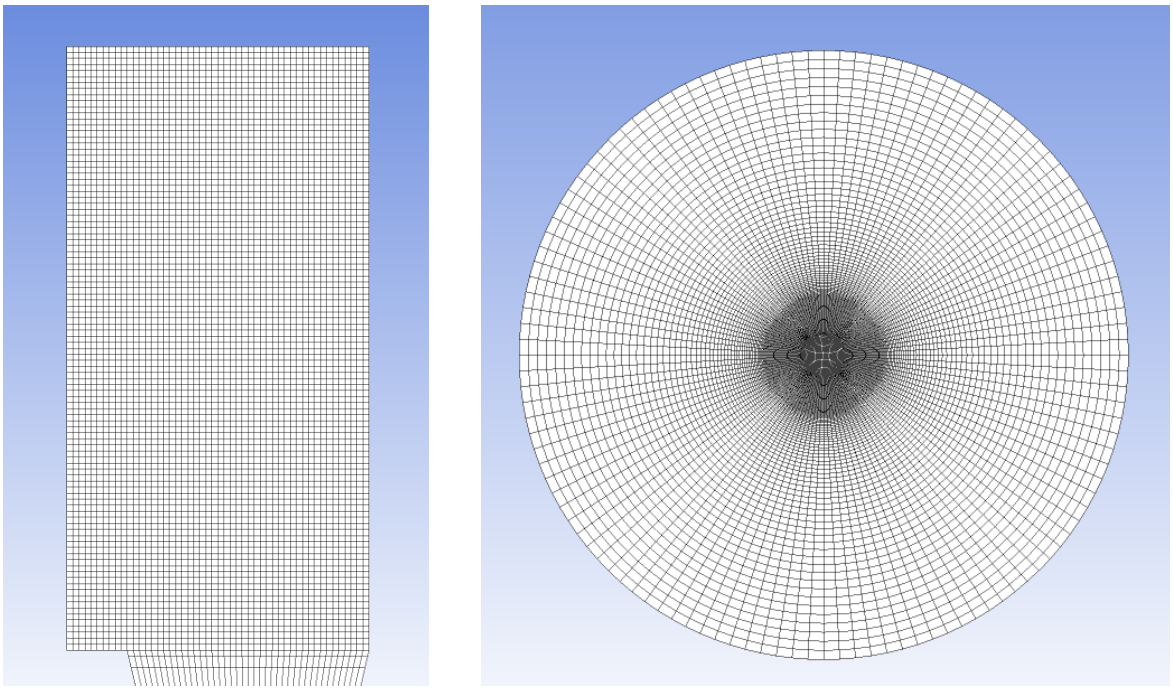

Fig. 23: Steady case: left: side-view of the 2D grid; right: top-view of the O-grid of the LES

The edge length of the elements is 10 mm. This leads to a grid size of 5760 elements, see the left hand side of Fig. 23. No near wall refinement was done, because the wall has no influence on the actual mixing, which happens in the centre of the geometry. Due to the third dimension and the cylindric character of the grid for the large eddy simulation, an O-grid is necessary. This means that an equidistant node distribution is not possible in radial direction, except for the central block of the O-grid. The right hand side of Fig. 23 shows the top view of the LES grid. The three-dimensional grid for the large eddy simulation has $2.463 \cdot 10^6$ elements.

3.3 Test Simulations

In this chapter, the preliminary simulations for the steady case are discussed. The aim of this test simulations was to identify and quantify the impact of the turbulence model for the Reynolds stresses on the mixing.

Two different turbulence models are used for this simulations, the non-isotropic ω-RS model and the isotropic k-ω model. Both simulations use the isotropic eddy diffusivity model to calculate the turbulent mass fluxes.

The left hand side of Fig. 24 shows that the resulting helium distribution is almost identical in both cases. This is also true for the velocity. The right hand side of Fig. 24 shows the vertical velocity. The main upward flow is the free jet, which is redirected by the density layer due to the stable stratification. The main downward flow is in both cases very close to the jet. The main flow never reaches the outer wall of the vessel. The results of the large eddy simulation and the TSF model in chapter 4 will prove this behaviour wrong.

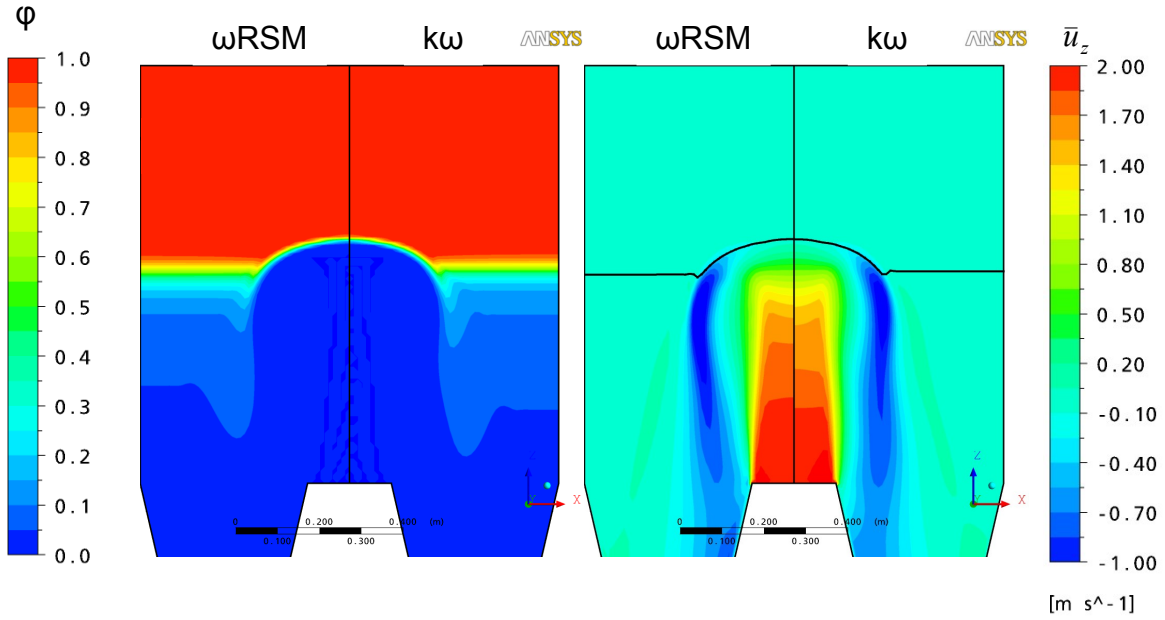

Fig. 24: Test simulations, left helium distribution, right vertical velocity

To investigate the similarity of the results closer, turbulent values are analysed. During the post-processing of a two-equation model, the Reynolds stresses can not be accessed directly. They have to be calculated using the Boussinesq approach.

$$-\tilde{\tau}_{ij} = \nu_t \cdot \left(\frac{\partial u_i}{\partial x_j} + \frac{\partial u_j}{\partial x_i} \right) - \frac{2}{3} k \, \delta_{ij} \tag{3-4}$$

The last term of equation (3-4) is the turbulent kinetic energy k multiplied with the Kronecker delta δ_{ij} . The Kronecker delta is 1 when i=j and 0 otherwise. This term is necessary to make equation (3-4) applicable for the normal stresses [71]. The part of (3-4) with the velocity gradients for the normal stresses would yield (3-5), which is zero for incompressible flows due to the continuity equation (2-1).

$$\tilde{\tau}_{ii} = -2 \nu_t \frac{\partial u_i}{\partial x_i} \tag{3-5}$$

The definition of the normal stresses is, that they are positive and their sum is twice the turbulence kinetic energy.

$$k = \frac{1}{2} \left(\widetilde{u_1'' u_1''} + \widetilde{u_2'' u_2''} + \widetilde{u_3'' u_3''} \right) \tag{3-6}$$

Fig. 25 shows that the Reynolds stresses calculated with the ω-RSM are different than those calculated with the k-ω model. This is expected, because the two-equation model is not capable of calculating the anisotropies of the flow.

So, the mixing calculated with both models is almost the same despite the difference of the Reynolds stresses. The reason for this is the dominance of the scalar flux model. As stated above, the eddy diffusivity model (2-20) is used in both cases to calculate the turbulent mass flux. And the difference of the Reynolds stresses can't influence the mixing if there is no difference in the eddy viscosity, because only the eddy viscosity is used in the eddy diffusivity model to consider turbulence.

$$\nu_t = \frac{k}{\omega} \tag{3-7}$$

It turns out, that both cases have a similar distribution of the eddy viscosity (Fig. 26).

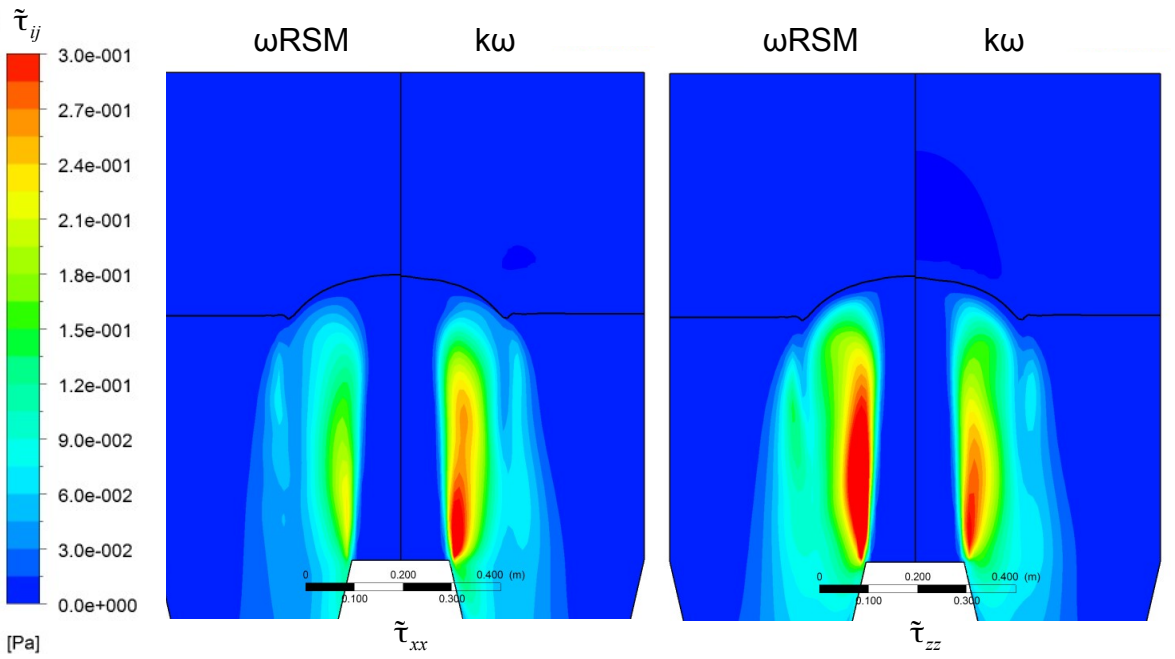

Fig. 25: Test simulations, Reynolds stresses

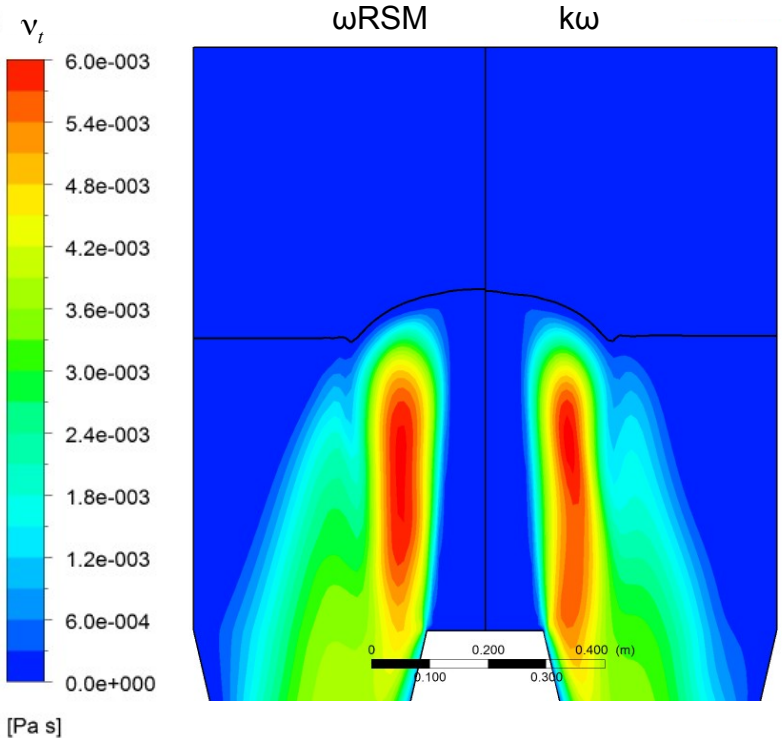

Fig. 26: Test simulations, eddy viscosity

The resulting turbulent mass fluxes can be post-processed by implementing an expression for every spatial direction of the eddy diffusivity model (2-20). In this case, the turbulent mass flux in horizontal direction is labelled Jx and in vertical direction Jz. The expression to calculate Jx and Jz are

- Jx = Eddy Viscosity * He.Conservative Mass Fraction.Gradient X
- Jz = Eddy Viscosity * He.Conservative Mass Fraction.Gradient Z

The contour plots of Jx and Jz (Fig. 27) shows the similarity of both simulations, qualitatively as well as quantitatively. So it can be concluded, that the simulation of the mixing of a stable stratification with a free jet is dominated by the turbulent scalar flux model. The impact of the turbulence model for the Reynolds stresses is negligible if the eddy diffusivity model is used for the turbulence mass fluxes.

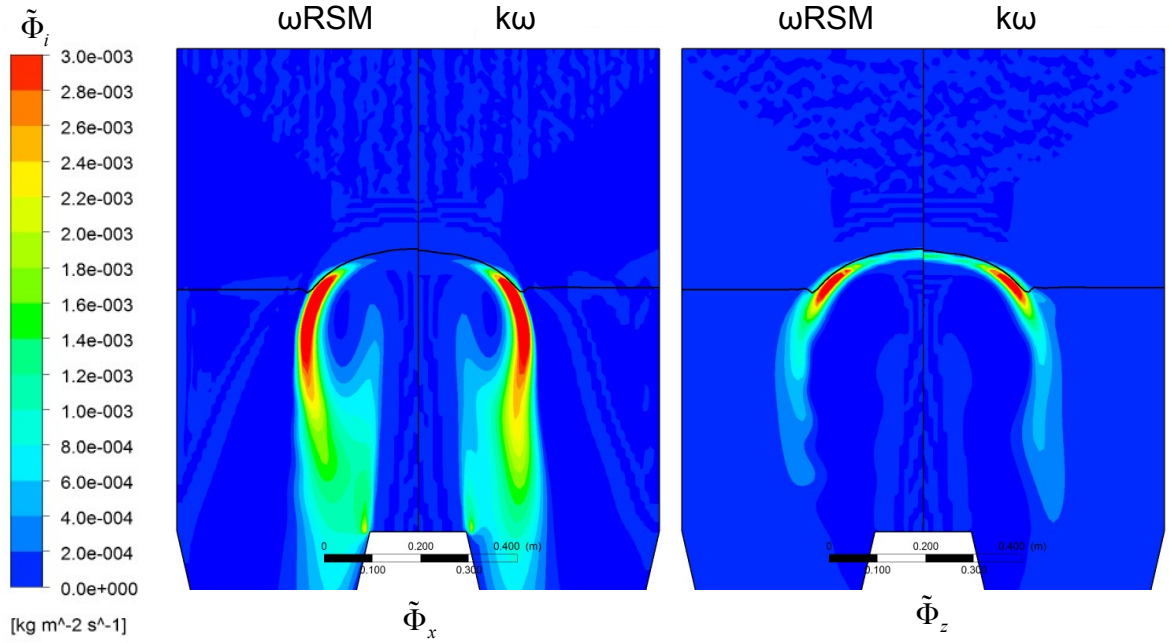

Fig. 27: Test simulations, turbulence mass fluxes

4 Results

In this chapter the results of the investigation of the steady case with large eddy simulation and turbulence scalar flux model will be discussed as well as the application of the TSF model on the experimental case.

The first step is a detailed discussion of the results of the large eddy simulations. This includes the validation of the quality with a spectral analysis.

Next, the results obtained with the TSF model will be presented and compared with the results of the LES and of a RANS simulation with the eddy diffusivity model. Then the modification of selected model coefficients will be discussed.

Finally, the TSF model will be used to calculate the experimental case. The results will be compared with the experimental data as well as with RANS simulations using the eddy diffusivity model. Then the influence of the modified TSF model coefficients will be presented.

4.1 Steady Case – Large Eddy Simulation

The discussion of the results of the large eddy simulation is separated into three parts. First, the quality of the LES will be verified with a spectral analysis. Then, the transient aspects of the LES will be presented. The discussion will cover the movement of the density layer due to its interaction with the free jet and it's impact on the transient averaged results. This is demonstrated with the velocity distribution. The third part of the chapter is about the physical values of the result. This includes the turbulence mass fluxes and the helium distribution. Time-averaged values will be investigated in this part of the chapter, since the turbulence mass fluxes are only available after transient averaging.

4.1.1 Spectral Analysis

The large eddy simulation of the steady case is carried out to have a reference case for the RANS simulations. It must be assured that the grid is sufficiently fine to resolve the large, energy-bearing eddies. As introduced in chapter 2.5, the inertial range has to be resolved to assure this (see Fig. 14, page 32).

The resolution of the inertial range also depends on the resolution of time. The time step must be small enough to capture the frequency of the eddies in the inertial range. As presented in chapter 3.1.2, the time step is $\Delta t = 0.001\,s$, which leads to the highest resolvable frequency

of 500Hz. This is due to the Nyquist-Shannon sampling theorem which states, that the perfect reconstruction of a signal needs a sampling frequency that is twice the maximum of the signal being sampled (Shannon [81], Lücke [82]). This means, that the maximum resolvable frequency of the signal $f_{sig,max}$ is half the sampling frequency $\frac{1}{\Delta t}$.

$$f_{sig,max} = \frac{1}{2\Delta t} \tag{4-1}$$

To get the spectrum of a given variable, a fast Fourier transform is performed on its time signal. For example, the time signal of the velocity at x = 0.3 m and z = 0.6 m is shown in Fig. 28. The velocity has a large amplitude ranging from below $0.2\frac{m}{s}$ up to above $1.2\frac{m}{s}$. One period from minimum velocity to minimum velocity takes approximately one second or slightly more.

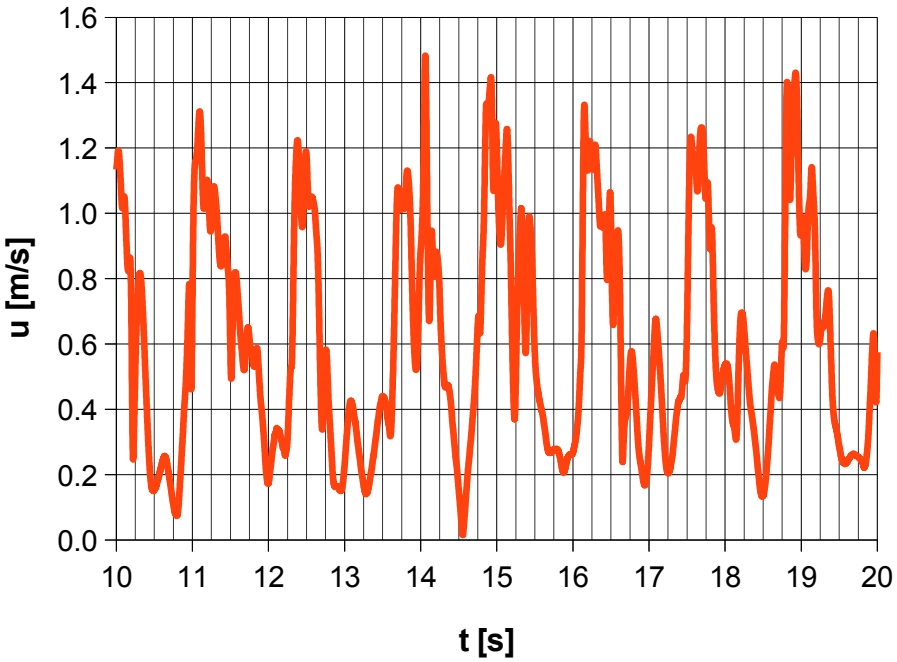

Fig. 28: Velocity at x = 0.3 m and z = 0.6 m

This large scale period is the frequency of the density layer movement. It will be shown later, that the monitor point at z = 0.6 m is at the average height of the density layer. The density layer is performing a movement similar to a see-saw, mounted on the free jet. One cycle of up and down movement takes the same time as the large scale period of the velocity in Fig. 28.

This can be explained with the stability of the stratification. In the upper position, by the time the density layer is above the monitor point, the velocity of the jet can be measured at this

monitor point. If the layer is in the lower position, for instance below the monitor point, it is preventing the jet from reaching the monitor point due to the stability characteristics.

The movement of the fluid above the density layer, in the helium cloud, is very slow. If the density layer would not have its 'see-saw' like behaviour, the only reason for a movement of the fluid in the helium cloud would be the mass flux of helium over the density layer caused by diffusion, both laminar and turbulent. But even with the impact of the movement of the density layer, the velocity is still approximately $1\frac{m}{s}$ slower than the velocity of the fluid below the layer. So the large period of over one second is not the frequency of the largest eddies, but of the movement of the density layer.

Fig. 29 show the velocity spectrum at x = 0.3 m and z = 0.6 m, with a red line to show the characteristic slope of the inertial range. The spectrum has a major peak at 4 Hz. This frequency can still easily be seen in Fig. 28.

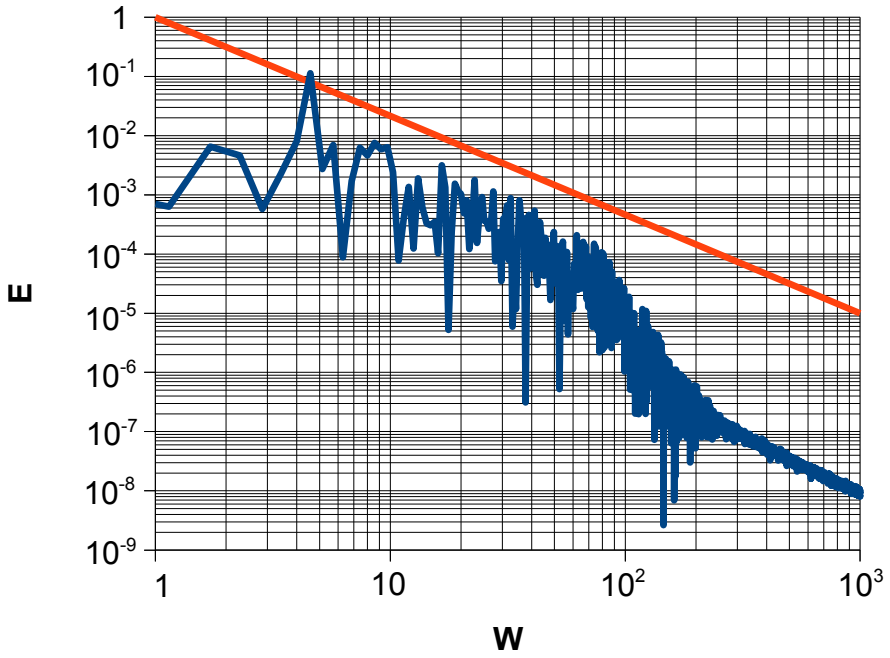

Fig. 29: Velocity spectrum at x = 0.3 m and z = 0.6 m

In the frequency region between 10 Hz and 100 Hz, the characteristic slope of the inertial range can be seen. This means, that the resolution of space and time is sufficient to resolve the large, energy bearing eddies, down to smaller eddies in the inertial range.

At higher frequencies above 100 Hz, the spectrum has a slightly steeper slope and ends at 200 Hz. The uniformly fluctuating and decaying energy above 200 Hz can no longer be interpreted as a result of the direct simulations of eddies. This is the frequency, where the capability of the grid to resolve the flow ends.

As discussed above, the sampling frequency is capable to resolve eddies up to a frequency of

500 Hz. So the resolution of time is sufficient to resolve the frequency of the smallest eddies that can be resolved by the grid, which is 200 Hz.

The analysis of the velocity spectrum at x = 0.3 m and z = 0.6 m verifies the quality of the LES in a crucial region. It has already been mentioned, that the density layer performs a 'see-saw' like movement and the average height of the layer is at z = 0.6 m. In this region, which is the same as the interaction area in the experimental case (Fig. 4, page 4), the free jet tries to penetrate the layer, gets redirected and takes in helium. Therefore the large eddy simulation is capable to calculate the region where the major fluid interactions are happening. Since the quality of grid and time discretisation is the same in the whole integration domain, it is safe to assume that the LES is also capable to calculate the flow there. The spectral analysis at all monitor points shown in Fig. 19 (page 40) verifies this assumption.

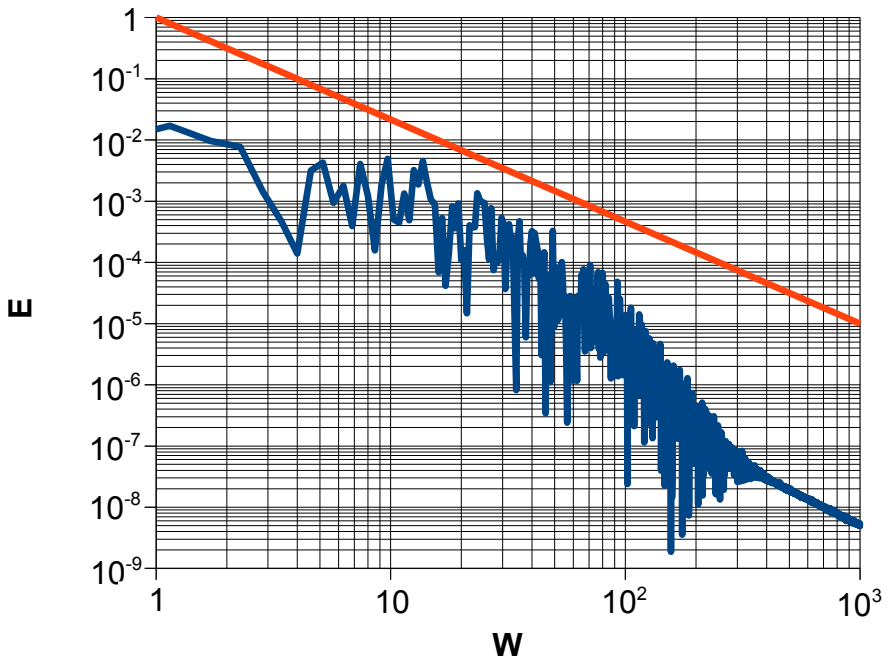

Fig. 30: Velocity spectrum at x = 0.3 m and z = 0.4 m

To demonstrate the quality of the LES outside the interaction area, Fig. 30 shows the velocity spectrum at x = 0.3 m and z = 0.4 m. This is below the range of the density layer movement. The major difference between this spectrum and the velocity spectrum at z = 0.6 m is the missing peak at 4 Hz in the spectrum at z = 0.4 m. This is a characteristic frequency of the eddies inside the range of the layer movement.

Beside this difference, the spectrum at z = 0.4 m also shows the highlighted features of the spectrum at z = 0.6 m. The characteristic slope of the inertial range between 10 Hz and 100 Hz is present as well as the slightly steeper slope above 100 Hz and the cut-off at 200 Hz.

4.1.2 Layer Movement

During the discussion of the velocity spectrum at x = 0.3 m and z = 0.6 m the movement of the density layer was already mentioned to explain the velocity fluctuations at this position in the integration domain.

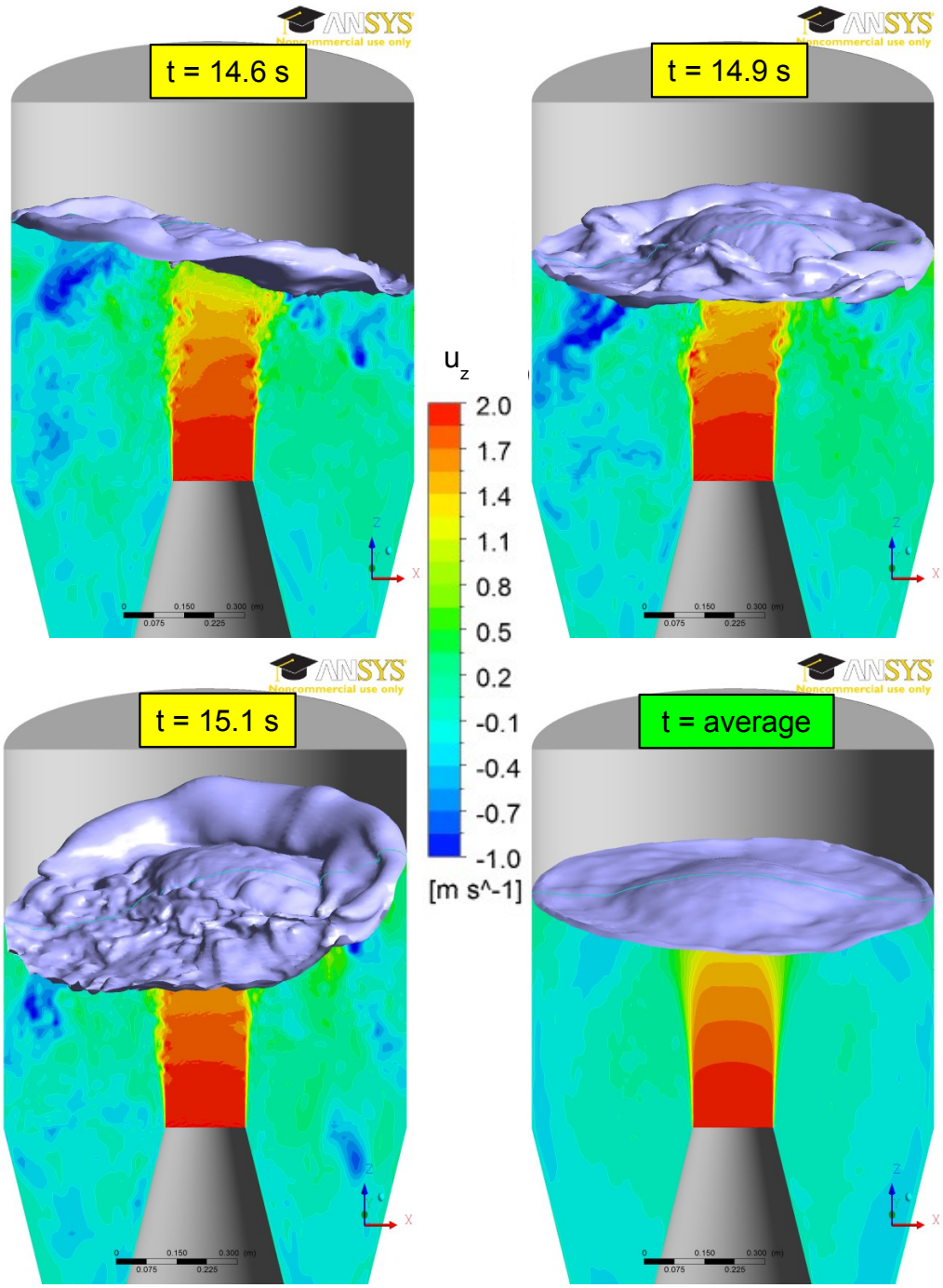

Fig. 31: Movement of the density layer and vertical velocity on the x-z plane

Fig. 31 shows a half-period of this see-saw like movement as well as the transient average inside the integration domain. The density layer is visualised as an isosurface of a helium mass fraction of 0.5. The length of one period is approximately one second. The half period shown in Fig. 31 starts at 14.6 s (denoted as position 1) and ends at 15.1 s (denoted as position 2) which is 0.5 seconds.

The xz-plane below the density layer shows the distribution of the vertical velocity. This visualises the large-scale velocity fluctuations at x = 0.3 m and z = 0.6 m, or at any other monitor point in the range of the layer's movement. The average layer is approximately at z = 0.6 m. Let us assume a monitor point on the negative x-axis for the sake of better visualisation in Fig. 31. The blue region at layer position 1, which means a negative vertical velocity larger than $1\frac{m}{s}$ is at the height of the average layer, z = 0.6 m. At position 2, the layer on the negative x-axis is below the average layer height and therefore preventing the main flow to reach the monitor point.

Another observation of the velocity distribution is the dependency of the down-flow on the layer position. This is important to consider for the comparison of the transient averaged result of the three-dimensional large eddy simulation with two-dimensional RANS simulations. A two-dimensional RANS result will have a more narrow and more distinct down-flow region, because it can not capture the three-dimensional movement.

At position 1, the down-flow on the negative x-axis comes close to the wall of the integration domain at a higher vertical position than the average density layer. In position 2, the down-flow also reaches the wall but at a lower vertical position than the average density layer. That behaviour results in a broader and less distinct down-flow region in the transient averaged velocity distributions on affected post-processing planes.

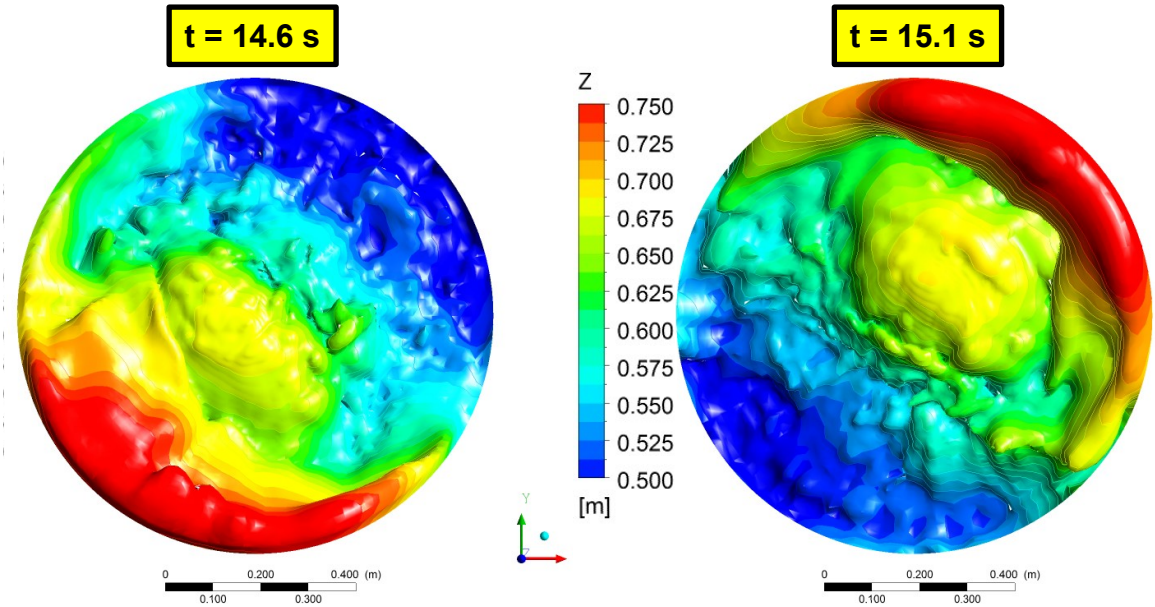

Fig. 32: Top view on the instantaneous density layer coloured with the height z

Fig. 32 shows the top view of the density layer at positions 1 and 2, coloured with the height z. At position 1, the major part of the highest region of the density layer has a negative x-coordinate as well as a negative y-coordinate. The major part of the highest region at position 2 has a positive sign for both coordinates. At first the direction of the density layer movement appears to be random. No preferred direction was provided by the initial conditions. The geometry as well as the boundary conditions are totally symmetric. But the calculation grid representing the geometry is not perfectly rotational symmetric. As presented in chapter 3.1.2 (Fig. 23, page 44), a block structured O-grid is used for the LES. Since the inner block of the O-grid is rectangular, the calculation grid has four symmetry planes, but no rotational symmetry. It turns out that the movement of density layer is following the symmetry planes through the angles of the rectangular inner block. They follow the block structure of the outer blocks (see Fig. 20, page 42).

One of those symmetry planes of the O-grid goes through the highest and lowest regions of the layer (grey line in Fig. 33, denoted 'plane max') and is therefore fully affected by the density layer movement as described above in the discussion of Fig. 31. The other plane goes through the region of the layer with the least height change (black line in Fig. 33, denoted 'plane sym'). This plane is therefore least affected by the movement of the layer.

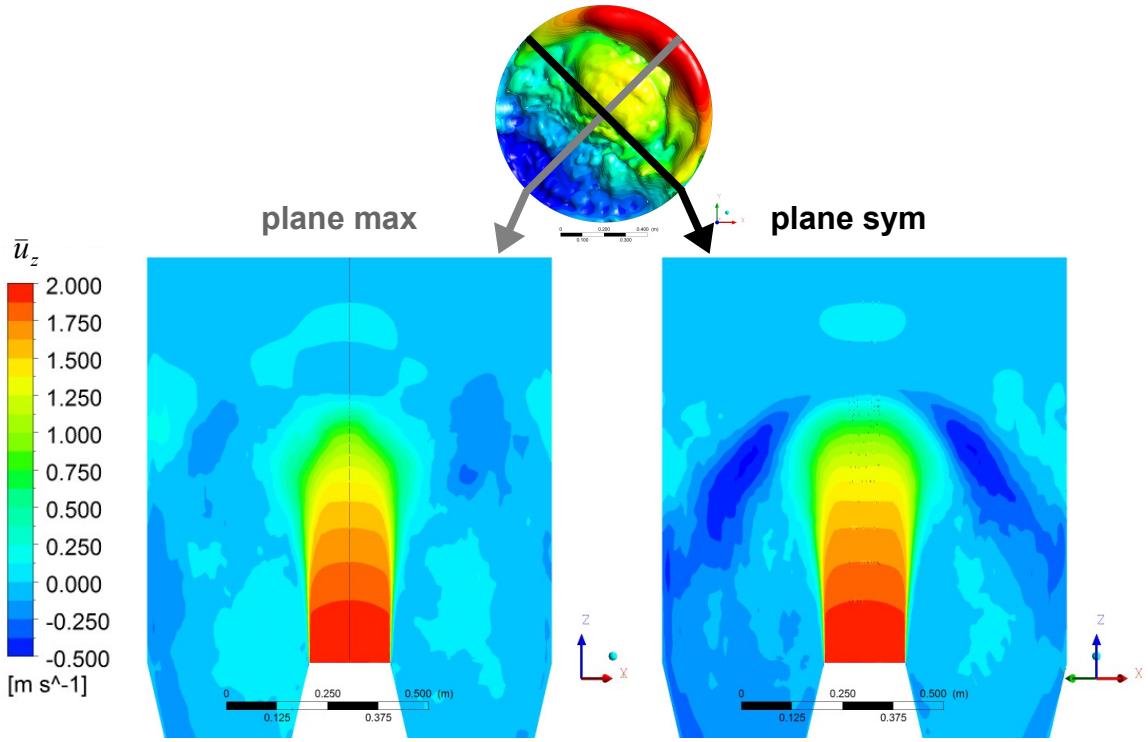

Fig. 33: Comparison of post-processing planes

The velocity profiles in Fig. 33 show the effect of the layer movement on the transient averaged velocity distribution. The left hand side shows the velocity distribution on the fully affected 'plane max'. As already pointed out, the down-flow region is broad due to the influence of the layer movement on the down-flow.

The right-hand side of Fig. 33 shows the velocity distribution on the least affected 'plane sym'. Here a distinct down-flow can be identified. The jet gets redirected by the density layer and flows in an arc downwards and to the wall. This flow situations would be expected considering the shape of the transient averaged density layer (Fig. 31).

The symmetric conditions of the density layer movement can also be seen in the distribution of the turbulent mass flux Fig. 34. The region of the transient averaged largest turbulence mass flux would have a circular shape but is stretched along 'plane max' due to the movement. It appears that the layer movement also has an effect on the turbulence mass flux near the point where 'plane max' intersects with the wall. The turbulence mass flux close to the wall in the region of 'plane max' is absent in the region where 'plane sym' intersects with the wall. This leads to the conclusion, that this turbulence mass flux is a result of a mixing effect caused by the layer movement, as this is the region of the largest movement.

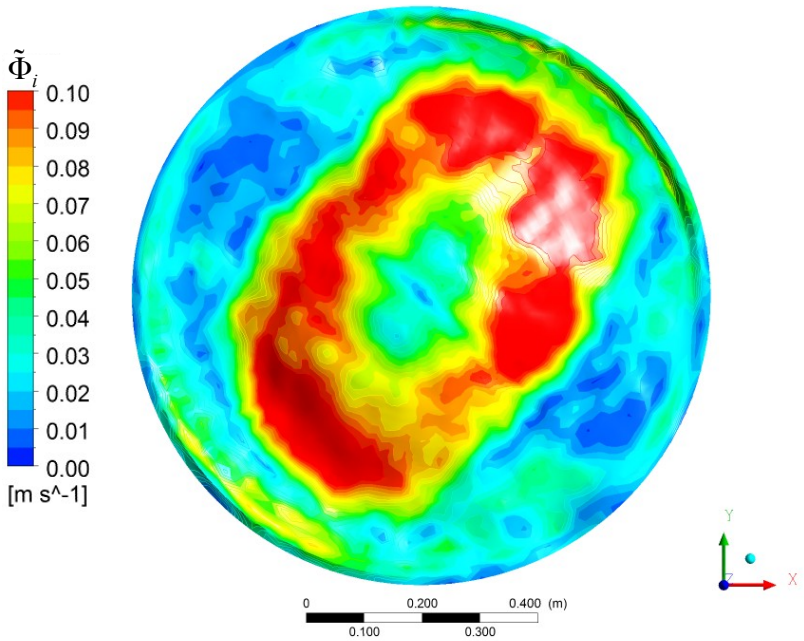

Fig. 34: Top-view of the transient averaged density layer coloured with UPHI

The annular region of turbulence mass flux near the centre of the density layer where the jet gets redirected by the layer is caused by the mixing of the jet. The turbulence mass flux is the physical effect that the turbulence scalar flux model is aimed to predict.

Considering the impact of the density layers movement on the transient averaged values at different locations is important for the comparison of the large eddy simulation with two- and three-dimensional RANS simulations. The result of a three-dimensional RANS simulation of the steady case is rotational symmetric, due to the symmetric boundary conditions and geometry, and does not capture the density layer movement. The grid of a three-dimensional RANS simulation has no influence on the result as opposed to the LES. It is therefore basically an expensive two-dimensional simulation because no additional information is gained by using all three spatial directions.

Since the results obtained with turbulence models are two-dimensional and can not capture the layer movement, 'plane sym' of the LES is used for comparison. Using this plane, a good comparability of LES and RANS results is assured because the disturbing influence of the layer movement on the transient averaged results is lower.

It was already mentioned, that the monitor point at x = 0.3 m and z = 0.6 m is in the region of the average layer height. The whole range of the layer movement is shown in Fig. 35. The minimum height can be as low as 0.42 m and the maximum height up to 0.84 m while the average height of the layer stay in the region of 0.61 m to 0.63 m.

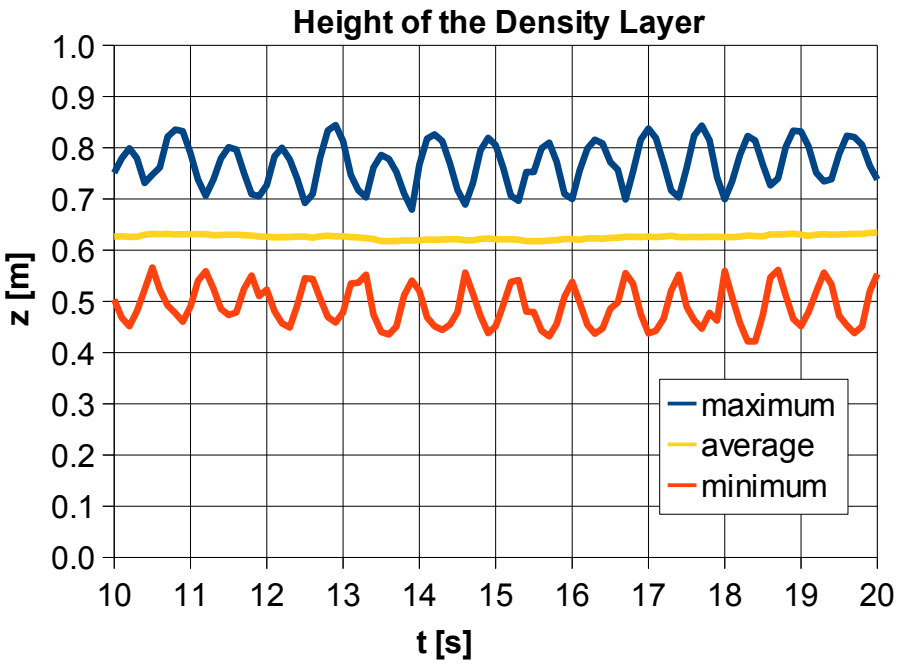

Fig. 35: Global maximum, minimum and average height of the density layer

The large scale interval already discussed with the spectral analysis (chapter 4.1.1) also appears in Fig. 35. Because the global maximum and minimum height is plotted, one period at either position 1 or position 2 is two peaks.

4.1.3 Physical Values

The discussion of the physical values of the large eddy simulation is focused on transient averaged values. The necessity to use transient averaged values is due to the accessibility of the turbulence mass fluxes. They can only be obtained by transient averaging as explained in chapter 3.1.2. Another reason is the purpose of the LES as reference for RANS simulation. The results of RANS simulations of the steady case are steady state.

The post-processing plane for the values discussed in this chapter is 'plane sym' described in chapter 4.1.2. It's the plane that is least affected by the movement of the density layer and is also used for the comparison with the RANS simulations in chapter 4.2.

The first value to be investigated is the distribution of the transient averaged helium mass fraction (Fig. 36). The distribution of the density is qualitatively the same, because the density only depends on the helium concentration. So the terms 'density gradient' and 'helium mass fraction gradient' are qualitatively exchangeable.

In the upper region of the integration domain, above the density layer, only helium is present with a mass fraction of 1.0 or close to 1.0. This situation strongly changes in the region of the density layer. The mass fraction changes in a narrow range around the density layer from almost 1.0 to below 0.2 or even 0.0 in the centre of the geometry, where the jet hits the layer.

The width of the region where the mass fraction changes depends on the position in the integration domain. It is smallest in the centre, due to the impinging jet. Closer to the wall, this range is broader. This means, that the steepest density gradient is in the centre, in vertical direction (z-direction). In general, the helium mass fraction gradient is vertically steeper than in other directions. This has an impact on the turbulent helium mass flux, as discussed later.

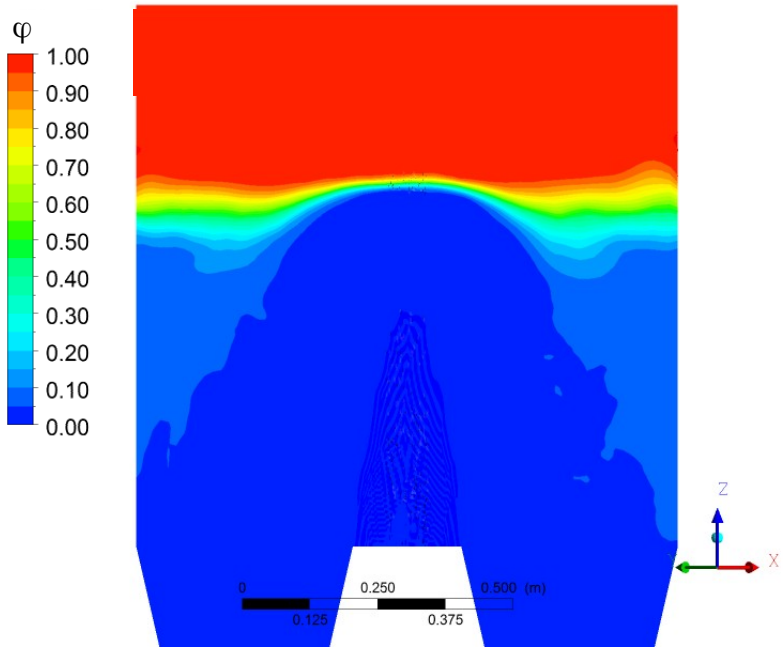

Fig. 36: LES - Average helium distribution

The lower part of the integration domain, below the density layer, is dominated by the main flow of the free jet. Almost no helium is present in the jet region. The small amount of helium in the near wall region below the density layer has a triangular shape. This helium is eventually transported out of the domain by the down-flow of the jet. The average helium mass transported out of the domain is $3.7\frac{g}{s}$.

Some aspects of the velocity have already been discussed in chapter 4.1.1 and 4.1.2. Especially the transient averaged vertical velocity on the right-hand side of Fig. 33 (page 55)

gives a first impression about the main flow of the steady case, which is driven by the free jet. A more detailed view on the flow of the steady case and the relation between it and the helium distribution is shown in Fig. 37. Originating from the air inlet, the jet flows straight to the density layer. Without the impact of the jet, the layer would be plain. The interaction of the jet and the layer forces a convex shape on the layer and causes the redirection of the jet. The jet is then flowing downwards and to the wall, forming a triangle with the density layer. Because the jet is in-taking a certain small amount of helium while trying to erode the stable stratification, this triangular shape can be seen in the helium distribution.

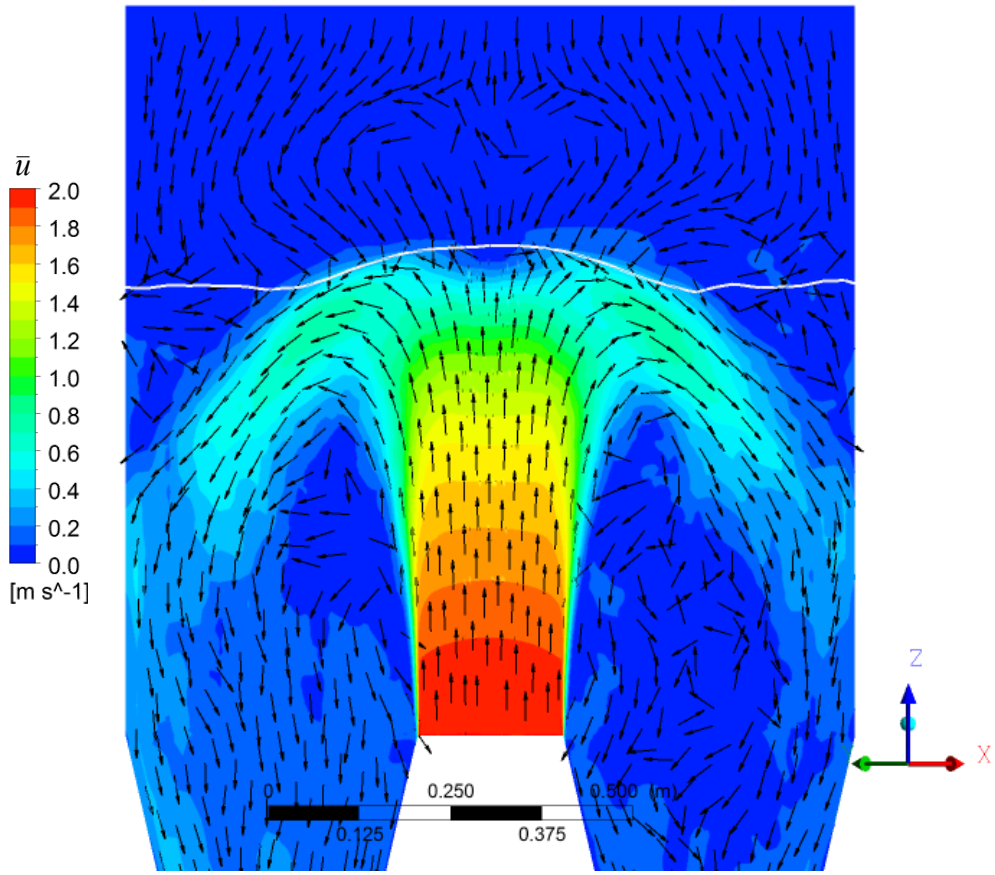

Fig. 37: LES – Transient averaged velocity with uniform velocity vectors

The region where the jet gets redirected is the main interaction region, where the largest turbulence mass flux is present. The spatial distribution of the turbulence mass flux (Fig. 38) shows that with over $0.1\frac{m}{s}$ the highest turbulence mass flux is in this region. The major part of this mass flux is in horizontal direction. The vertical component of the turbulence mass flux is only up to 20% of the total mass flux (Fig. 39).

It can also be seen in Fig. 38, that the turbulence mass flux in the centre of the geometry, and therefore in the centre of the upward jet is rather small. It is increasing with the redirection of the jet. A closer view on the interaction region is given in Fig. 40, page 61. The velocity vectors are shown rainbow scaled, combined with the turbulence mass flux grey scaled.

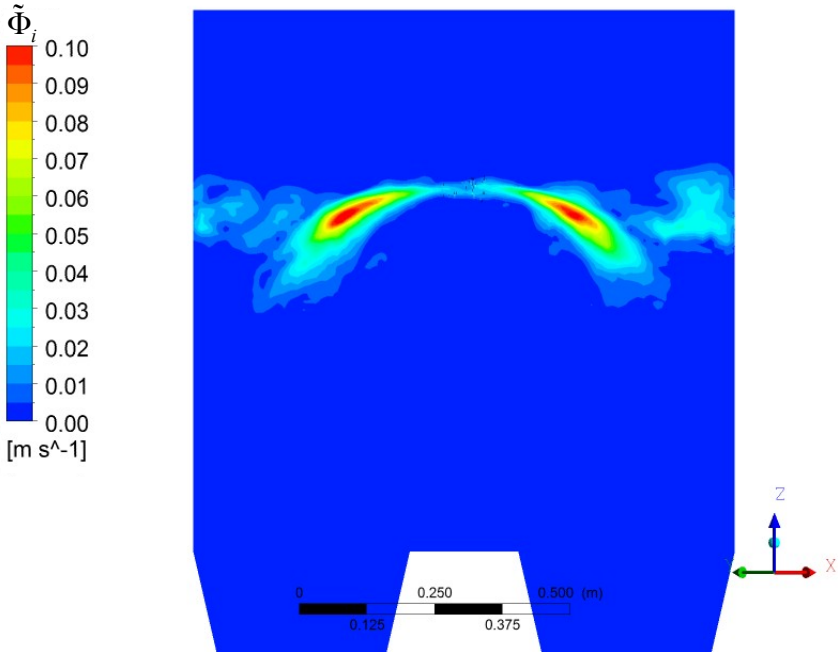

Fig. 38: LES - Turbulence mass flux distribution

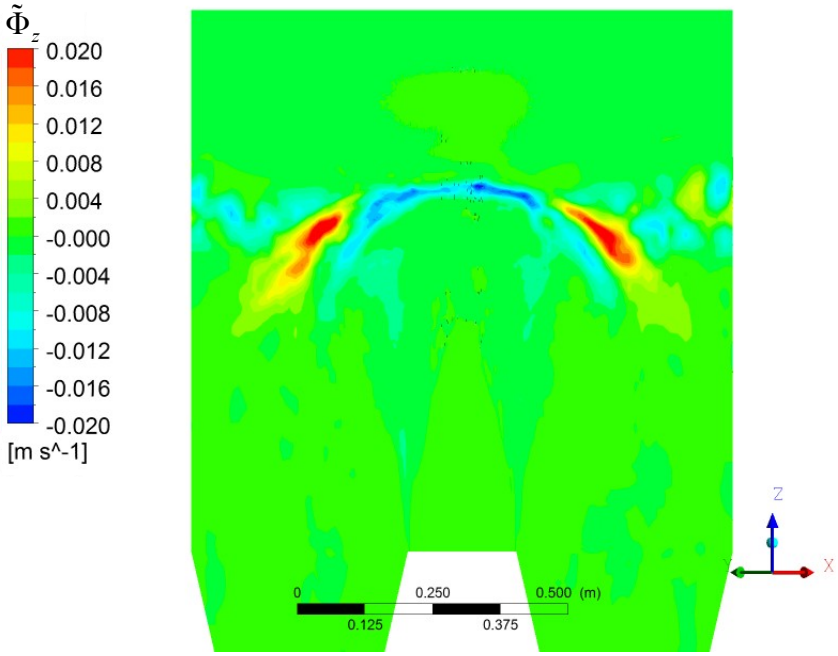

Fig. 39: LES - Vertical turbulence mass flux distribution

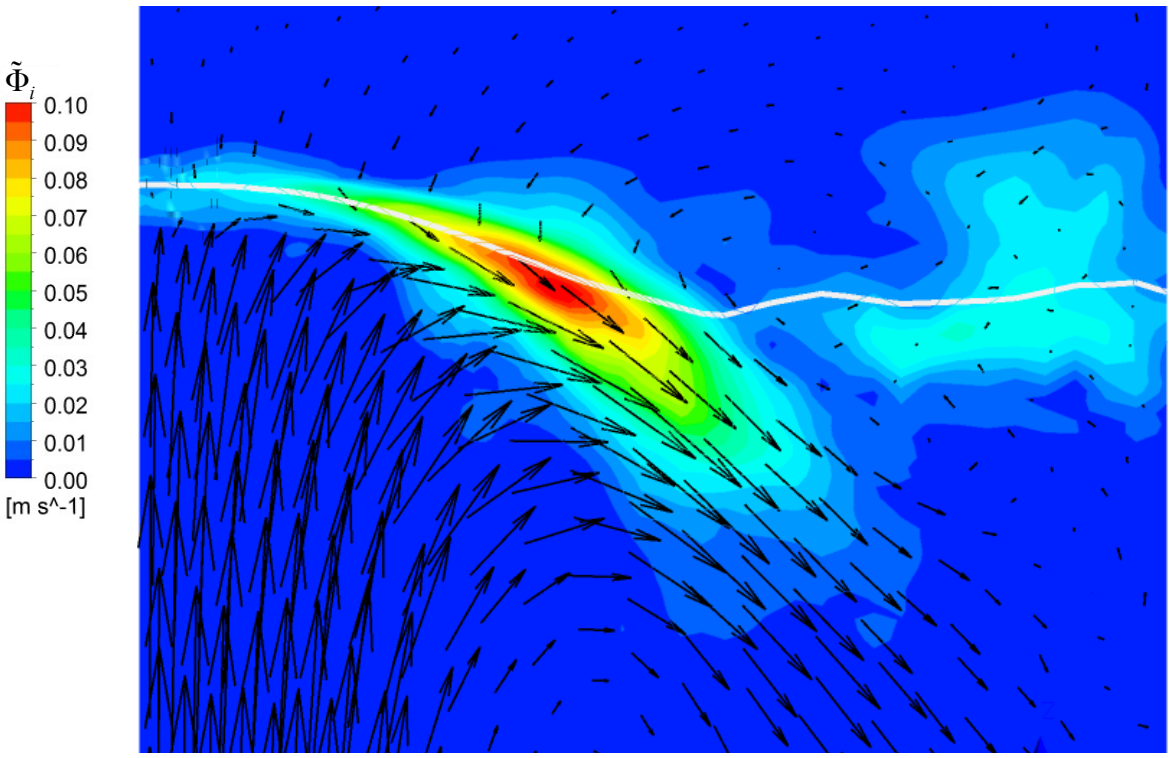

Fig. 40: LES - Velocity vectors and mass flux distribution in the interaction are

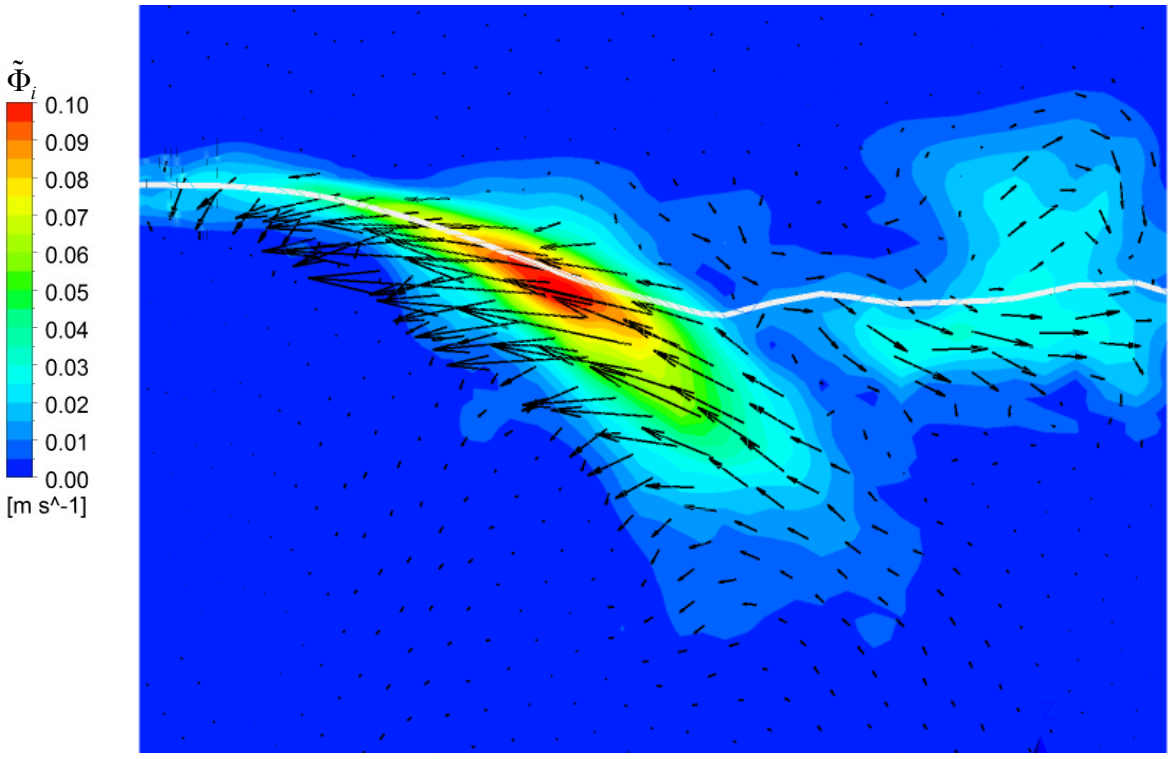

Fig. 41: LES - Turbulence mass flux in the interaction area

So the jet is in-taking a very small amount of helium during the first impact at the place where the helium mass fraction gradient of the stable stratification is steepest. The jet contains now some helium and is moving to a region where the gradient of the stratification is less steep. The helium inside the jet contributes to a less steep mass fraction gradient between jet and stratification. Since the gradient is less steep and the stratification therefore less stable, the jet can intake more helium. The main flow is also more tangential to the density layer in this region. Therefore the shear-stresses of the main flow can better contribute to the mixing. This effect has a maximum as shown in Fig. 38 and Fig. 40. In this region the best situation for the mixing is reached.

Afterwards the turbulence mass flux is decreasing again, because helium is not available for mixing any longer since the jet is moving away from the helium cloud. This can be seen in Fig. 41, where the spatial distribution of the turbulence mass flux vectors is shown.

A detailed view of the turbulence mass flux vectors and the helium mass fraction distribution the interaction region is given in Fig. 42. As discussed above, there is a rather small vertical mass flux in negative z-direction in the centre of the domain, where the jet first hits the layer. In the redirection region, the mass flux is increasing and is changing direction. It has now the tendency to be approximately tangential to the density layer. This means that the main direction of the turbulence mass flux is horizontal and slightly upwards.

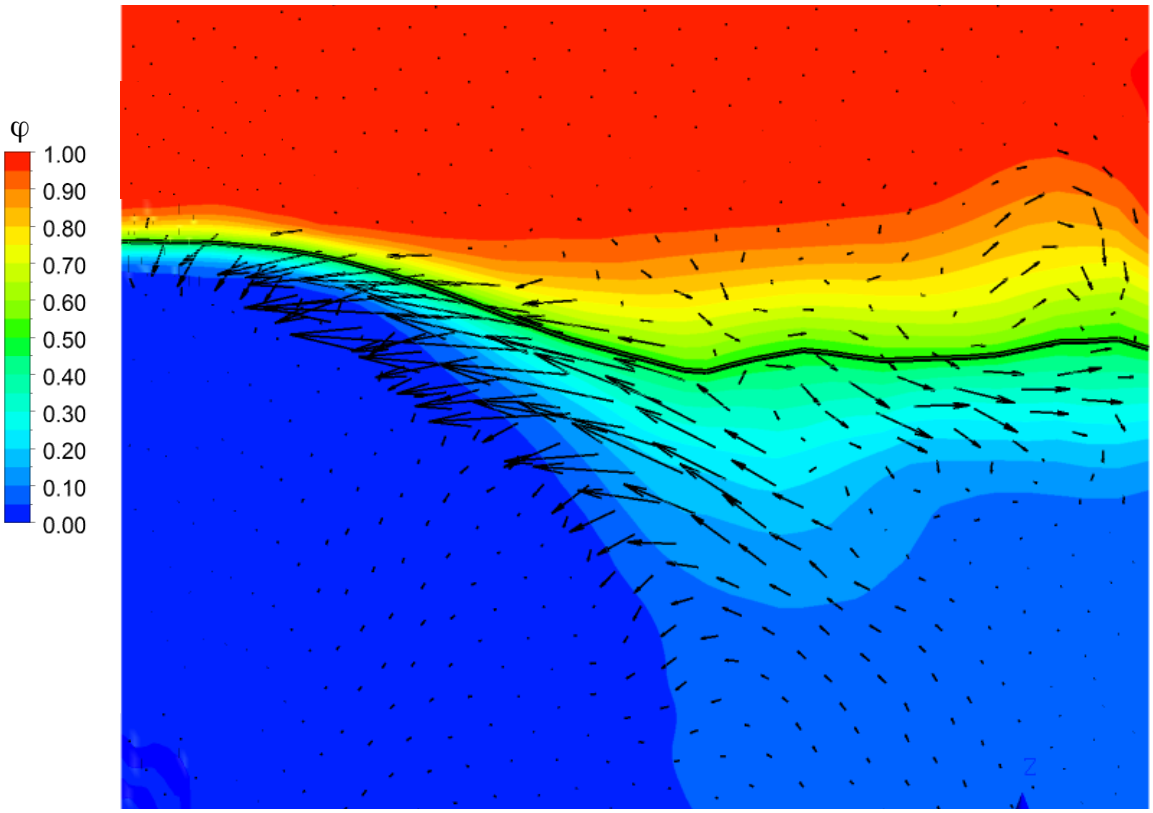

Fig. 42: LES - Mass flux vectors and helium distribution

The helium mass fraction gradient in vertical direction is much larger than the gradient in horizontal direction. Hence the turbulence mass flux in horizontal direction is larger because the helium mass fraction gradient has a damping effect on the turbulence mass flux in vertical direction. The position of the maximum turbulence mass flux is related to the distribution of helium in the integration domain and the possibility of the main flow to erode the stratification.

	Helium Mass Fraction Gradient [1/m]	Turbulence Mass Flux [m/s]
vertical maximum	45.682	0.026
horizontal maximum	10.399	0.110
vertical / horizontal []	4.393	0.238
horizontal / vertical []	0.228	4.200

Table 3: LES - Helium mass fraction gradient and turbulence mass flux

The relation between the helium mass fraction gradient and the turbulence mass fluxes can be quantified. Not only the position of the the mass flux is influenced by the density gradient, but also the strength. A steeper gradient results in a slower mass flux and vice versa. A comparison of the maximum values of both quantities in horizontal and vertical direction quantifies that relation (Table 3). The two used ratios here are vertical / horizontal (denoted v/h-ratio) and horizontal / vertical (denoted h/v-ratio). The v/h-ratio of the mass fraction gradient is four. The opposite is true for the turbulence mass flux. Here, the h/v-ratio is four.

The spatial distribution of the vertical helium mass fraction gradient can be seen in Fig. 43 and of the horizontal gradient in Fig. 44. Both figures also contain white coloured velocity vectors. The ratio of 4.39:1 between the maximum vertical and horizontal gradient can be seen.

The position of those maxima in relation to the main flow is interesting. The steepest vertical gradient is in the impact region of the jet on the layer. The jet is changing the shape of the otherwise plain density layer into a convex geometry. The layer gets pushed by the jet towards the ceiling. This results in a decreased layer width with the narrowest point located in the centre. This is the reason for the position of the steepest vertical helium mass fraction gradient, which is related with the width of the layer.

This is also a general illustration of the stable characteristic of a stable stratification. The density gradient is preventing an impinging jet to penetrate the light gas cloud. With a steeper gradient, this effect becomes stronger. During the impact, the jet is causing a steeper density gradient and is therefore increasing the stability of the stratification.

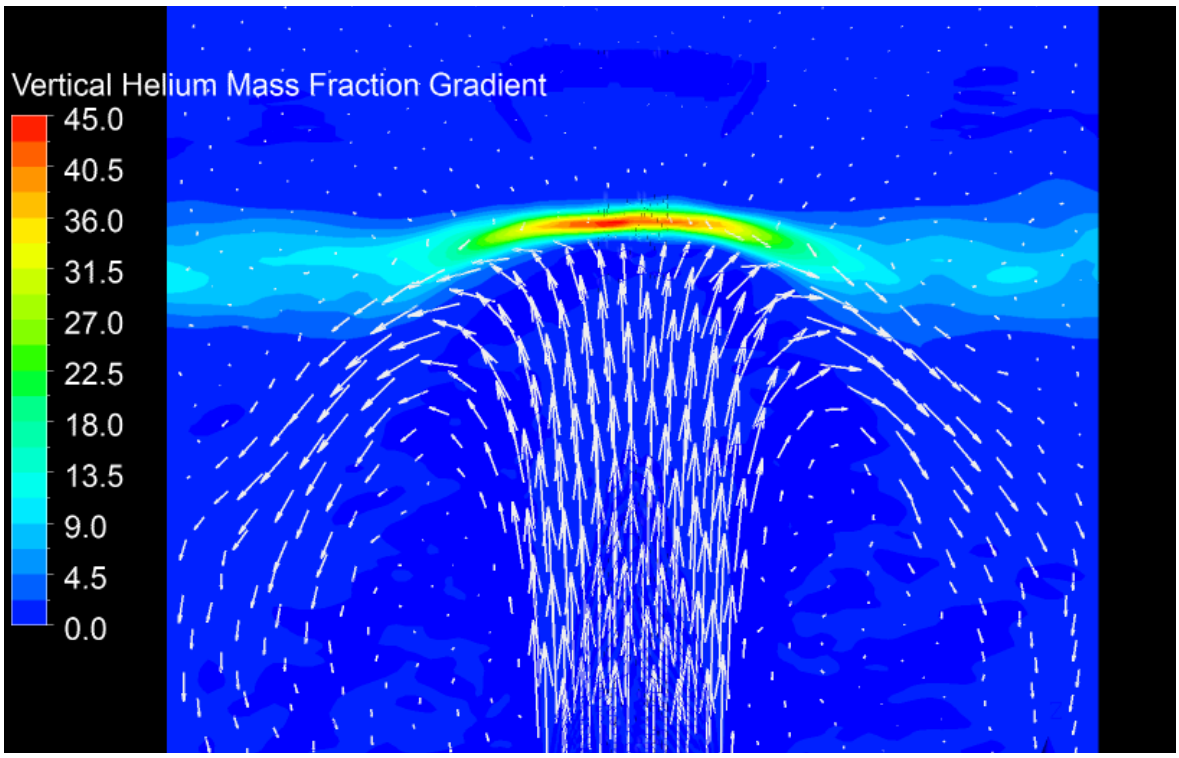

Fig. 43: Vertical helium mass fraction gradient and velocity vectors

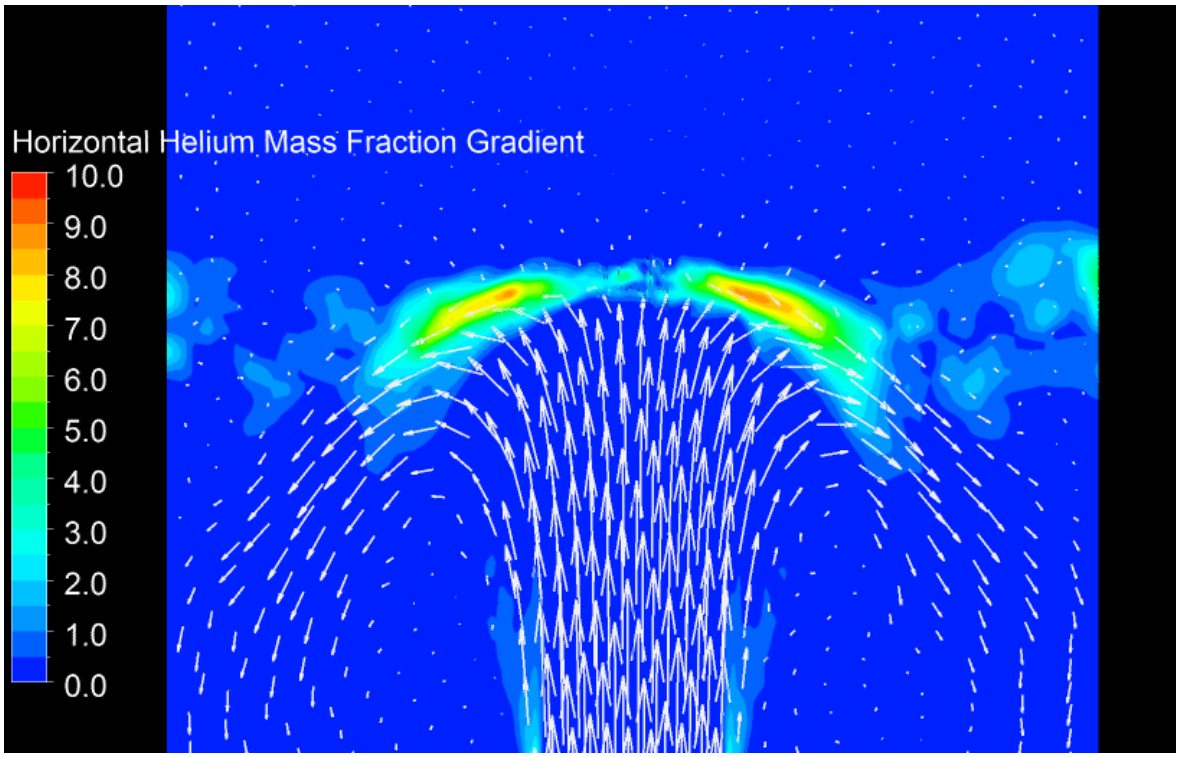

Fig. 44: Horizontal helium mass fraction gradient and velocity vectors

The jet also determines the position of the maximum horizontal helium mass fraction gradient (see Fig. 44). Here, the same effect occurs, that is responsible for the maximum vertical gradient. The jet gets redirected by the stable stratification and is now flowing horizontal. Since the density layer is now convex, the jet is hitting the layer again, this time slower and in horizontal direction. This causes another push on the layer, again resulting in a steeper helium mass fraction gradient, this time in horizontal direction. Since the jet can no longer continue in horizontal direction due to the stability of the stratification, it is again redirected downwards and to the wall.

4.2 Steady Case – Turbulence Scalar Flux Model

In this chapter the result of the steady case using the turbulence scalar flux model is discussed. In the first part, the result with the original model coefficients and its comparison to the large eddy simulation and the eddy diffusivity model is discussed.

Then, the variation of model coefficients is analysed and it is discussed, which coefficients are modified. First, the coefficient that is controlling the impact of the turbulence buoyancy production C_{3Y} is modified. The results are compared with the LES and the original TSF coefficients. Second, the coefficient that is controlling the last term of the pressure-scalar gradient correlation C_{4Y} is modified and compared to the other relevant cases. Finally the model coefficients which yield the best results are combined.

The chapter will be completed with a summary and conclusions of the investigation of the steady case.

4.2.1 TSF model results and comparison to LES and EDM

The comparison of the helium mass flow out of the domain shows that a significant improvement can be achieved by using the TSF model instead of the eddy diffusivity model (EDM) (Fig. 45).

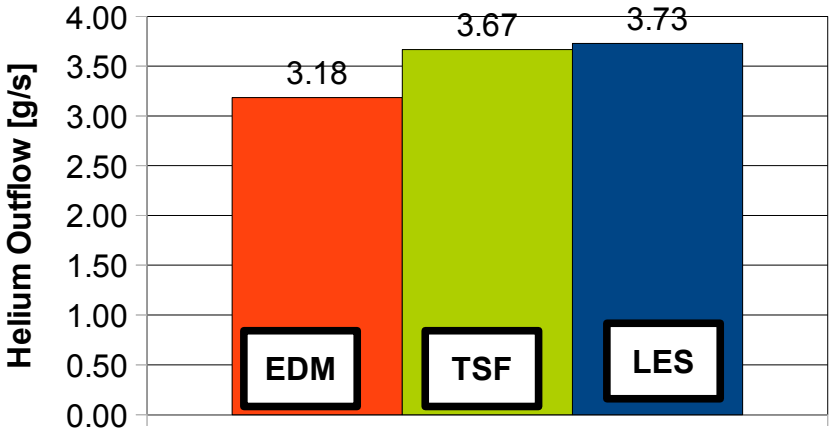

Fig. 45: Helium outflow of LES, TSF and EDM

It can be seen that the mixing with the TSF model is almost as good a with the LES. The difference of the helium outflow is only $0.06\frac{g}{s}$ which is 1.6 %. The helium outflow with the eddy diffusivity model is $0.55\frac{g}{s}$ which is 14.7% lower than the outflow of the LES.

The velocity vectors in Fig. 46 show a considerable difference between the TSF model and the EDM in the main flow below the density layer. The down-flow obtained with the TSF model follows the same direction as the down-flow of the LES. The EDM on the other hand shows a different behaviour. The down-flow happens very close to the upward jet and does not reach the wall. The difference of the flow field has also an effect on other values. For example, it causes a difference in the helium distribution.

The agreement between the TSF model and the large eddy simulation is reasonable. The redirection of the jet is similar, and the shape of the down-flow is comparable. A difference in the down-flow region is that the down-flow is more narrow in the TSF case. The reason for this difference is the absence of transient effects using the turbulence model, where the result of the large eddy simulation is affected by the movement of the density layer (see 4.1.2).

The velocity field in the lower part of the domain, near the beginning of the outlet between the upward jet and the down-flow, shows a discrepancy between the results of the LES and the TSF model. The result of the TSF model shows a circulating flow in this region. This swirl appears to be caused by the accelerating effect of the jet on the surrounding fluid. Since the LES doesn't show such a distinct swirl it can be assumed that the mixing in the shear layer of the jet is over-predicted by the TSF model.

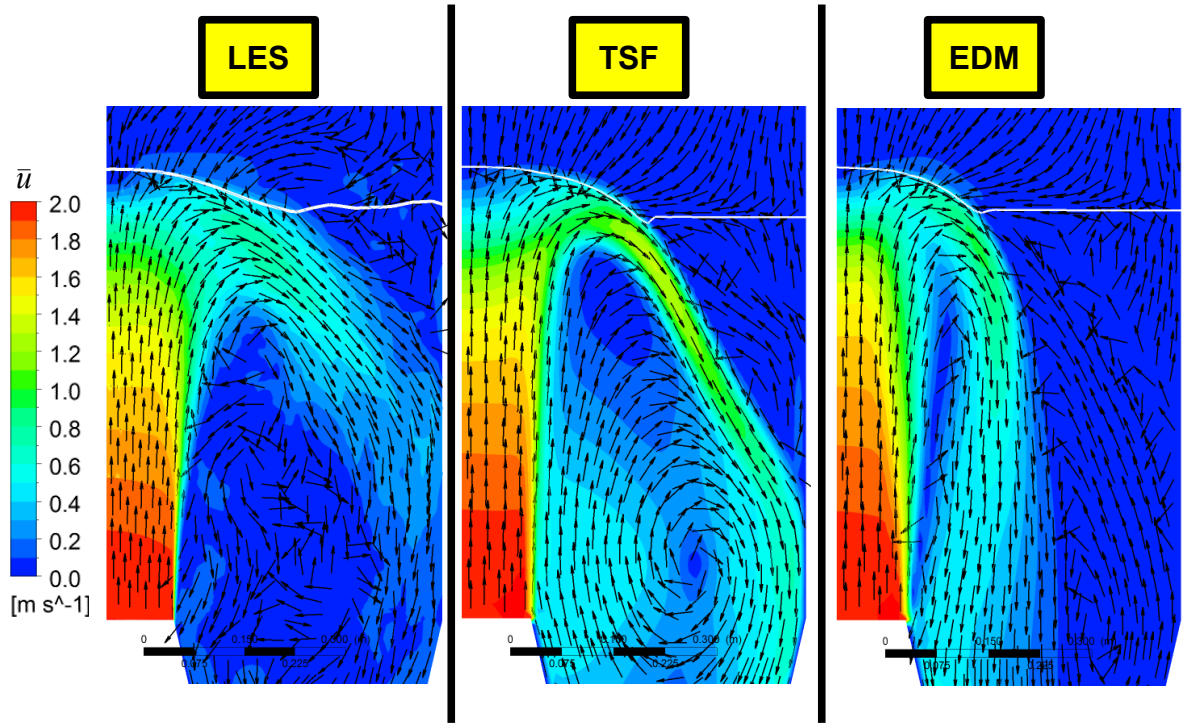

Fig. 46: Transient averaged velocity with uniform velocity vectors of LES, TSF and EDM

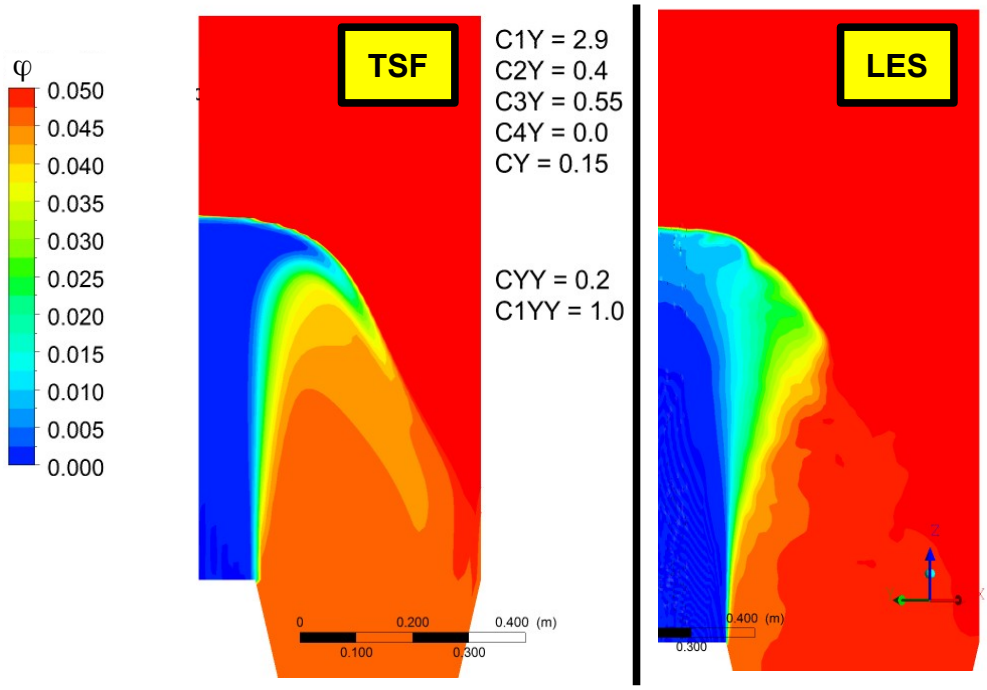

Fig. 47: Helium mass fraction 0 – 0.05 of LES and TSF model

As an assumption, the swirl could have either a negative or a positive effect on the helium outflow. The negative effect would be a blocking of the outlet, which would lead to a lesser helium outflow as the turbulence model would be capable of. The positive effect would lead to a better mixing of the stable stratification. Since a small amount of helium could be brought into the upward jet by the swirl, the helium mass fraction gradient between the jet and the stratification in the interaction area would be less steep. This, in turn, would lead to a better mixing.

A detailed comparison of the helium mass fraction distribution shows a discrepancy between the results of the TSF case and the LES (Fig. 47). It turns out that the swirl does not bring additional helium into the free jet. The smaller helium mass fraction in the lower part of the domain in the TSF case indicates, that the swirl does have a negative effect on the helium outflow. This means that the helium outflow can not be used as a value to judge the quality of the mixing. Only the turbulence mass fluxes are a reliable value to judge the mixing.

It should be noted, that the difference in the interaction area between TSF and LES shown in Fig. 47 is a result of the transient averaging of the large eddy simulation. The helium mass fraction is larger in the LES case because this region is still affected by the movement of the density layer. It can be seen in Fig. 32 (page 54) that the top of the jet is not always in 'plane sym'. Whenever that happens, the height of the density layer in 'plane sym' is lower. During one period, the highest point of the jet is passing 'plane sym' twice. This causes the blurring effect in the transient averaged value of the helium mass fraction in Fig. 47.

The comparison of the helium mass fraction gradient on the left-hand side of Table 4 shows that the maximum vertical gradient is approximately the same. However, the horizontal gradient obtained with the TSF model is twice the horizontal gradient of the large eddy simulation. This leads to a different relation of those two components. The v/h-ratio of the TSF model is only 2.14, where it is 4.39 in the LES.

The values of the turbulence mass flux of the TSF model are lower than in the LES which was not expected at first considering it has an almost identical helium outflow as the large eddy simulation. But as discussed above the turbulence mass fluxes and the helium outflow do not depend on each other due to the influence of the main flow on the helium outflow. The vertical maximum of the LES is 5.7 times of the vertical maximum of the TSF model. The difference of the horizontal maximum turbulence mass flux is even larger. Here, the result of the LES is 13.7 times larger compared to the TSF model.

	Helium Mass Fraction Gradient [1/m]		Turbulence Mass Flux [m/s]	
	LES	TSF	LES	TSF
vertical maximum	45.682	45.579	0.026	0.005
horizontal maximum	10.399	21.287	0.110	0.008
vertical / horizontal []	4.393	2.141	0.238	0.573
horizontal / vertical []	0.228	0.467	4.200	1.746

Table 4: TSF - Helium mass fraction gradient and turbulence mass flux

The relation between the helium mass fraction gradient and the turbulence mass flux, as discussed for the LES (see Table 3, page 63), can approximately still be seen in the TSF result. As already discussed, the v/h-ratio of the helium mass fraction gradient of the LES is 4.39 which is slightly larger (factor 1.1) than the h/v-ratio of the turbulence mass flux of the LES with 4.2. For the TSF case, the v/h-ratio of the gradient is 2.14, which is slightly larger (factor 1.2) than the h/v-ratio of the turbulence mass flux of 1.75.

The reason for the different horizontal mass fraction gradient is the horizontal velocity. It was already explained how the interaction of jet and density layer is creating steeper mass fraction gradients. A higher velocity leads to a steeper gradient. It can therefore be expected, that the horizontal velocity in the interaction area of the TSF case is larger than in the large eddy simulation. The distribution of the horizontal velocity is shown in Fig. 48. The absolute value of the horizontal components is used in both cases, because x and y components have to be considered in the LES.

The discrepancy between LES and TSF in the lower part of the domain in Fig. 48 is caused by

the swirl in the TSF case. But, as expected, a qualitatively good agreement of TSF and LES is achieved in the interaction area, with a greater velocity in the TSF case. The velocity distribution of the LES appears slightly blurred because of the density layer movement. The maximum horizontal velocity of the TSF model is $u_{max,h,TSF}=1.0\frac{m}{s}$ and of the LES $u_{max,h,LES}=0.71\frac{m}{s}$. The higher horizontal velocity in the TSF case is the reason for the higher horizontal helium mass fraction gradient. The relation of the maximum horizontal velocities $\frac{u_{max,h,TSF}}{u_{max,h,LES}}=1.41$ and the mass fraction gradients $\frac{\nabla\varphi_{TSF}}{\nabla\varphi_{LES}}=2.01$ is not the same, but this is just an indicator that the relation of the velocity and the helium gradient is not linear.

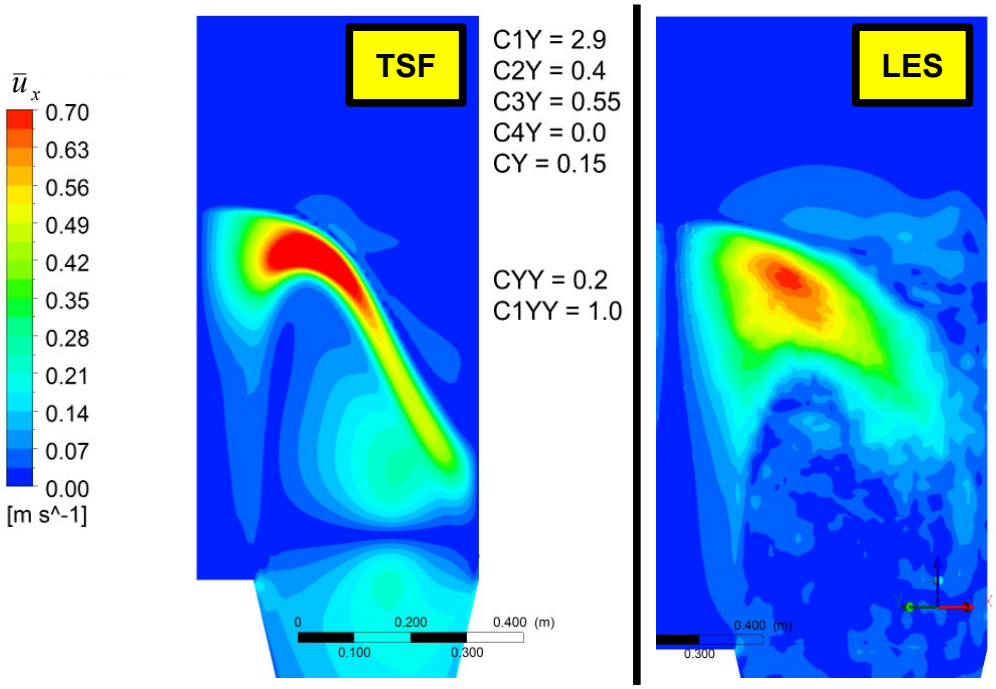

Fig. 48: Horizontal velocity of LES and TSF model

4.2.2 Modification of model coefficients

The turbulent scalar flux model has seven model coefficients (Table 5). The five coefficients C_{1Y}, C_{2Y}, C_{3Y}, C_{4Y} and C_Y are for the three spatial transport equations (2-29). The coefficients C_{YY} and C_{1YY} are for the variance (2-30).

C_{1Y}	C_{2Y}	C_{3Y}	C_{4Y}	C_Y	C_{YY}	C_{1YY}
2.9	0.4	0.55	0	0.15	0.2	1

Table 5: Original TSF model coefficients

The first coefficient to be modified is C_{3Y}, which is controlling the buoyancy production term (4-1). In the actual implementation $(1-C_{3Y})$, C_{3Y} is a weighting factor in combination with 1. A greater value for C_{3Y} results in a smaller factor and therefore in a lesser impact of the buoyancy production term on the turbulence mass flux G_y (2-34).

The buoyancy production term itself is negative in the TSF model. The last part of (2-34) contains the gravity vector $g=\begin{bmatrix}0\\0\\-9.81\end{bmatrix}\frac{m}{s^2}$. So the last part has only an impact in vertical direction. Here, the gravity is negative in a negative term which results in a positive effect on the transport equation.

The original value for $C_{3Y}=0.55$ which means 45% of the buoyancy turbulence production are considered. Two modifications of C_{3Y} are made. $C_{3Y}=0.0$ means a greater impact of 100%. $C_{3Y}=0.7$ leads towards a lesser impact of the buoyancy production.

The expected effects of a greater impact for $C_{3Y}=0.0$ is a greater turbulence mass flux, and a smaller mass flux is expected for $C_{3Y}=0.7$.

The second coefficient to be modified is C_{4Y}. This coefficient is controlling the last term in the pressure-scalar gradient correlation Π_Y (2-36). In the original coefficient set, $C_{4Y}=0.0$. Since there is no specific reason why this term could be neglected, the value of C_{4Y} is carefully increased and three different values are used, $C_{4Y}=0.1$, $C_{4Y}=0.3$ and $C_{4Y}=0.4$. An increased weighting of this term is expected to result in a larger turbulence mass flux.

4.2.3 Modification of the Buoyancy Production Term

The comparison of the helium outflow with the modified C_{3Y} is shown in Fig. 49. The green bar shows the original value of $C_{3Y}=0.55$. Only a slightly decrease helium outflow can be seen for $C_{3Y}=0.0$. This means that an increase of the influence of the buoyancy production term with $C_{3Y}=0.0$ results in a lesser helium outflow. But the difference of the outflow is rather small for $C_{3Y}=0.0$ and even negligible for $C_{3Y}=0.7$.

Fig. 50 shows the result of the turbulence mass fluxes according to the expectations discussed in chapter 4.2.2. More influence of the buoyancy production term with $C_{3Y}=0.0$ results in a larger turbulence mass flux. But the turbulence mass flux of the TSF model is still smaller than the turbulence mass flux of the LES ($\tilde{\Phi}_v=0.02\frac{m}{s}$ and $\tilde{\Phi}_h=0.1\frac{m}{s}$, see Table 3 or Table 4). The fact, that the largest turbulence mass flux leads to the lowest helium outflow in the investigation of C_{3Y} confirms that both values do not depend on each other.

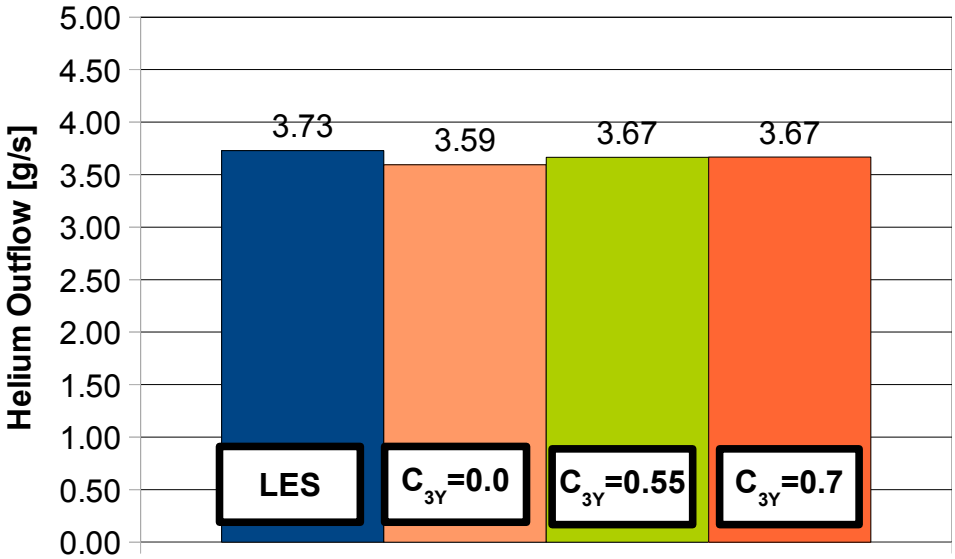

Fig. 49: Helium outflow comparison of LES and different values of C_{3Y}

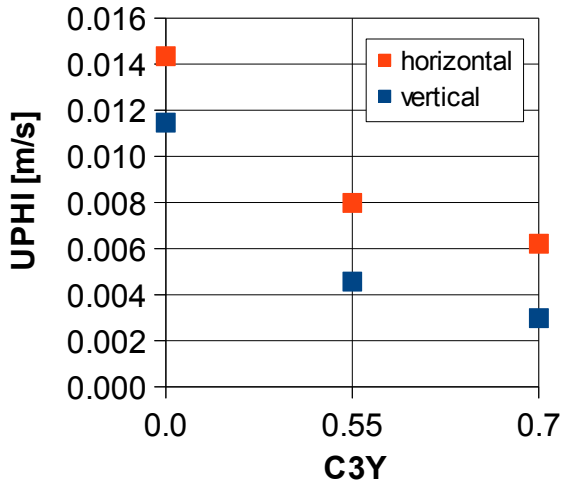

Fig. 50: Maximum turbulence mass flux

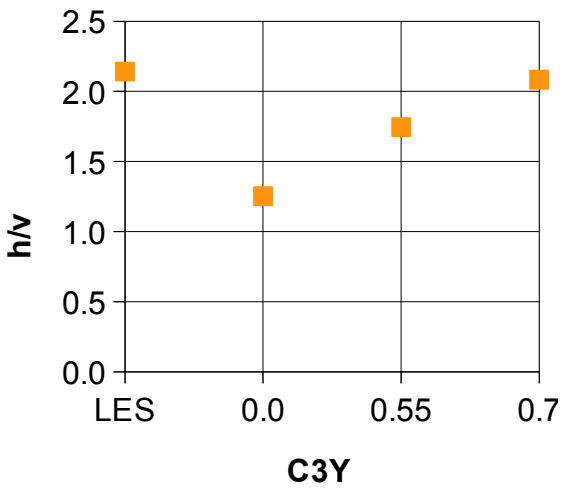

Fig. 51: h/v-ratio of the turbulence mass flux

The increase of turbulence mass flux with a smaller value for C_{3Y} happens with approximately the same value in horizontal and vertical direction. As an example, Fig. 50 shows that the increase of the turbulence mass flux from $C_{3Y}=0.7$ to $C_{3Y}=0.0$ is approximately the same in horizontal and in vertical direction $\Delta\tilde{\Phi}_h=\Delta\tilde{\Phi}_v=0.008\frac{m}{s}$. This causes a change in the h/v-ratio of the turbulence mass flux, which can be seen in Fig. 51. The h/v-ratio obtained with $C_{3Y}=0.7$ is approximately the same as the h/v-ratio of the LES. An increase of the turbulence mass flux with $C_{3Y}=0.55$ and $C_{3Y}=0.0$ results in a decreasing h/v-ratio.

The decrease of the h/v-ratio can be explained with the spatial distribution of the largest turbulence mass flux vectors (Fig. 52). In the LES, the mass flux vectors are mostly horizontal because the mixing happens at a higher point of the interaction region. The mixing in the TSF

simulations happens further downstream.

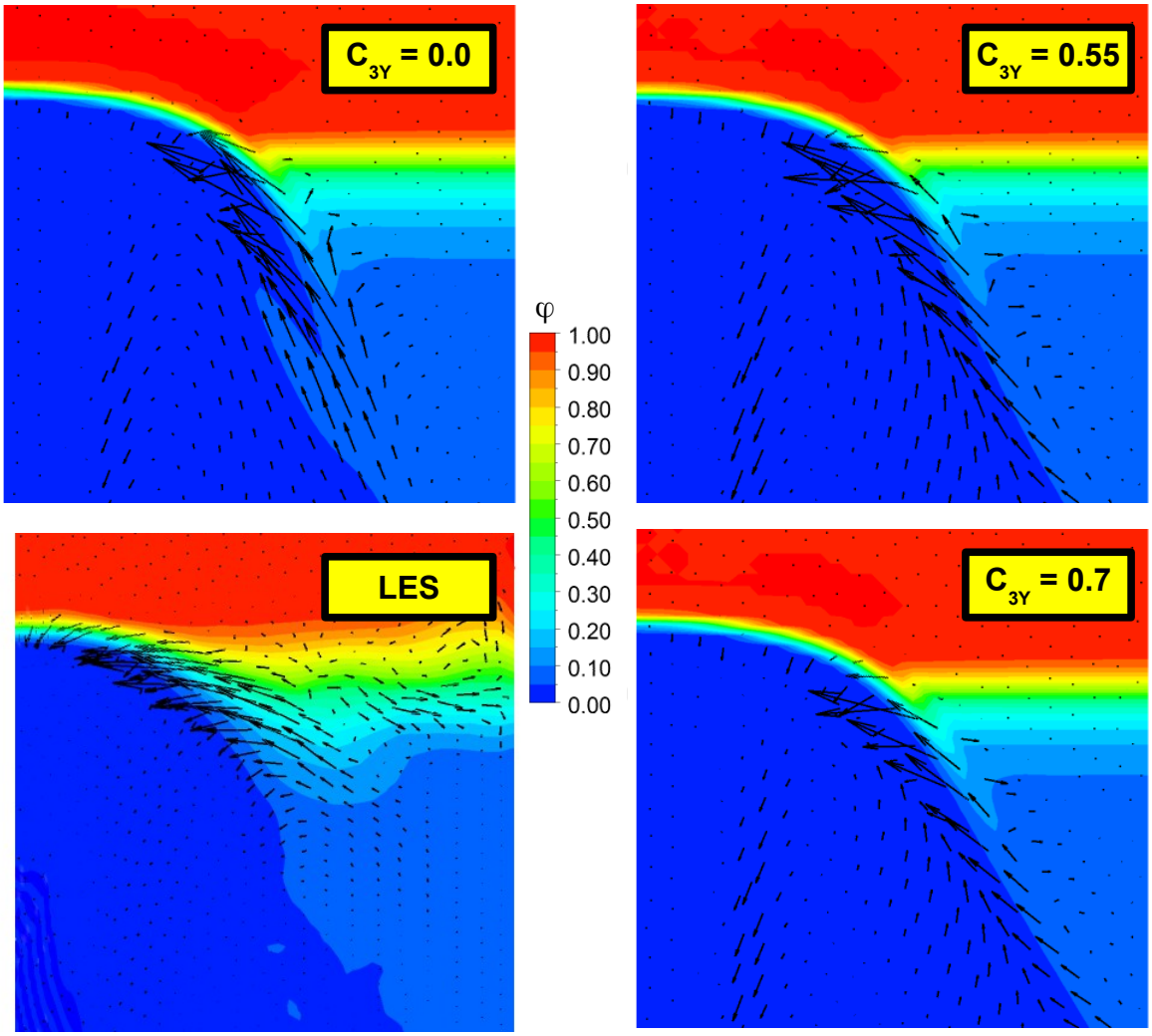

Fig. 52: Turbulence mass flux vectors and helium distribution of LES and different values of C_{3Y}

An explanation for this phenomenon is the larger horizontal helium mass fraction gradient in the TSF cases. The helium mass fraction distribution in Fig. 52 shows that the major part of the mixing is happening at a region where the helium mass fraction is lower than its maximum value. This region starts at a higher point in the LES. This is also the explanation for the larger horizontal helium mass fraction gradient obtained with the TSF model, since all these phenomena depend on each other. In the interaction region, the main flow is horizontal and pushing the density layer as discussed in chapter 4.1.3 (Fig. 46, page 66). In the TSF case, more helium is present in this horizontal flow region. So the jet is hitting a region of higher helium concentration and can therefore create a steeper gradient than in the LES.

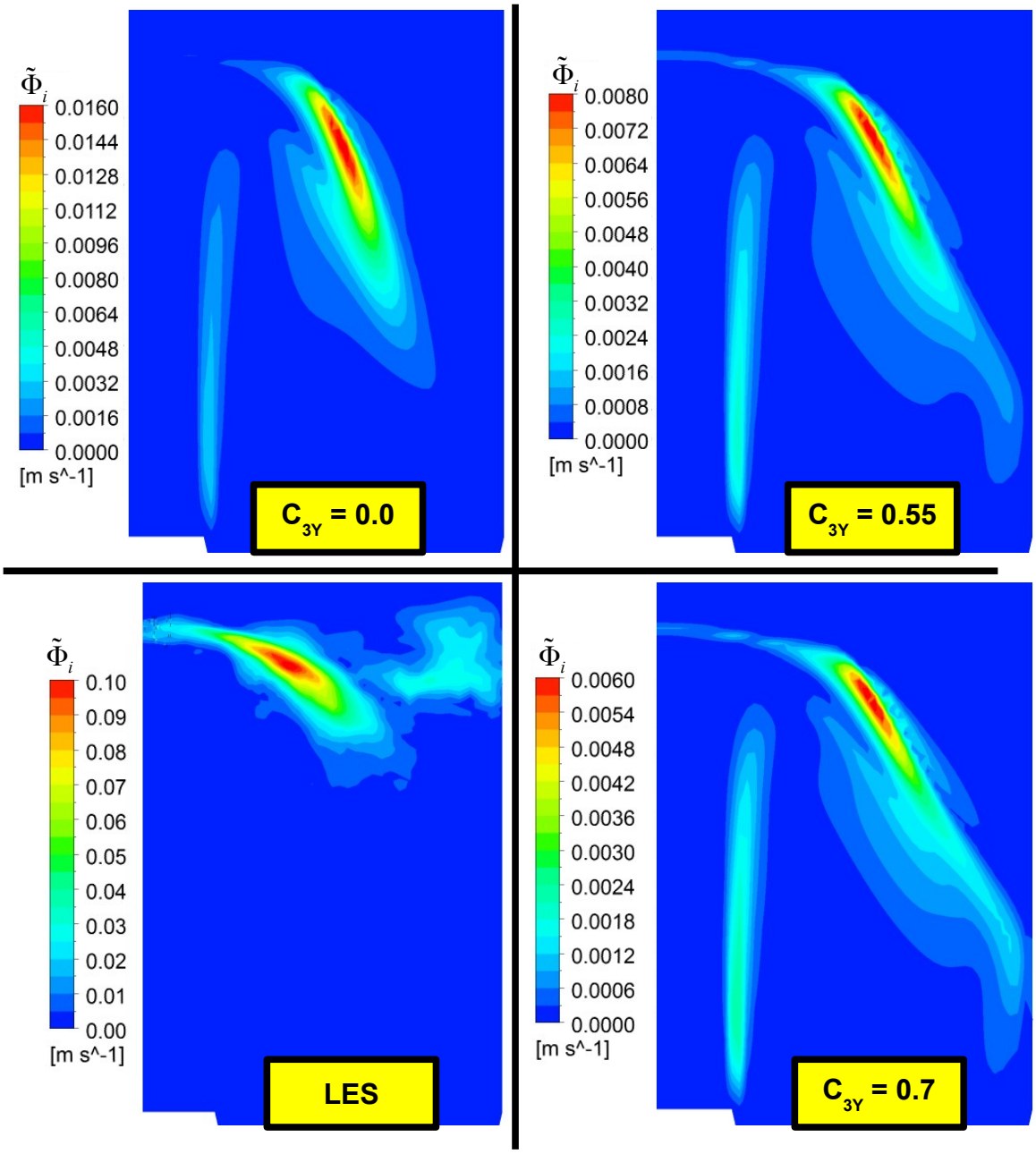

Fig. 53: Turbulence mass flux distribution of LES and different values of C_{3Y}

The steeper horizontal helium mass fraction gradient is damping the turbulence mass fluxes and forces the mixing to happen further downstream. The main flow in this region is downwards and to the wall. Since the main flow direction is influencing the direction of the turbulence mass flux, the vertical component is larger in the TSF case than in the LES. This effect is strongest with $C_{3Y}=0.0$ and weakest with $C_{3Y}=0.7$. The reason is that the direction of the down-flow is more towards the wall with $C_{3Y}=0.7$ which results in a larger horizontal component of the main flow and the turbulence mass flux. The down-flow with $C_{3Y}=0.0$ is more towards the outlet and is therefore enlarging the vertical components

more.

It is also worth mentioning, that the turbulence mass flux in the shear layer of the upward jet is absent in the LES (Fig. 53). The reason for the mass flux into the jet is the swirl in the lower region of the domain. When the swirl is stronger, more helium is transported towards the jet. This means that the strongest swirl occurs with $C_{3Y}=0.7$ (Fig. 54). The swirl becomes weaker with a lower value of C_{3Y} which means a greater influence of the buoyancy production.

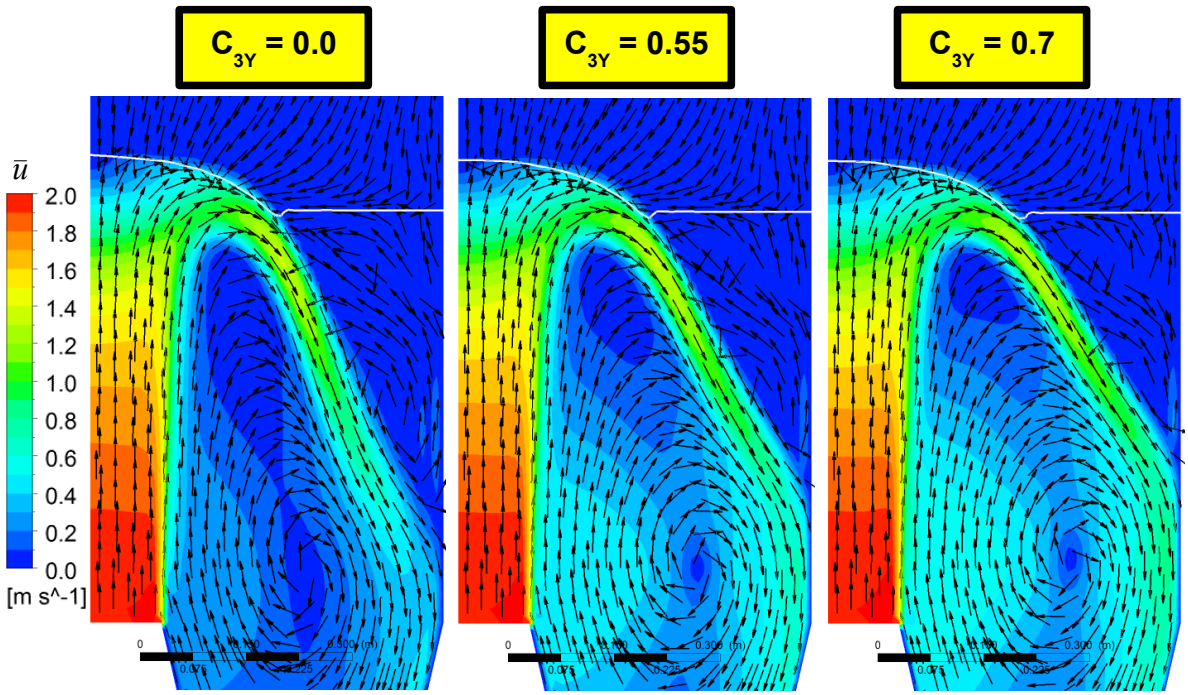

Fig. 54: Transient averaged velocity with uniform velocity vectors of different values of C_{3Y}

The modification of C_{3Y} showed that a greater consideration of the buoyancy production leads to a better agreement with the large eddy simulation. The swirl in the lower part of the domain becomes weaker. This has an impact on the helium mass fraction distribution in the lower part of the domain (Fig. 55). It turns out that even the weakened swirl still interferes with the helium outflow.

This explains why the helium outflow stays approximately the same with all three values for C_{3Y} even with a large increase of the turbulence mass flux. Fig. 55 shows, that the helium mass fraction distribution closer to the density layer obtained with $C_{3Y}=0.0$ shows a partially better agreement with the LES than the result of $C_{3Y}=0.7$. But in the lower part of the domain, closer to the outlet, an impact of the swirl can not be observed.

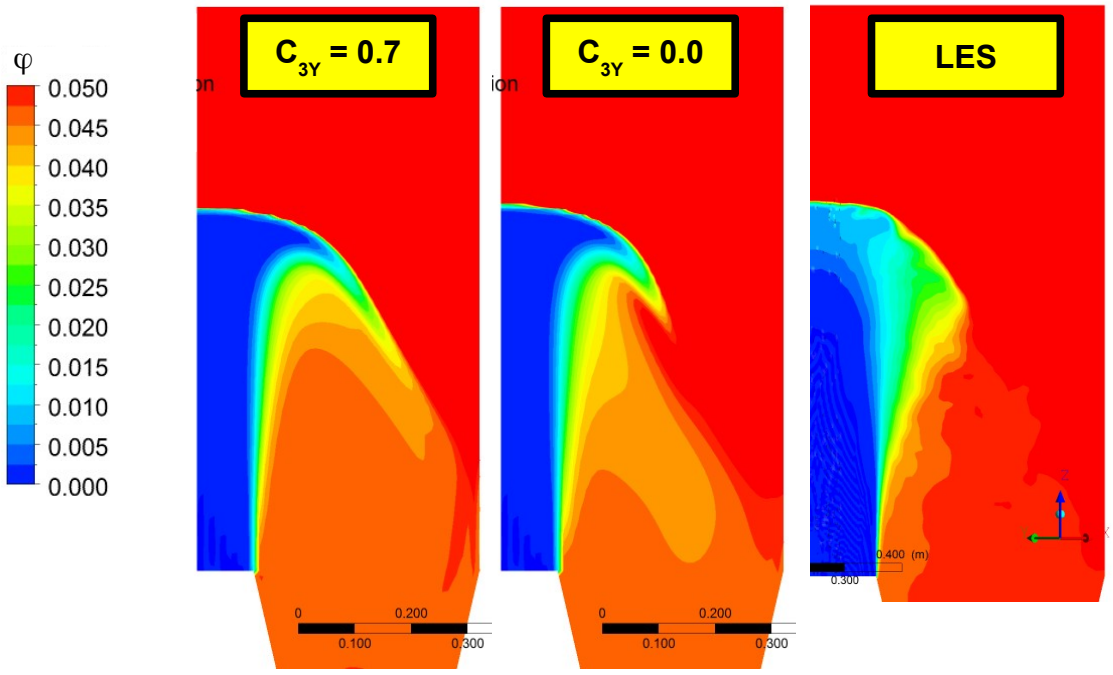

Fig. 55: Helium mass fraction 0-0.05 of LES and different values of C_{3Y}

4.2.4 Modification of the Pressure Scalar Correlation

The modification of C_{4Y} has a considerable impact on the helium outflow (Fig. 56). A greater value of C_{4Y} results in a greater helium outflow. The greatest used value for C_{4Y} is $C_{4Y}=0.4$. A greater value causes numerical problems and negatively effects the solver stability. Considering the results so far, it can not be assumed that a greater helium outflow equals a greater turbulence mass flux. The results of the investigation of the modification of C_{4Y} confirms that a greater helium outflow is no indicator for larger turbulence mass fluxes or vice versa.

However, the turbulence mass flux increases from $C_{4Y}=0.0$, which is the original value of C_{4Y}, to $C_{4Y}=0.1$ (Fig. 57), but the increase is approximately the same for the vertical and the horizontal component. An even larger increase of the turbulence mass flux can be obtained with $C_{4Y}=0.3$. Here, the horizontal component is increased more than the vertical component which is in better agreement with the LES.

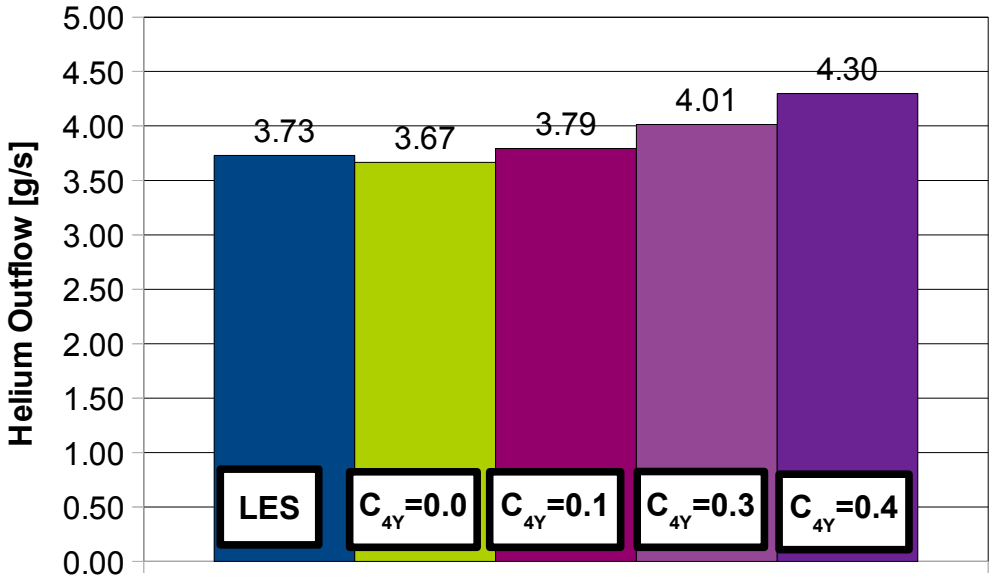

Fig. 56: Helium outflow of LES and different values of C_{4Y}

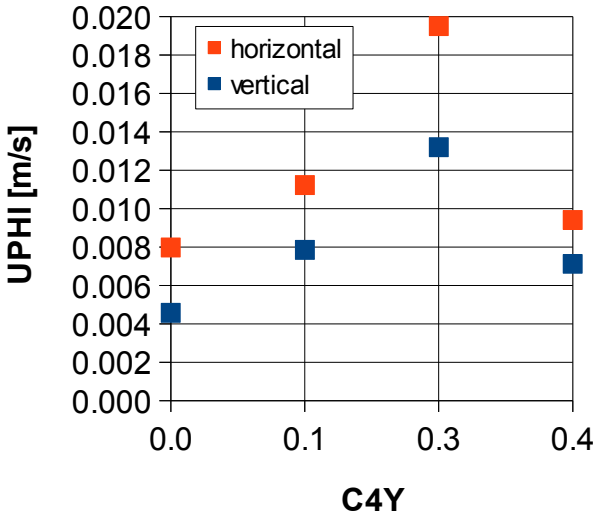

Fig. 57: Turbulence mass flux

Increasing C_{4Y} further results in a large decrease of the turbulence mass fluxes. The fluxes for $C_{4Y}=0.4$ are even smaller than for $C_{4Y}=0.1$. The h/v-ratio is also the smallest for $C_{4Y}=0.4$. This observation leads to the conclusion that an increase of C_{4Y} to a larger value than the optimal value of 0.3 yields non-physical phenomena and eventually causes problems for the solver. This explains the stability issues of the solver with $C_{4Y}>0.4$ for the steady case.

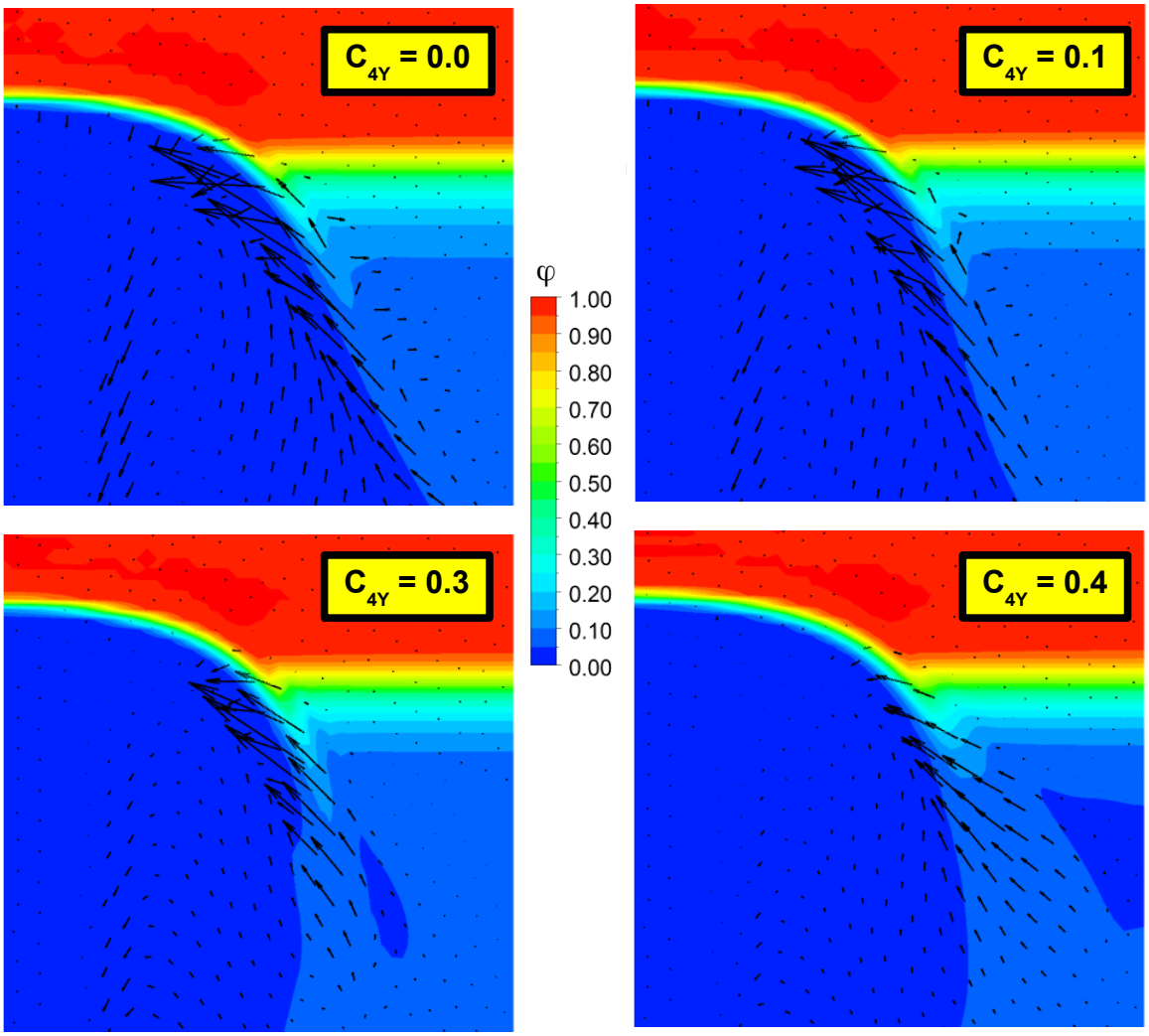

Fig. 58: Turbulence mass flux vectors and helium distribution of different values of C_{4Y}

So far, the results of the modification of C_{4Y} showed an increasing helium outflow for a larger value of the model coefficient. It also showed that the maximum turbulence mass fluxes can be obtained with $C_{4Y}=0.3$. The turbulence mass flux vectors in Fig. 58 show that the best agreement with the large eddy simulation can also be obtained with $C_{4Y}=0.3$. A comparison of $C_{4Y}=0.1$ and $C_{4Y}=0.3$ shows that the horizontal component is larger with $C_{4Y}=0.3$ and that the region where the turbulence mass fluxes are present is more concentrated towards the layer.

The direction of the turbulence mass flux in the interaction region shows the same tendency for $C_{4Y}=0.1$ and $C_{4Y}=0.3$. It has a larger vertical component than the LES, because it is further downstream, but has a comparable behaviour upwards and towards the jet. Both results still show the smaller turbulence mass fluxes in the shear layer of the upward jet. However, the focus of this investigation is the interaction region with the stable stratification.

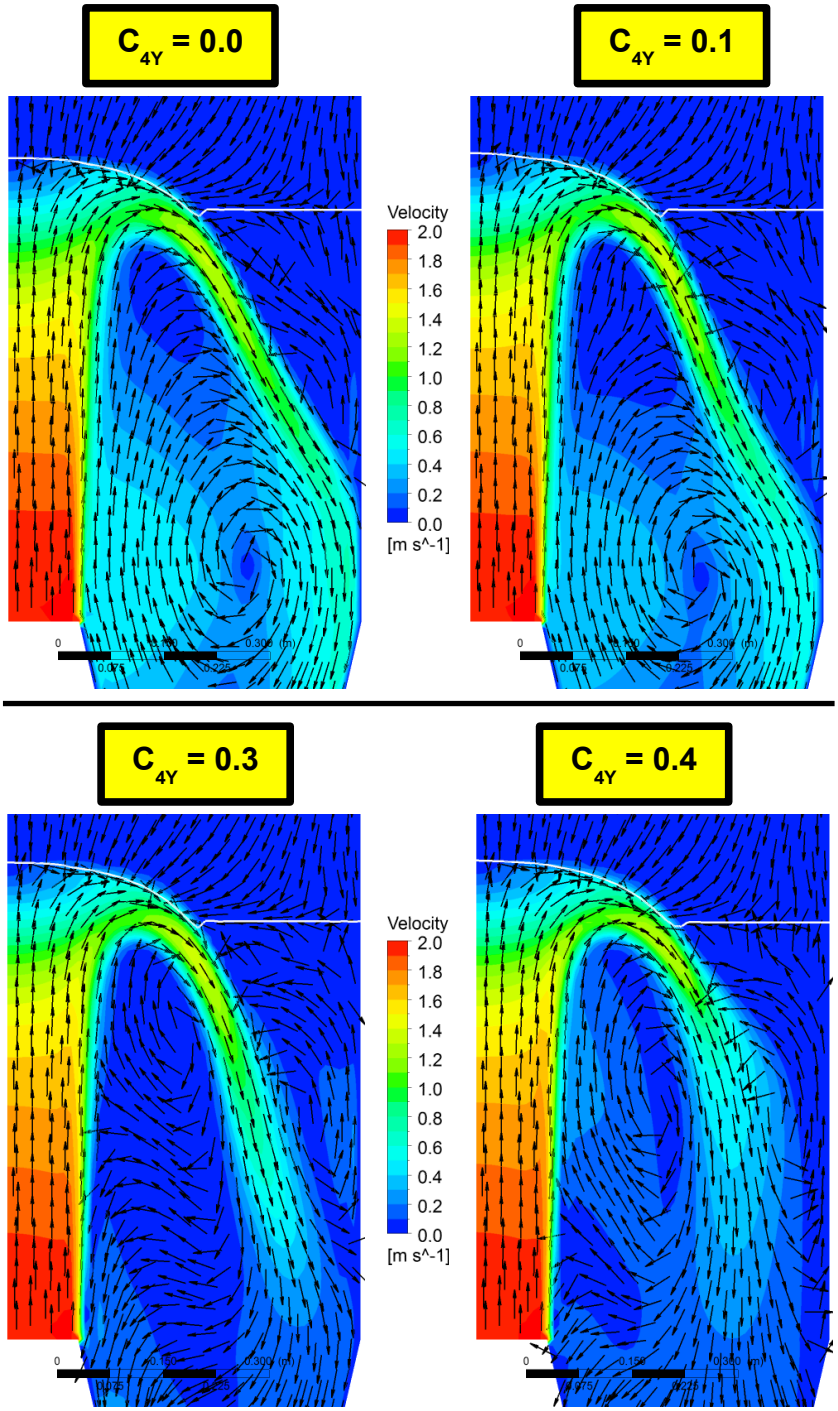

Fig. 59: Transient averaged velocity with uniform velocity vectors of different values of C_{4Y}

The turbulence mass flux vectors for $C_{4Y}=0.4$ are different than for the other investigated values of C_{4Y}. The mass fluxes in the interaction area are less focused in a broader region and have different directions.

The velocity vectors in Fig. 59 show a great improvement from $C_{4Y}=0.1$ to $C_{4Y}=0.3$. The flow obtained with $C_{4Y}=0.1$ still has a distinct swirl in the lower part of the domain.

In the result for $C_{4Y}=0.3$, this swirl can longer be seen. The flow field obtained with $C_{4Y}=0.3$ has the best agreement with the large eddy simulation for all investigated values of C_{3Y} and C_{4Y}.

The flow field for $C_{4Y}=0.4$ has also no swirl in the lower part of the domain. The down-flow branch of the main flow has a different shape compared to the other results. It is forming an arc bend towards the upward jet and not the triangle with the density layer and the wall which is the common shape for the other RANS simulations with TSF model as well as the large eddy simulation. So the down-flow for $C_{4Y}=0.4$ is between the RANS simulation with eddy diffusivity model (see chapter 3.3) and the other TSF model simulations.

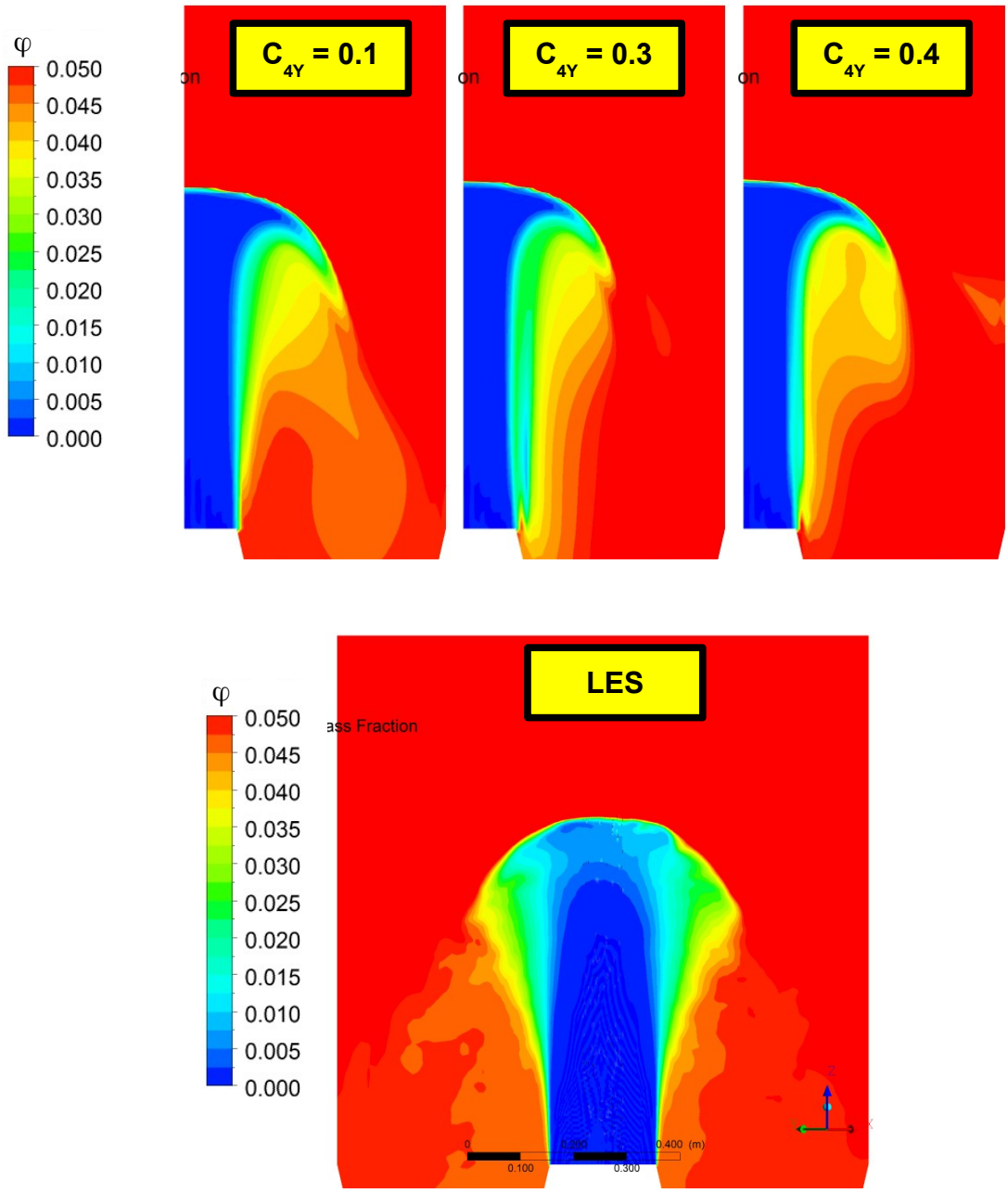

Fig. 60: Helium mass fraction 0-0.05 of LES and different values of C_{4Y}

The investigation of the buoyancy production term (chapter 4.2.3) shows, that a modification of the model coefficient C_{3Y} not only affects the turbulence mass fluxes but also the flow field. The modification towards a greater turbulence mass flux resulted in a weaker but still present swirl. A different main flow in the lower part of the domain leads to a different helium mass fraction distribution in this region.

The investigation of the pressure scalar correlation shows, that a modification of C_{4Y} towards a greater turbulence mass flux with $C_{4Y}=0.3$ yields a better agreement with the LES for the turbulence mass flux and the velocity distribution. The helium mass fraction distribution in the lower part has also the best agreement with the LES for $C_{4Y}=0.3$ (Fig. 60).

The helium distribution for $C_{4Y}=0.1$ shows the expected effect of the swirl which is hindering the helium from leaving the domain. The result for $C_{4Y}=0.4$ shows a worse agreement with the LES than $C_{4Y}=0.3$. An interesting aspect of the $C_{4Y}=0.4$ helium mass fraction distribution is that the helium concentration near the outlet is higher than with $C_{4Y}=0.3$. This means that a larger amount of helium is brought to the outlet, which can be explained with the different shape of the down-flow.

4.2.5 Steady Case with the Final Model Coefficients

So far, the modification of a single model coefficient while leaving the others at their original value has been discussed. The modification of C_{3Y} to control the buoyancy production term showed the best result for $C_{3Y}=0.0$ which means that the full buoyancy production is considered for the turbulence mass fluxes. The modification of C_{4Y} showed that the best agreement with the large eddy simulation can be obtained with $C_{4Y}=0.3$. The last step of the investigation of the steady case is a combination of both modified model coefficients. Table 6 gives an overview over the final set of model coefficients.

C_{1Y}	C_{2Y}	C_{3Y}	C_{4Y}	C_Y	C_{YY}	C_{1YY}
2.9	0.4	0	0.3	0.15	0.2	1

Table 6: final TSF model coefficients

The helium outflow obtained with the final model coefficients $C_{3Y}=0.0$ and $C_{4Y}=0.3$ is almost the same as the outflow of the large eddy simulation (Fig. 61). While the helium outflow is not related to the turbulence mass flux, this result is an indicator that the result obtained with the final model coefficients is in good agreement with the LES.

The turbulence mass flux for the combination of $C_{3Y}=0.0$ and $C_{4Y}=0.3$ is larger than with the modification of only one of the coefficients (Fig. 62). This is the desired result because the combination of the values for C_{3Y} and C_{4Y} with the largest turbulence mass flux in each case is expected to yield an even larger mass flux. The horizontal component of the turbulence mass flux of the large eddy simulation is still larger than those with the final model coefficients but the vertical component is similar ($\tilde{\Phi}_v=0.02\frac{m}{s}$ and $\tilde{\Phi}_h=0.1\frac{m}{s}$, see Table 3 or Table 4).

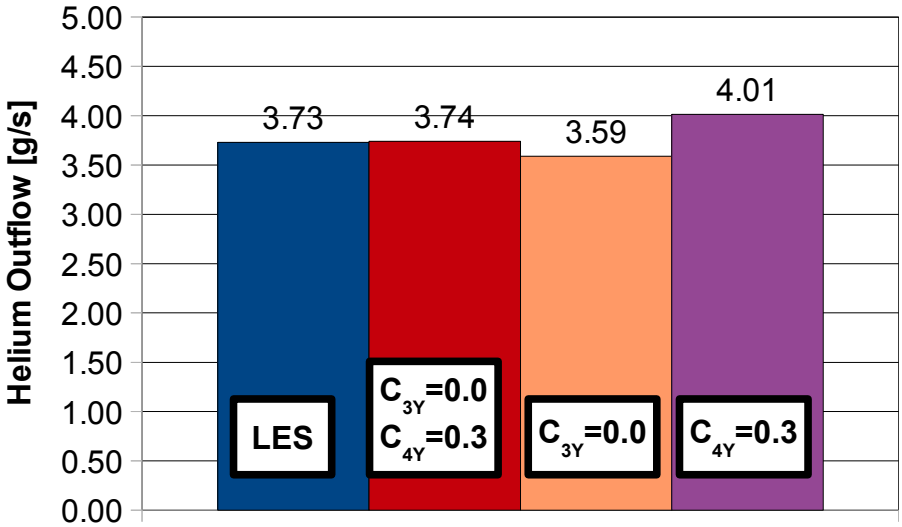

Fig. 61: Helium outflow of LES, and the final values of C_{3Y} and C_{4Y}

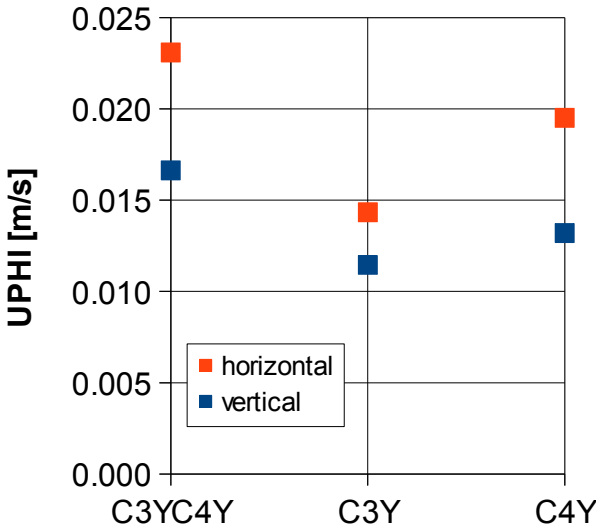

Fig. 62: Turbulence mass flux

The comparison of the velocity vectors of the final model coefficients and the LES (Fig. 63) shows a good agreement. The swirl in the lower part of the domain that is present in the results of some simulations with different values of C_{3Y} and C_{4Y} can not be found in the result obtained with the final model coefficients.

The downward branch of the main flow of the LES is less distinct due to the density layer movement. The down-flow of the final TSF simulation is more narrow and slightly more downwards, where the down-flow of the LES is slightly more towards the wall. The movement of the density layer is also the reason for the broader density layer between the interaction region and the wall in the large eddy simulation.

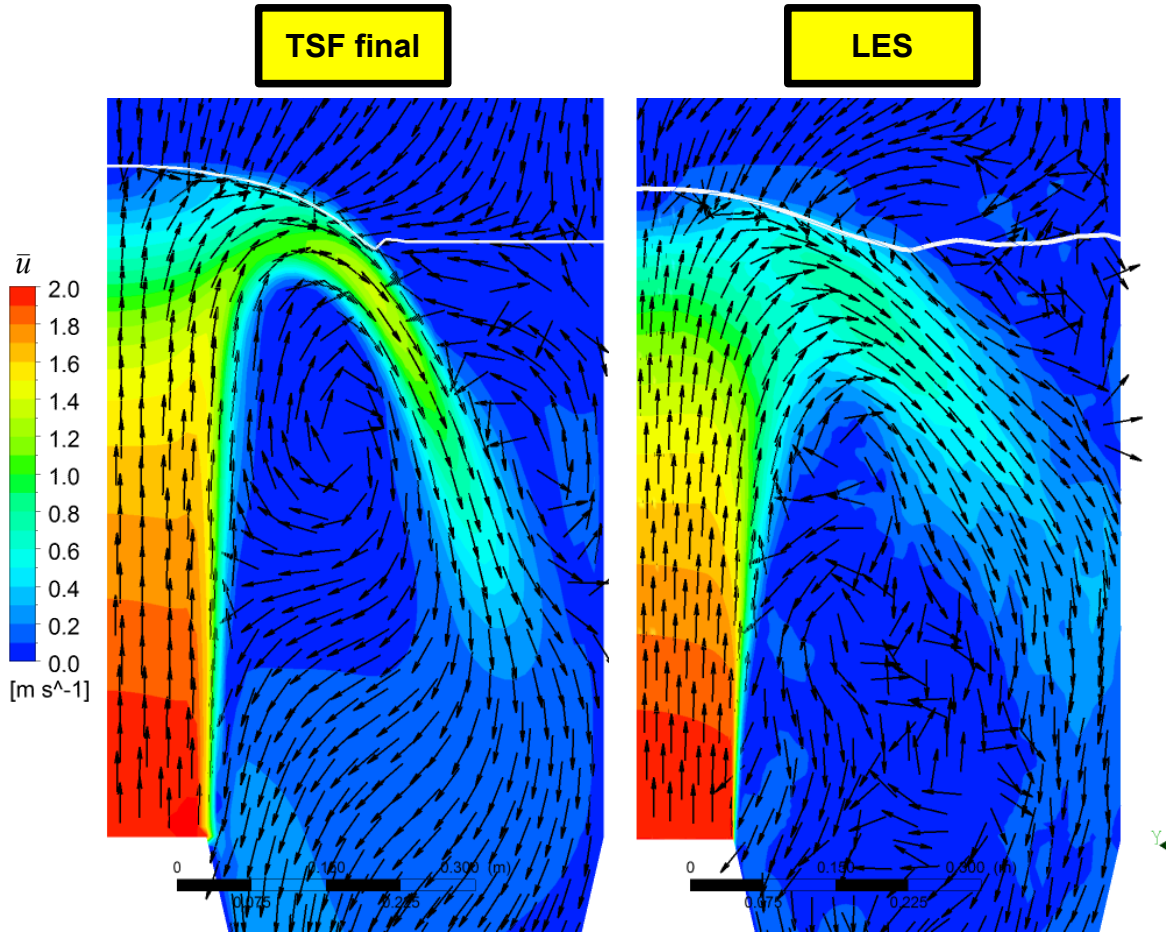

Fig. 63: Transient averaged velocity with uniform velocity vectors

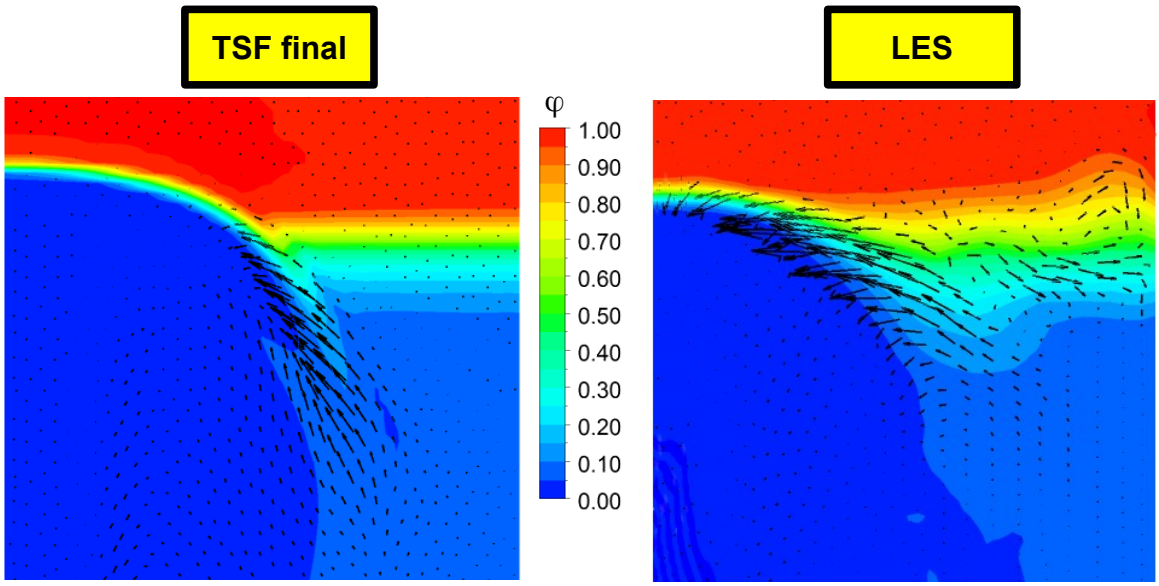

Fig. 64: Turbulence mass flux vectors and helium distribution

The small discrepancy in layer thickness and down-flow direction is responsible for the different position and direction of the maximum turbulence mass flux (Fig. 64). This phenomenon is already discussed in chapter 4.2.3 (Fig. 53, page 73).

The helium mass fraction distribution below the density layer with the final TSF model shows also a good agreement with the large eddy simulation (Fig. 65). It looks like the helium mass fraction for $C_{4Y}=0.3$ (Fig. 60, page 79) is slightly improved by the additional use of $C_{3Y}=0.0$.

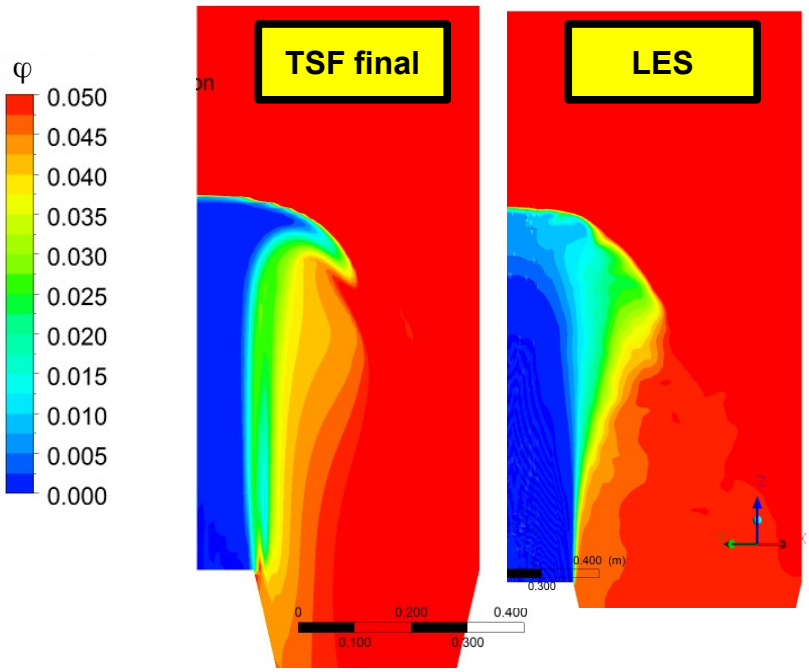

Fig. 65: Helium fraction, close-up view

4.2.6 Summary of the Steady Case with the TSF model

The first simulation of the steady case with the turbulence scalar flux model was carried out with the original model coefficients. The result of this simulation showed a much better agreement with the large eddy simulation than the RANS simulations with the eddy diffusivity model.

To improve the result of the TSF model further, two model coefficients have been modified separately. The dimension analysis (see chapter 2.1) showed a large Archimedes number which means that the buoyancy forces are of great significance (Table 2, page 24). Therefore, the coefficient C_{3Y}, which is governing the buoyancy production term, has been modified to increase and decrease the influence of the buoyancy production on the turbulence mass fluxes. Due to the implementation of the TSF model, a larger value of C_{3Y} means a lesser consideration of the buoyancy production and vice versa. The investigated values are

$C_{3Y}=0.0$, $C_{3Y}=0.7$ and the original value $C_{3Y}=0.55$.

The other coefficient that has been modified is C_{4Y}. It governs a term in the pressure-scalar gradient correlation. This correlation is redistributing the turbulence mass flux and can be used to add anisotropy. Its original value is $C_{4Y}=0.0$ which means that the term is neglected. The investigated values in addition to the original value of $C_{4Y}=0.0$ are $C_{4Y}=0.1$, $C_{4Y}=0.3$ and $C_{4Y}=0.4$. A modification of the other two coefficients of the pressure scalar correlation, C_{1Y} and C_{2Y} , did not improve the result.

Finally the values of each model coefficient with which the best results could be obtained, $C_{3Y}=0.0$ and $C_{4Y}=0.3$, have been used together.

At first, the helium mass flow out of the domain was considered to be a simple parameter to judge the mixing in addition to the turbulence mass flux. The reason for this assumption is that the helium outflow is expected to be larger with a better mixing . It turned out that this assumption is not correct and that the helium outflow is affected by the flow situation in the lower part of the domain. Many results of the RANS simulations show a large swirl in the lower part of the domain which is an obstacle for the helium outflow. The modification of C_{4Y} showed that the helium outflow increases with a decreasing strength of the swirl. The modification of C_{3Y} showed a stronger swirl for greater values of the model coefficient, but no notable impact on the helium outflow could be observed. The best agreement with the helium outflow of the large eddy simulation can be obtained with the final values $C_{3Y}=0.0$ and $C_{4Y}=0.3$.

As noted above, the increase or decrease of the turbulence mass flux is not correlated with the helium outflow. The modification of C_{3Y} showed that the turbulence mass flux is higher with a greater consideration of the buoyancy production. The largest turbulence mass fluxes can be obtained with $C_{3Y}=0.0$. The modification of C_{4Y} showed an increase of the turbulence mass flux with an increasing value for C_{4Y} up to a maximum for $C_{4Y}=0.3$. Increasing C_{4Y} more results first in a sharp decrease of the turbulence mass flux and then to stability issues with the solver. The largest turbulence mass flux and therefore the best agreement with the large eddy simulation can be obtained with the final values $C_{3Y}=0.0$ and $C_{4Y}=0.3$.

4.3 Experimental Case

In this chapter the results of the simulation of the experimental case with the turbulence scalar flux model are discussed. Since the dimension analysis showed that the steady case is a good representation of the experimental case concerning the dimensions, the major difference between the two cases is the time.

The first part of the chapter presents a comparison of the experimental data, the results of a simulation with the eddy diffusivity model and the TSF model. Then the result of the steady case concerning the model coefficients are applied. The coefficients which yield the best agreement with the large eddy simulation for each case will be used, $C_{3Y}=0.0$ and $C_{4Y}=0.3$, as well as the combination of both.

4.3.1 TSF model results and comparison to experiment and EDM

The first step of the investigation of the experimental case with the TSF model is a simulation with the original model coefficients (see Table 5, page 69) and a comparison with the eddy diffusivity model and the experimental data. The compared values are the helium concentrations at certain monitor points due to experimental data availability. Only very limited velocity and no turbulence information is available for the experimental case.

The used monitor points are at different heights in the experimental facility to cover the advancement of the density layer towards the ceiling. For an overview of all measurement positions of the experimental case see Fig. 18, page 39. All monitor points used for the comparison are at x = 1.078 m, which is located horizontally between the interaction region of the jet with the density layer and the wall of the vessel. The naming convention for the monitor points of the original experimental data is taken over. The relevant monitor point sorted by height are shown in Table 7.

name	**203**	**209**	**214**	**210**	**202**	**215**
x [m]	1.078	1.078	1.078	1.078	1.078	1.078
z [m]	**6.27**	**6.60**	**6.93**	**7.20**	**7.49**	**7.99**

Table 7: position of the monitor points used for comparison

The charts in Fig. 66 show the helium concentration at a given monitor point versus time. Initially all monitor points are inside the light gas cloud with helium concentrations larger than 30 %. The measured time starts with the generation of the free jet by the fan. After the jet reaches the density layer, the layer becomes more narrow. This behaviour is explained in the discussion of the steady case. If two cases have a similar mixing speed, the layer thickness can be seen in the charts in Fig. 66. A steeper time gradient of helium at a monitor point means a more narrow density layer. But this is only true if the mixing time is similar, otherwise the time gradient of helium is also affected by the advancement speed of the layer towards the ceiling.

The eddy diffusivity model shows the expected large discrepancy to the experimental data. It can be seen that the longer the calculated transient is, the larger the discrepancy becomes. The reason for this behaviour is the accumulation of the under-prediction of the mixing of the eddy diffusivity model over time.

Using the turbulence scalar flux model yields a significant improvement of the mixing. Here, the positive effect of the TSF model becomes more clear with a longer calculated transient. The curves of TSF and eddy diffusivity model at monitor point 203 are quite similar. But 0.33 m higher at monitor point 209 the curve of the TSF model is closer to the experimental data. This trend continues with the progress of the layer towards the ceiling. A comparison of monitor points 210, 202 and 215 shows that the gap between the curve of the TSF model and the measured data is getting smaller while the gap between the curves of TSF and eddy diffusivity model is getting larger. The reason for this behaviour is the smaller error of the

TSF model to predict the mixing. The TSF model is still under-predicting the mixing and this error is also accumulated. The accumulation of the under-prediction described above for the eddy diffusivity model can be seen as well for the TSF model in Fig. 66. But it is less than the under-prediction of the eddy diffusivity model.

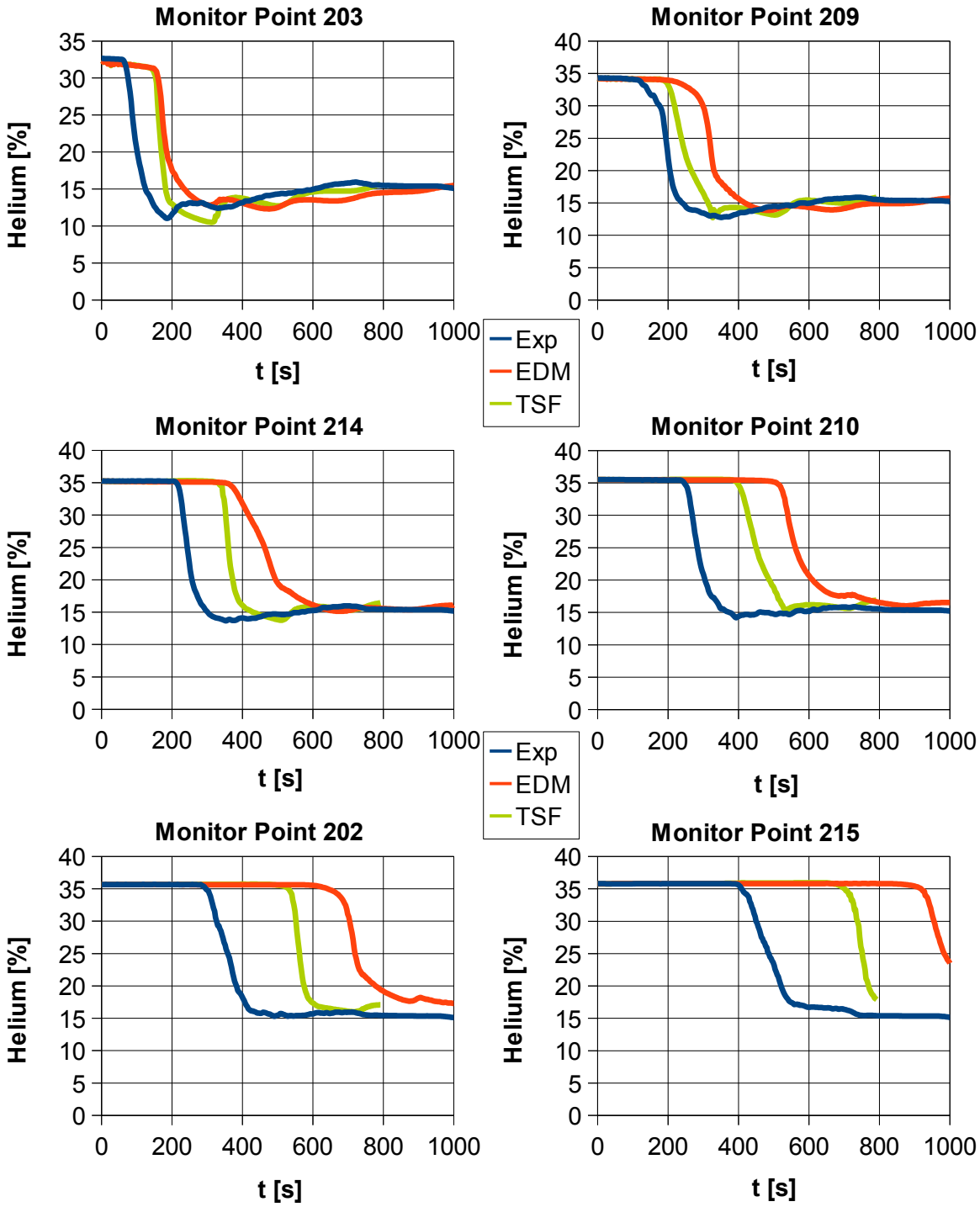

Fig. 66: Helium Concentration at different Monitor Points; Experiment ↔ TSF ↔ EDM

Fig. 67 shows the advancement of the density layer over the monitor points 203 and 209 calculated with the turbulence scalar flux model. The sequence in Fig. 67 starts at 0 seconds and shows the initial helium distribution. The region of the density layer is rather broad. After 10 seconds, the jet reaches up to the region of 28 % helium. The density layer in the region of the jet is drastically narrowed. The thickness of the layer closer to the wall is not yet affected by the jet.

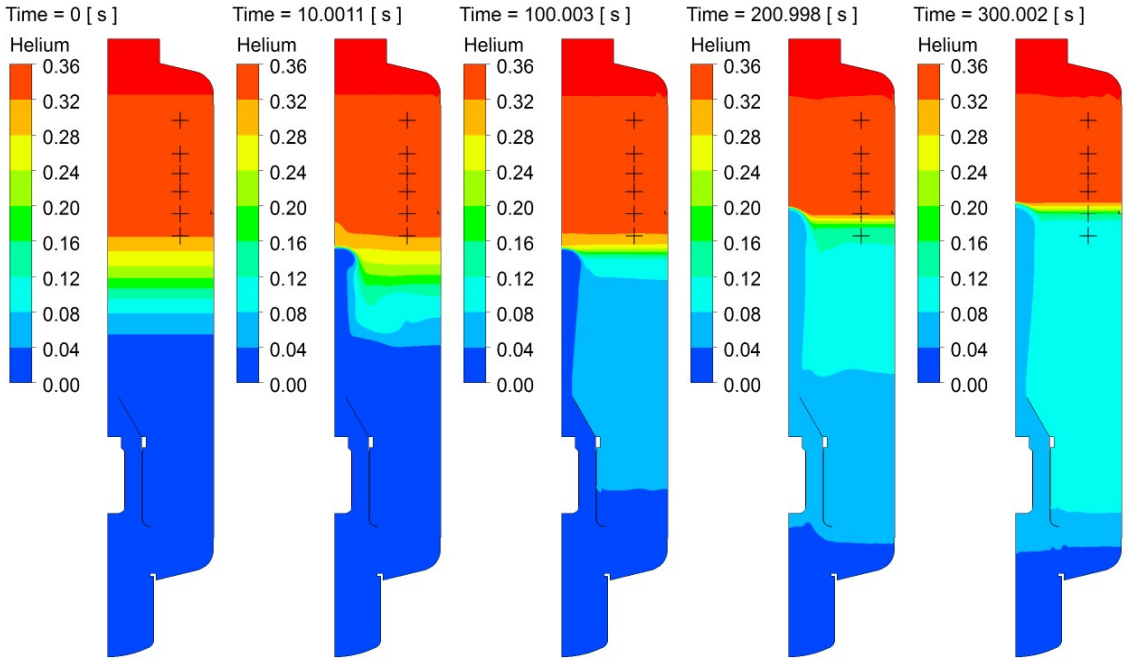

Fig. 67: Helium concentration with TSF model at different times

The next contour plot in Fig. 67 shows the helium distribution after 100 seconds. The jet has still the same length that it had after 10 seconds and the density layer did not advance further towards the ceiling. What happened in the 90 seconds is a change of the density layer thickness between the jet and the wall. It has now an approximately uniform thickness along its whole length. A small amount of helium is transported downwards and is already reaching the inner cylinder. But the fan is not yet entraining helium.

After 200 seconds the density layer moved upwards and is now above monitor point 203. This can also be seen in Fig. 66. The thickness of the density layer is further decreased and more helium is brought down to the lower part of the vessel. The fan is now entraining a mixture of helium and air, so the jet contains a small helium concentration.

The helium in the jet at 200 seconds leads to a less steep helium mass fraction gradient in the interaction region and causes a larger turbulent mass flux. The last contour plot in Fig. 67 shows a further continuation of the effects of the mixing on the density layer thickness and the transport of helium to the lower part of the vessel.

The turbulence mass flux distribution is shown in Fig. 68. At 10 seconds the largest turbulence mass flux is at the side of the jet downstream of the redirection region. This can be

explained with the broad density layer at that time. Since the layer is broad, the jet is reaching deep inside the light gas cloud. In this case the helium mass fraction gradient further away from the redirection region is better for the mixing.

After 100 seconds, the largest turbulence mass flux is close to the redirection region. The jet still contains only air and the helium mass fraction gradient is steep. This leads to a decreased turbulence mass flux than at 10 seconds.

After 200 seconds the jet contains helium. This results in a less steep helium mass fraction gradient between the jet and the density layer. The effect of the less steep gradient leads to an increased turbulence mass flux.

The turbulence mass flux decreases again a little bit after 300 seconds. This can be explained with the helium distribution shown in Fig. 67. The helium concentration inside the jet is not considerably increased, but the density layer is less broad compared to the layer at 200 seconds. This leads to a steeper helium mass fraction gradient and therefore to a decreased turbulence mass flux.

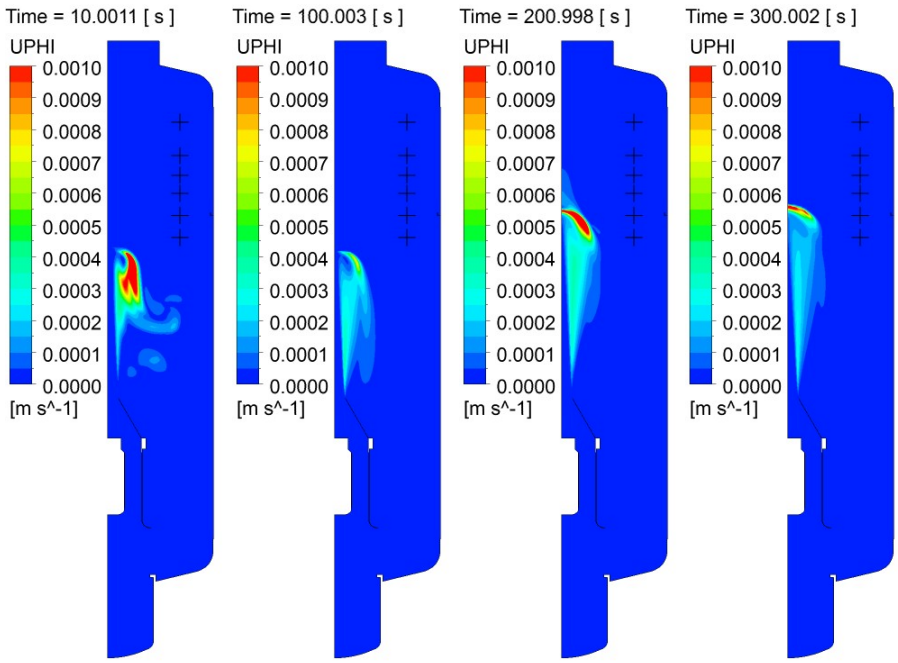

Fig. 68: Turbulence Mass Flux with TSF model at different times

4.3.2 Modification of Model Coefficients

So far, the physical insight of the mixing and the turbulence mass flux obtained with the steady case could be confirmed with the simulation of the experimental case with the turbulence scalar flux model. To improve the mixing further, the results of the model coefficient modification are used on the simulation of the experimental case.

Modification of C_{3Y}

The first modified coefficient to be used is C_{3Y} which controls the buoyancy production term. The investigation of the steady case showed that the best results can be obtained with $C_{3Y}=0.0$. Using this value in the steady case leads to an increase of the turbulence scalar fluxes and a better agreement of the flow field of the large eddy simulation.

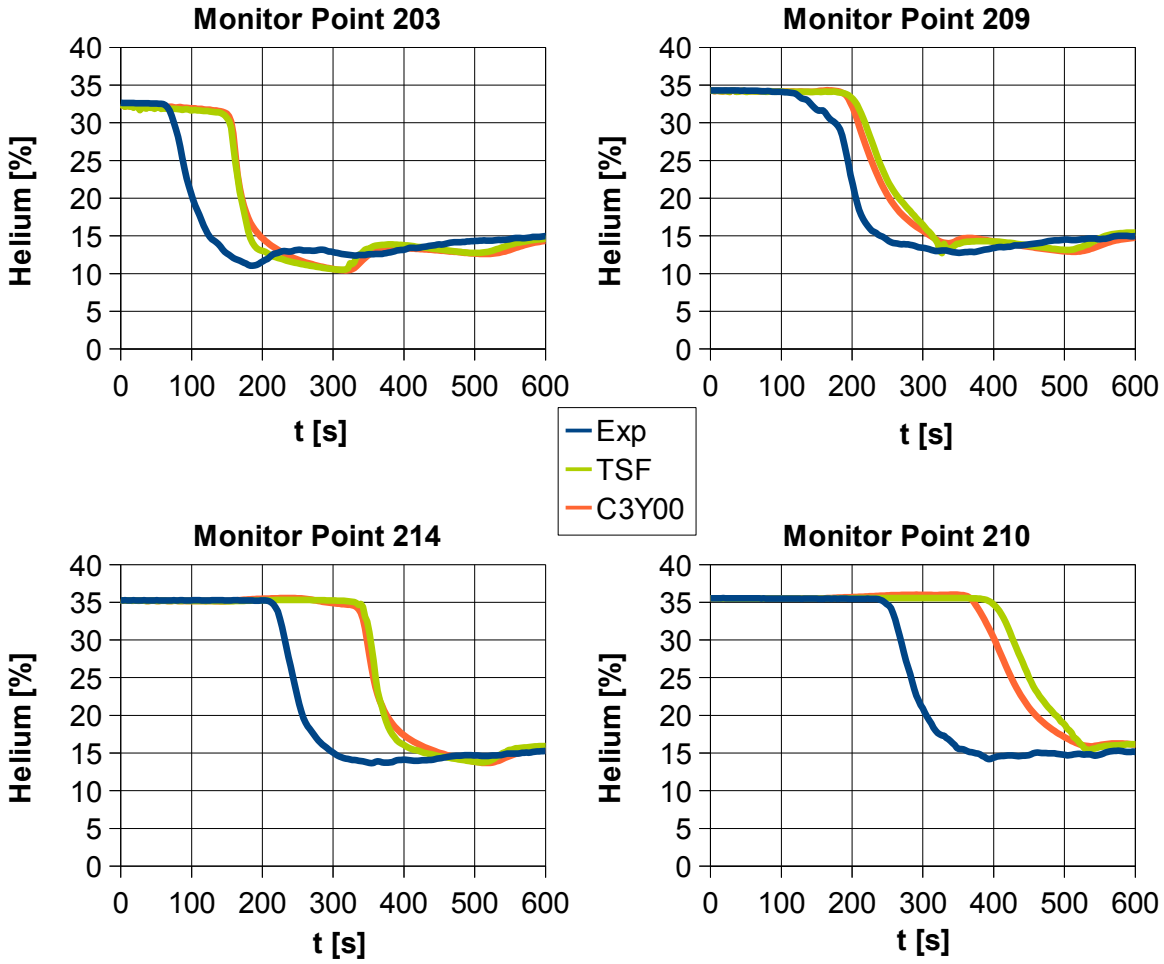

Fig. 69: Helium Concentration at different Monitor Points; Experiment ↔ TSF ↔ C_{3Y} = 0.0

The result of the modified C_{3Y} can be seen in Fig. 69. At the first three monitor points no considerable improvement can be observed. The mixing at monitor point 209 is slightly faster but at the next monitor point it is again similar.

The comparison of the TSF model with the original model coefficients and the eddy diffusivity model showed that the effect of the better mixing capabilities of a model becomes larger with a longer calculated transient. This is true as well for the result of the modified buoyancy production term. The mixing curve at monitor point 210 shows that a considerable

improvement of the mixing time can be obtained with $C_{3Y}=0.0$ compared to the original value of $C_{3Y}=0.55$.

The distribution of the turbulence mass flux at 100 s, 200 s, 300 s and 400 s can be seen in Fig. 70. An increase of the mass flux compared to the original TSF model coefficients (Fig. 68, page 88) can be observed, especially at 200 seconds.

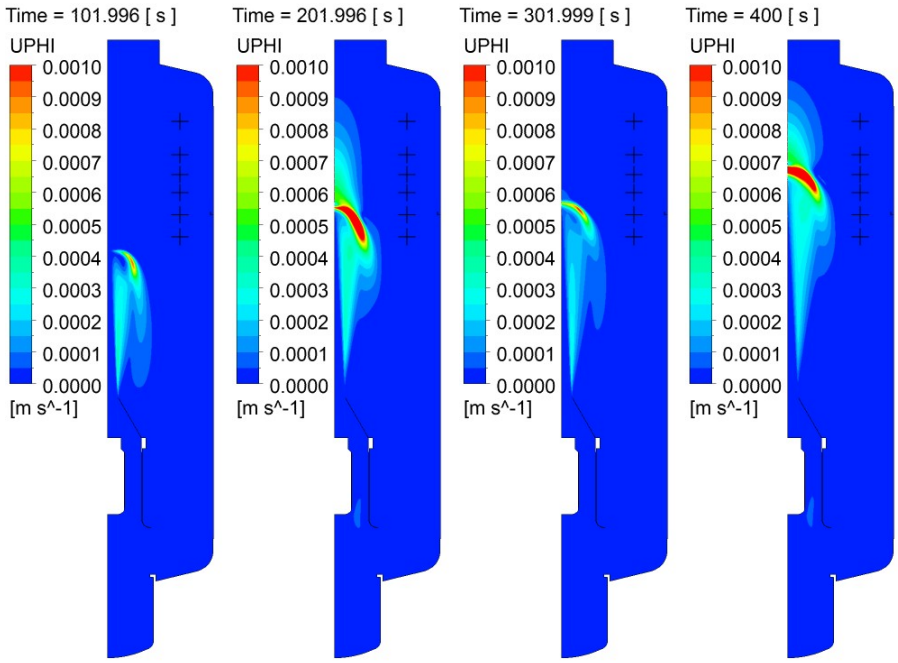

Fig. 70: Turbulence Mass Flux of the experimental case with modified buoyancy production term

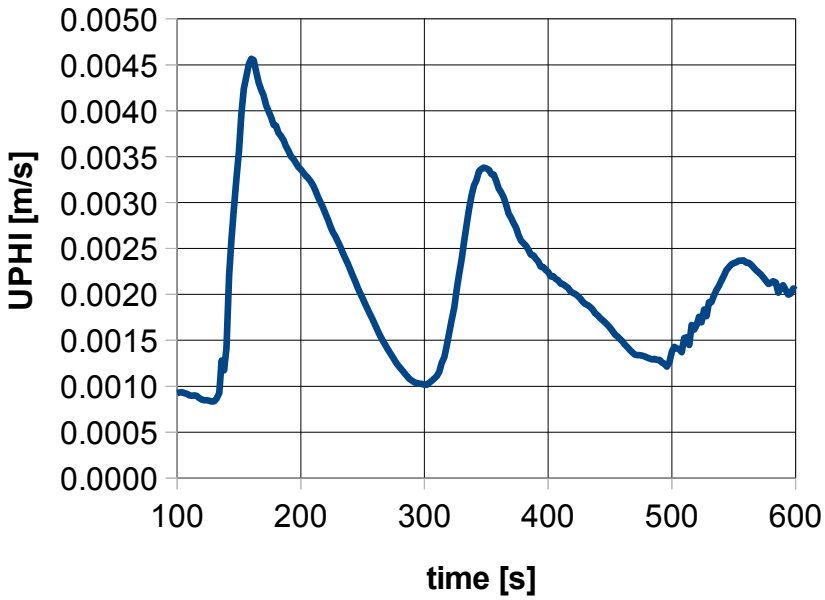

Fig. 71: Maximum turbulence mass flux with modified buoyancy production term

The four contour plots in Fig. 70 show a pattern of change of the turbulence mass flux. The shape and strength of the mass flux at 100 s and 300 s is similar. The same is true for at 200 s and 400 s. The strength of the turbulence mass flux is increasing and decreasing in a periodic fashion with decreasing amplitude. Fig. 71 shows the maximum value of the turbulence mass flux over time. It can be seen that the maximum turbulence mass fluxes are at a minimum at 120 s and 300 s. The maximum turbulence mass flux at 100 s is not much larger than at 300 s which leads to the similar contour plots at 100 s and 300 s. At 200 s and 400 s the value of the maximum turbulence mass flux is at a similar position between the maximum and minimum of the curve.

An explanation for the periodic increase and decrease of the maximum turbulence mass flux and the decreasing amplitude shown in Fig. 70 and Fig. 71 can be found in the amount of helium in the free jet and the shape and broadness of the density layer. The helium mass fraction distribution for $C_{3Y}=0.0$ shown in Fig. 72 show basically the same behaviour as for the original value $C_{3Y}=0.55$ (see Fig. 67, page 87).

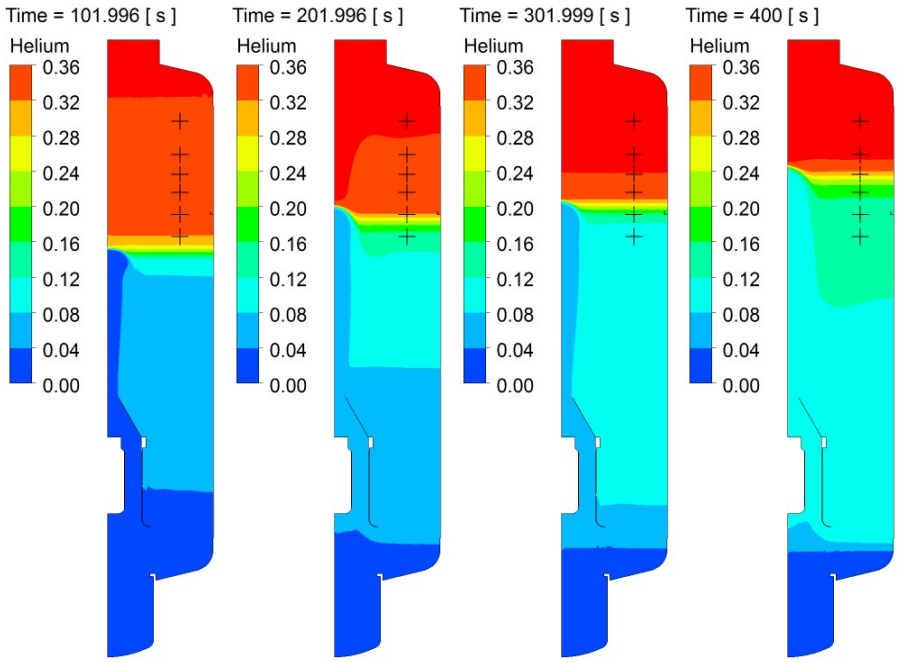

Fig. 72: Helium Mass Fraction of the experimental case with modified buoyancy production term

At 100 seconds the jet contains no helium and faces a steep helium mass fraction gradient. This leads to a low turbulence mass flux. After 200 seconds the jet contains a certain amount of helium. This means a less steep helium gradient and therefore a larger turbulence mass flux. Another reason contributing to the less steep gradient in the region where the maximum turbulence mass flux is located is the broader density layer. This is related to the deformation of the layer in the impact region of the jet into a convex shape.

At 300 seconds the convex shape is less distinct and the helium mass fraction gradient in the interaction region more steep. At the same time the helium concentration in the jet is not yet

increased. This contributes to the steepness of the helium mass fraction gradient. The result is a lower turbulence mass flux.

The situation at 400 seconds is the same than at 200 seconds. A distinct convex shape of the density layer is present and the density layer is even broader than it was at 200 seconds. The helium concentration in the lower vessel and the jet is higher due to the advanced state of the mixing process.

Modification of C_{4Y}

The second modified coefficient to be used is C_{4Y} which controls the pressure-scalar gradient correlation. The investigation of the steady case showed that the best results can be obtained with $C_{4Y}=0.3$. Using this value in the steady case leads to an increase of the turbulence scalar fluxes and a better agreement of the flow field of the large eddy simulation.

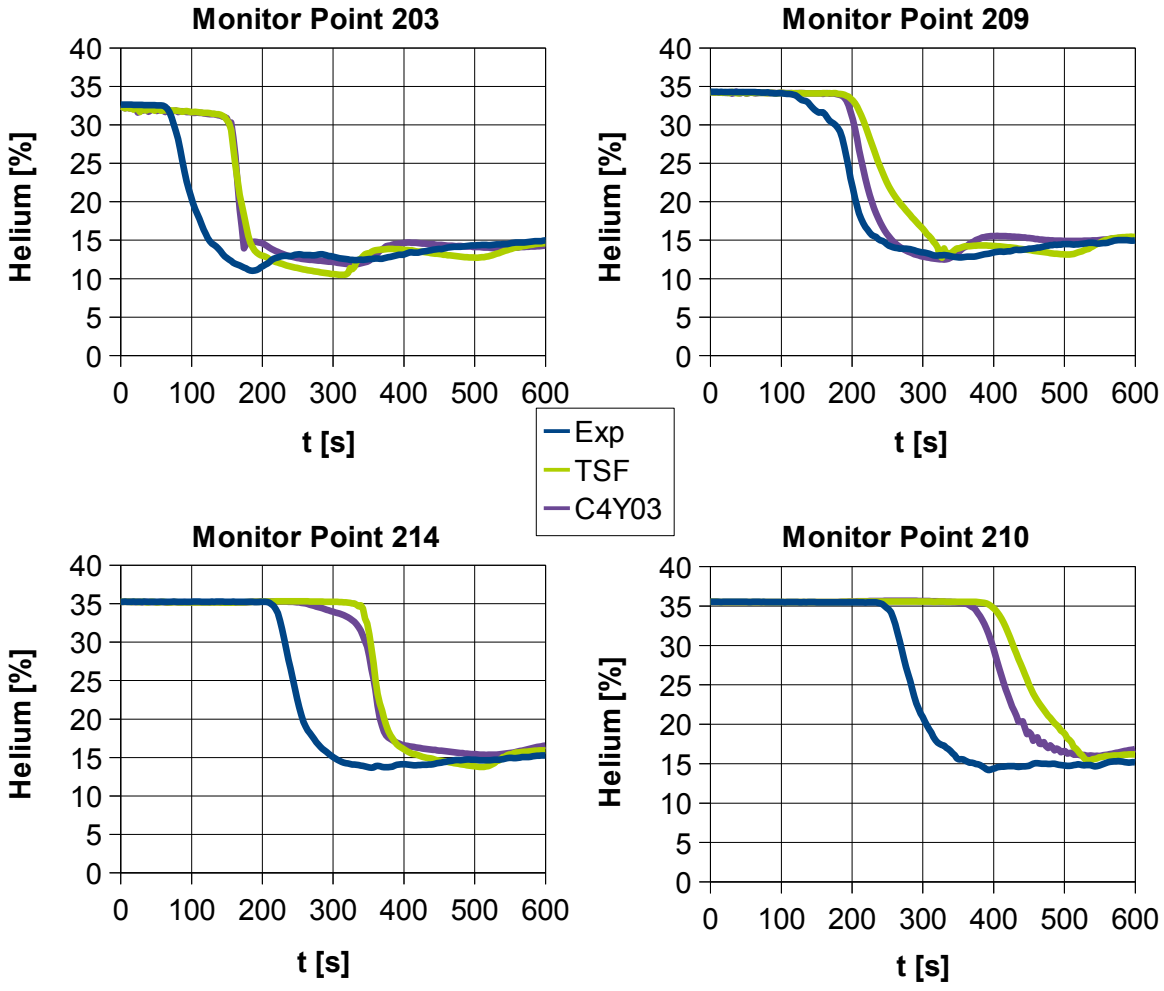

Fig. 73: Helium Concentration at different Monitor Points; Experiment ↔ TSF ↔ C_{4Y} = 0.3

The result of the experimental case with the modified C_{4Y} can be seen in Fig. 73. At monitor point 203 no considerable improvement can be observed. The mixing at monitor point 209 shows a good agreement with the experiment, but the mixing starts at the same time than with the original C_{4Y}. At monitor point 214 the mixing is again similar to the original TSF model coefficient $C_{4Y}=0.0$.

The comparison of the TSF model with the original model coefficients and the eddy diffusivity model showed that the effect of the better mixing capabilities of a model becomes larger with a longer calculated transient. This is true as well for the result of the modified pressure-scalar correlation term. The mixing curve at monitor point 210 shows that a considerable improvement of the mixing time can be obtained with $C_{4Y}=0.3$ compared to the original value of $C_{4Y}=0.0$. The better agreement of $C_{4Y}=0.3$ with the experimental data at monitor point 209 is due to the steeper mixing curve at that point. The mixing started at the same time than with $C_{4Y}=0.0$ but the mixing gradient is similar to the measured one. The result at monitor point 210 shows a qualitatively similar mixing curve for both simulations and the experimental data. The improvement with the use of $C_{4Y}=0.3$ is the earlier start of the mixing which leads to a better agreement with the experiment.

Comparison and Combination of C_{3Y} = 0.0 and C_{4Y} = 0.3

A comparison of the helium concentration over the time at monitor points 203, 209, 214 and 210 of the experiment and the simulations with $C_{3Y}=0.0$ and $C_{4Y}=0.3$ is shown in Fig. 74. The mixing curves of both simulations are similar at monitor point 203. At monitor point 209 the helium concentration starts to decrease at the same time, but the mixing happens faster with $C_{4Y}=0.3$. At monitor point 214 and 210 the curves of the simulations are again pretty close to each other, with a slightly different shape. The mixing with $C_{4Y}=0.3$ is faster than with $C_{3Y}=0.0$ at monitor point 210.

Fig. 75 shows a comparison of the helium concentration over time at monitor point 210 of $C_{4Y}=0.3$, $C_{3Y}=0.0$, the combination of both modified model coefficients and the result obtained with the original values $C_{3Y}=0.55$ and $C_{4Y}=0.0$. The improvement of the mixing because of the modification to the model coefficients can be seen. The unmodified TSF model needs the most time for the mixing. A faster mixing is possible with the use of $C_{3Y}=0.0$. A slight improvement towards a faster mixing can be achieved with the use of $C_{4Y}=0.3$.

So far the results of the investigation of the steady case have been confirmed by the simulations of the experimental case. The TSF model yields a significant improvement over the eddy diffusivity model. The mixing with $C_{3Y}=0.0$ is better than with the original model coefficients and the mixing with $C_{4Y}=0.3$ is better than with $C_{3Y}=0.0$. The combination of both modifications to the final values leads to the best result in the steady case. The helium concentration curve at monitor point 210 (Fig. 75) shows that the final values improve the mixing compared to all other TSF model coefficient variations.

The transient behaviour of the maximum turbulence mass flux obtained with the final model coefficients compared to the result of $C_{3Y}=0.0$ can be seen in Fig. 76. The final model

coefficients yield a higher turbulence mass flux. This leads to the better agreement with the experimental data.

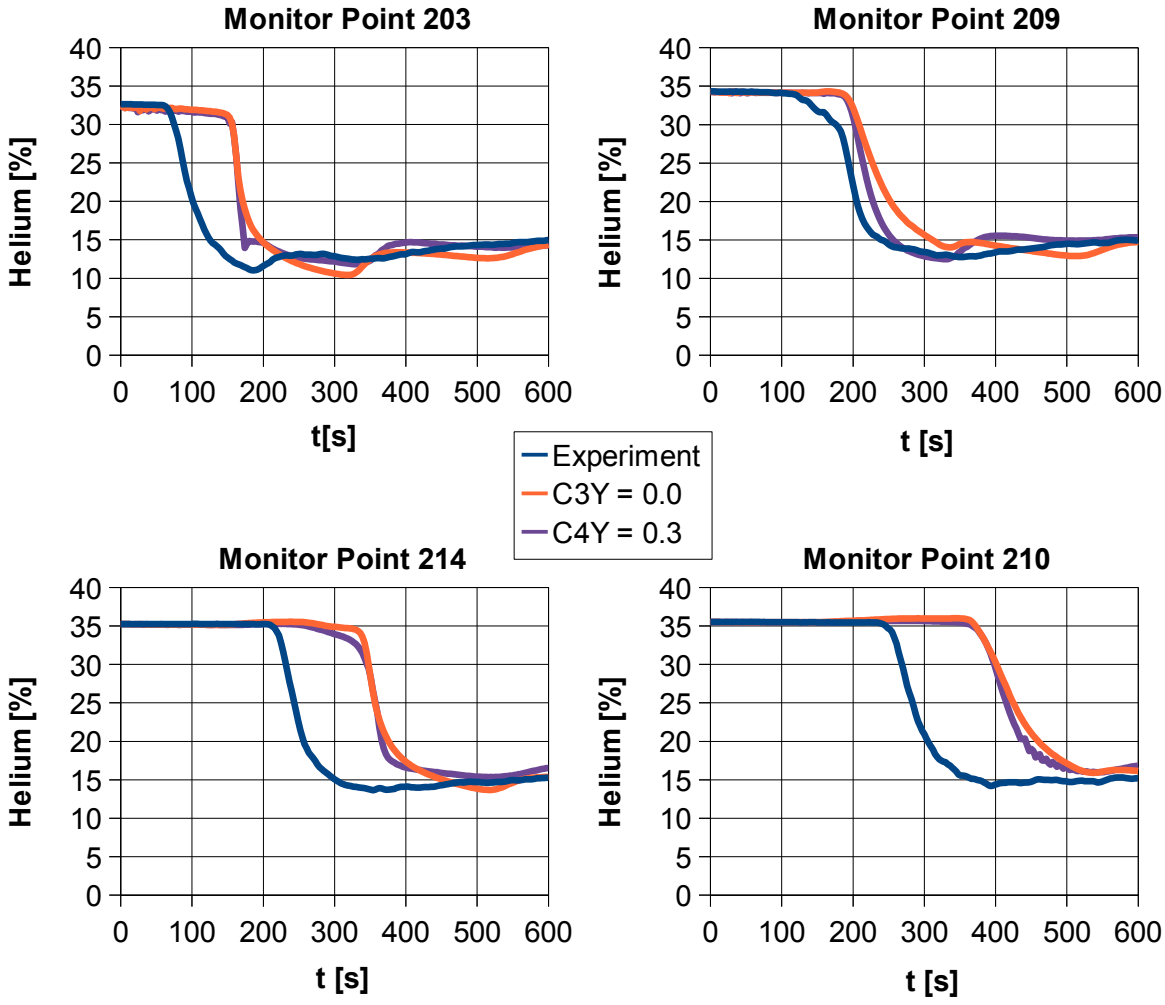

Fig. 74: Helium Concentration at different Monitor Points; Experiment ↔ $C_{3Y} = 0.0$ ↔ $C_{4Y} = 0.3$

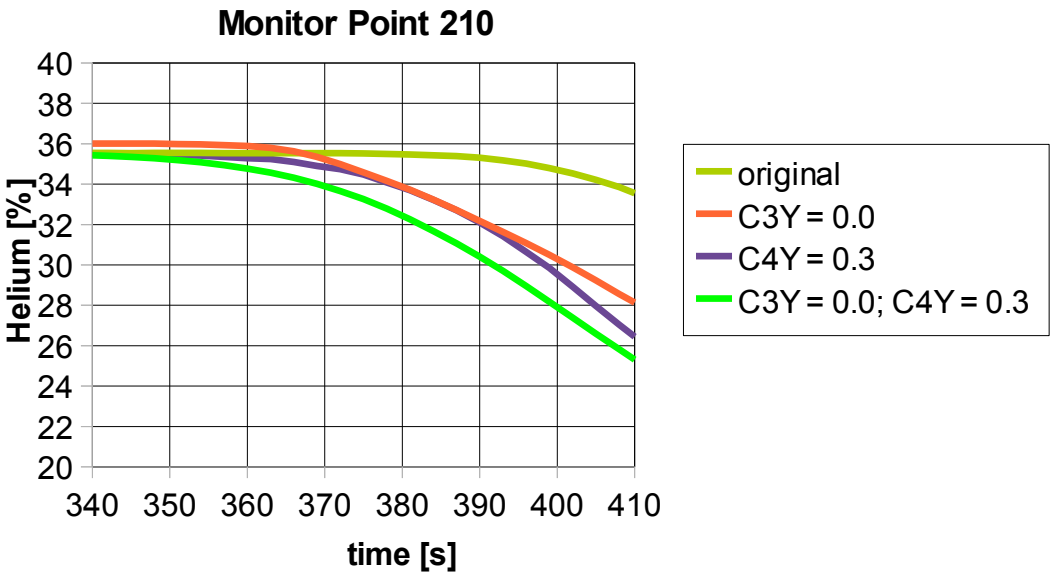

Fig. 75: Improvement of the mixing with the modified model coefficients

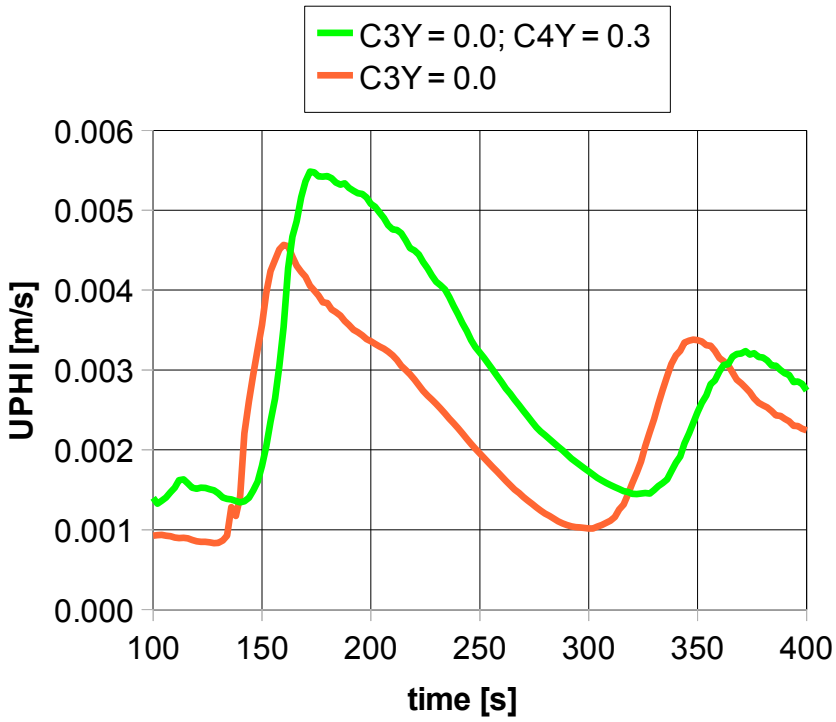

Fig. 76: Maximum turbulence mass flux over time

5 Summary and Conclusions

To contribute to the improvement of the safety analysis of light-water reactors, the aim of this study was to improve the capability of computational fluid dynamics methods to predict the mixing of a stable stratification with a free jet. The specific investigated flows were one phase flows of helium and air. The helium is a replacement of the hydrogen of the loss of coolant accident in the experimental case. This replacement was made because of safety concerns of the experimenters.

Previous numerical investigations showed a shortcoming of CFD codes to correctly predict the mixing of a stable stratification. The incapability of the turbulence model to consider the non-isotropy of such a stratification was identified as the reason for the poor results. While the Reynolds stress model is capable to calculate non-isotropic Reynolds stresses, a similar model for the turbulence mass flux was not yet available. This work was successfully using the non-isotropic turbulence scalar flux model to enhance the Reynolds stress model.

Conclusions of the Steady State Investigation – LES

The analysis of the transient effects of the LES showed a periodic, see-saw like movement of the density layer. The time of one period is approximately one second. It was observed that the movement of the layer has a fixed direction despite the symmetric geometry and boundary conditions. The reason for the direction of the density layer movement was the grid. The geometry is rotational symmetric, but the grid is not. Because a block structured O-grid was used, the calculation grid has four symmetry planes, two through the corners of the inner square black and two through the middle of its sides. The density layer movement follows the symmetry planes though the corners. The region of the movement of the layer is approximately 20% of the height of the integration domain, between $z \approx 0.61$ m and $z \approx 0.84$.

The analysis of the physical values of the LES showed the interaction of the jet and the stable stratification. Originating from the air inlet, the jet flows straight to the density layer. Without the impact of the jet, the layer would be plain. The interaction of the jet and the layer forces a convex shape on the layer and causes the redirection of the jet. Because the jet is compressing the layer, a steeper density gradient is the result of the impact of the jet. This makes the stratification more stable and eventually hinders the jets further upward advancing. Since the jet can not continue vertically it is now flowing horizontal, compressing the now convex-shaped density layer also in horizontal direction. This in turn makes the horizontal density gradient in that region steeper which again keeps the jet from further advancing in that direction. Eventually the jet is forced to flow downwards and to the wall, forming a triangle with the density layer. Downward is the only remaining flow direction unaffected by density

gradients.

The mixing itself during the redirection process happens because the jet is in-taking a very small amount of helium during the first impact at the place where the helium mass fraction gradient of the stable stratification is steepest. The jet contains now some helium and is moving to a region where the gradient of the stratification is less steep. The helium inside the jet contributes to a less steep mass fraction gradient between jet and stratification. Since the gradient is less steep and the stratification therefore less stable, the jet can intake more helium. The main flow is also more tangential to the density layer in this region. Therefore the shear-stresses of the main flow can better contribute to the mixing.

Conclusions of the Steady State Investigation – TSF

The helium mass flow out of the domain was first considered to be a simple parameter to judge the mixing in addition to the turbulence mass flux. The reason for this assumption was that the helium outflow is expected to be larger with a better mixing . It turned out that this assumption was not correct. The helium outflow is affected by the flow situation in the lower part of the domain. Many results of the RANS simulations show a large swirl in the lower part there which is an obstacle for the helium outflow. The modification of C_{4Y} showed that the helium outflow increases with a decreasing strength of the swirl. The modification of C_{3Y} showed a stronger swirl for greater values of the model coefficient, but no notable impact on the helium outflow could be observed. The best agreement with the helium outflow of the large eddy simulation can be obtained with the final values $C_{3Y}=0.0$ and $C_{4Y}=0.3$. The final values yielded also the best agreement with the flow field of the LES.

The modification of C_{3Y} showed that the turbulence mass flux becomes larger with a greater influence of the buoyancy production. The largest turbulence mass fluxes can be obtained with the maximum consideration of the buoyancy production term ($C_{3Y}=0.0$). The modification of C_{4Y} showed an increase of the turbulence mass flux with an increasing value for C_{4Y} up to a maximum for $C_{4Y}=0.3$. Increasing C_{4Y} more results first in a sharp decrease of the turbulence mass flux and to stability issues with the solver. The largest turbulence mass flux and therefore the best agreement with the large eddy simulation can be obtained with the final values $C_{3Y}=0.0$ and $C_{4Y}=0.3$.

The results of the modification of the model coefficients showed that the modification of the influence of the buoyancy production term leads to an overall better agreement with the LES. The modification of the pressure-scalar gradient correlation led to an even greater improvement of the results than the modification of the buoyancy production term with the exception of the helium outflow. The combination of the best values for each model coefficient to the final values $C_{3Y}=0.0$ and $C_{4Y}=0.3$ was yielding the overall best agreement with the large eddy simulation.

Conclusions of the Experimental Case Investigation

The first step of the investigation of the experimental case with the TSF model was a simulation with the original model coefficients and a comparison with the eddy diffusivity model and the experimental data. The eddy diffusivity model shows the expected large

discrepancy to the experimental data. It was observed, that a longer calculated transient leads to a larger discrepancy. The accumulation of the under-prediction of the mixing of the eddy diffusivity model was identified as the reason for this effect. Using the turbulence scalar flux model was yielding a significant improvement of the mixing. Here the positive effect of the TSF model became more clear with a longer calculated transient. However, the TSF model was still under-predicting the mixing.

Simulations were performed with the modified values of the model coefficients for the buoyancy production term and the pressure-scalar gradient correlation that yielded the best agreement with the large eddy simulation in the steady case. The results confirmed the outcome of the steady state investigation. The use of $C_{3Y}=0.0$ led to an improved mixing. A slightly better mixing than with $C_{3Y}=0.0$ could be obtained with $C_{4Y}=0.3$. Finally, the combination of both values was capable of a further improvement of the mixing and consequentially to the best agreement with the experimental data. The reason for the improved mixing is the increase if the turbulence mass flux with the modification of the model coefficients.

Lessons Learned of the TSF Model Investigation

It turned out that the results obtained with the steady case can also be observed for the experimental case. In the steady case the mixing of the large eddy simulation is better than the mixing obtained with the turbulence scalar flux model. The value used to judge the mixing quality of the steady case is the turbulence mass flux. The mixing of the TSF model can be improved with a modification of certain model coefficients. In the investigation of the experimental case the measured mixing is better than the simulated mixing with the TSF model. In the experimental case the quality of the mixing is judged by the mixing time since no turbulence measurement data is available.

Although the use of the TSF model leads to a significantly improved result compared to the eddy diffusivity model, there is still room for improvement. Additional modifications of model coefficients can be investigated using the steady case. The focus for doing this must be the increase of the turbulence mass fluxes and the correct representation of the flow field. Especially the swirl in the lower part of the integration domain, which was observed in the result of some simulations, must be considered.

Designing a theoretical, two-dimensional steady state test case with much smaller dimensions than the experimental case was beneficial for this work. A deep insight into the physics of the mixing of a stable stratification with a free jet was possible with the large eddy simulation of the steady state. Especially the access to values that are difficult to measure, like the turbulence mass fluxes, is a great advantage of this approach. It would be reasonable to make similar theoretical test cases to investigate other flow phenomena.

Laboratory scale experiments can also be beneficial for the investigation and development of turbulence models. Given a proper dimension analysis separated large scale phenomena can be investigated with representative small scale cases, as pointed out in this work. An advantage of a laboratory scale experiment is the better accessibility of the flow with measurement equipment.

Outlook

A further improvement of the capabilities of the TSF model to calculate the mixing of a stable stratification with a free jet is desirable. The modification of the buoyancy production term towards more production led to an improved mixing. Since the buoyancy production term contains the variance, an investigation of the transport equation of the variance and its two model coefficient could yield an improvement.

The rotational symmetry of the transient averaged results of the LES makes the two-dimensional modelling approach of the steady case reasonable. In addition, a three-dimensional calculation is not desirable due to the expensive calculations that are related with it. But another possibility to improve the prediction of the mixing is a further investigation of the impact of three-dimensional effects on the mixing, especially the layer movement. For a detailed investigation of the layer movement, different test cases should be considered. This includes different geometries and different angles between density layer and impinging free jet.

A next step towards the simulation of accident scenarios inside a containment of a light-water reactor would be the inclusion of steam. This makes the modelling of volume condensation necessary, because it can be expected that the water droplets will have an influence on mixing processes.

Bibliography

[1] "The History of Nuclear Energy", U.S. Department of Energy, Office of Nuclear Energy, Science and Technology, DOE/NE-0088

[2] C. Weßelmann, W. Tromm, T. Linnemann and M. Koch: "Kernenergie", BWK, vol. 62 No 5, Sonderdruck zur Jahresausgabe 2010, Springer-VDI-Verlag, Düsseldorf 2010

[3] "Kernenergie Weltreport 2009", atw, vol. 54, No. 4, pp. 271-275, 2010

[4] "Climate Change and Nuclear Power", IAEA/PI/A72E 00-02779, 2000

[5] "Nuclear Safety Review for the Year 2008", IAEA/NSR/2008, 2009

[6] "Der Reaktorunfall in Tschernobyl", Informationskreis KernEnergie, Berlin, 2007

[7] J. Lamarsh and A. Baratta: “Introduction to Nuclear Energy”, Prentice-Hall, New Jersey, 2001

[8] H.-J. Allelein, S. Arndt, W. Klein-Heßling, S. Schwarz, C. Spengler and G. Weber: "COCOSYS: Status of development and validation of the German containment code system", Nuclear Engineering and Design, vol. 238, pp. 872-889, 2008

[9] H.-J. Allelein, K. Neu and J.P. Van Dorsselaere: "European Validation of the Integral Code ASTEC (EVITA) First experience in validation and plant sequence calculations”, Nuclear Engineering and Design, vol. 235, pp. 285-308, 2005

[10] I. Kljenak, M. Babic, B. Mavko and I. Bajsic: "Modelling of containment atmosphere mixing and stratification experiment using a CFD approach”, Nuclear Engineering and Design, vol. 236, pp. 1682-1692, 2006

[11] M. Houkema, N.B. Siccama, J.A. Lycklama and E.M.J. Komen: "Validation of the CFX4 CFD code for containment thermal-hydraulics", Nuclear Engineering and Design, vol. 238, pp. 590-599, 2008

[12] "International Standard Problem ISP-47 on containment thermal hydraulics Final Report", Nuclear Energy Agency, NEA/CSNI/R(2007)10

[13] T. Kanzleiter, A. Kühnel, K. Fischer, M.Heitsch and B.Schramm: "Technical Report THAI Blower Test TH 20", Report No. 150 1325 – TH20, Gesellschaft für Reaktorsicherheit, Köln, 2007

[14] R. Zboray and D. Paladino: "Experiments on basic thermal-hydraulic phenomena relevant for LWR containments: Gas mixing and transport induced by buoyant jets in a multi-compartment geometry", Nuclear Engineering and Design, 2010

[15] D. Paladino, R. Zboray, P. Benz and M. Andreani: "Three-gas mixture plume inducing mixing and stratification in a multi-compartment containment", Nuclear Engineering and Design, vol. 240, pp. 210-220, 2010

[16] D. Paladino, R. Zboray and O. Auban: "The panda tests 9 and 9bis investigating gas mixing and stratification triggered by low momentum plumes", Nuclear Engineering and Design, vol. 240, pp. 1262-1270, 2010

[17] T. Bandurski, M. Huggenberger, J. Dreier, C. Aubert, F. Putz, R.E. Gamble and G. Yadigaroglu: "Influence of the distribution of noncondensibles on passive containment condenser performance in PANDA", Nuclear Engineering and Design, vol. 204, pp. 285-298, 2001

[18] M. Adreani, D. Paladino and T. George: "Simulation of basic gas mixing tests with condensation in the PANDA facility using the GOTHIC code", Nuclear Engineering and Design, vol. 240, pp. 1528-1547, 2010

[19] M. Adrani and D. Paladino: "Simulation of gas mixing and transport in a multi-compartment geometry using the GOTHIC containment code and relatively coarse meshes", Nuclear Engineering and Design, vol. 240, pp. 1506-1527, 2010

[20] O. Auban, R. Zboray and D. Paladino: "Investigation of large-scale gas mixing and stratification phenomena related to LWR containment studies in the PANDA facility", Nuclear Engineering and Design, vol. 237, pp. 409-419, 2007

[21] M. Scheuerer, M. Heitsch, F. Menter, Y. Egorov, I. Toth, D. Bestion, S. Pigny, H. Paillere, A. Martin, M. Boucker, E. Krepper, S. Willemsen, P. Muhlbaueh, M. Andreani, B. Smith, R. Karlsson, M. Henriksson, B. Hemstrom, I. Karppinen and G. Kimber: “Evaluation of computational fluid dynamic methods for reactor safety analysis (ECORA)”, Nuclear Engineering and Design, vol. 235, pp. 359-368, 2005

[22] F. Menter: "CFD Best Practice Guidelines for CFD Code Validation for Reactor-Safety Applications", EVOL-ECORA_D01, 2002

[23] M. Andreani, K. Haller, M. Heitsch, B. Hemström, I. Karppinen, J. Macek, J. Schmid, H. Paillere and I. Toth: “A benchmark exercise on the use of CFD codes for containment issues using best practice guidelines: A computational challenge” Nuclear Engineering and Design, vol. 238, pp. 502-513, 2008

[24] E. Studer, J. Brinster, I. Tkatschenko, G. Mignot, D. Paladino and M. Andreani: "Interaction of a light gas stratified layer with an air jet coming from below: large scale experiments and scaling issues", proceedings of the CFD4NRS-3 workshop, 2010

[25] D. Paladino, M. Andreani, R. Zboray and J. Dreier: "Towards a CFD-grade database addressing LWR containment phenomena", proceedings of the CFD4NRS-3 workshop, 2010

[26] E. Studer, J.P. Magnaud, F. Dabbene and I. Tkatschenko: "International standard problem on containment thermal-hydraulics ISP47 Step 1- Results from the MISTRA exercise", Nuclear Engineering and Design, vol. 237, pp. 536-551, 2007

[27] I. Tkatschenko, E. Studer and H. Paillere: "MISTRA Facility for Containment Lumped Parameter and CFD Code Validation: Example of the International Standard Problem ISP47", Proceedings of the International Conference Nuclear Energy for New Europe, Bled, Slovenia, September 5-8, 2005

[28] M. Povilaitis and Egidijus Urbonavicius: "Simulation of MASPn Experiments in MISTRA Test Facility with COCOSYS Code", Science and Technology of Nuclear Installations, 2008

[29] E. Porcheron, P. Lemaitre, A. Nuboer, V. Rochas and J. Vendel: "Experimental investigation in the TOSQAN facility of heat and mass transfer in a spray for containment application", Nuclear Engineering and Design, vol. 237, pp. 1862–1871, 2007

[30] S. Mimouni, J.-S. Lamy, J. Lavieville, S. Guieu and M. Martin: “Modelling of sprays in containment applications with A CMFD code”, Nuclear Engineering and Design, vol. 240, pp. 2260–2270, 2010

[31] M. Babic, I. Kljenak and B. Mavko: "Simulations of TOSQAN containment spray tests with combined Eulerian CFD and droplet-tracking modelling", Nuclear Engineering and Design, vol. 239, pp 708–721, 2009

[32] J. Kim, U. Lee, S.-W. Hong, S.-B. Kim and H.-D. Kim: “Spray effect on the behaviour of hydrogen during severe accidents by a loss-of-coolant in the APR1400 containment”, International Communications in Heat and Mass Transfer, vol. 33, pp. 1207–1216, 2006

[33] S. Kudriakov, F. Dabbene, E. Studer, A. Beccantini, J.P. Magnaud, H. Paillere, A. Bentaib, A. Bleyer, J. Malet, E. Porcheron and C. Caroli: “The TONUS CFD code for hydrogen risk analysis: Physical models, numerical schemes and validation matrix”, Nuclear Engineering and Design, vol. 238, pp. 551–565, 2008

[34] J. Malet, E.Porcheron and J.Vendel: “J. Malet Nuclear Engineering and Design. 10.1016/j.nucengdes.2010.05.061OECD International Standard Problem ISP-47 on containment thermal-hydraulics—Conclusions of the TOSQAN part ”, Nuclear Engineering and Design, 2010

[35] M. Babic, I. Kljenak and B. Mavko: "Simulation of Containment Atmosphere Mixing and Stratification Experiment in the THAI Facility with a CFD Code", Proceedings of ICAPP, Reno, USA, June 4-8, 2006

[36] A. Zirkel, G. Doebbener and E. Laurien: "CFD simulation of forced flow within the THAI model containment", Proceedings of the 17th International Conference on Nuclear Engineering, Brussels, Belgium, July 12-16, 2009

[37] M. Heitsch, R. Huhtanen, Z. Téchy, C. Fry, P. Kostka, J. Niemi and B. Schramm: “CFD evaluation of hydrogen risk mitigation measures in a VVER-440/213 Containment”, Nuclear Engineering and Design, vol. 240, pp. 385–396, 2010

[38] N. Rajaratnam: “Turbulent Jets”, Elsevier, New York, 1976

[39] R.A. Antonia and Q. Zhao: "Effect of initial conditions on a circular jet", Experiments in Fluids, vol 31, pp. 319-323, 2001

[40] G. Xu and R.A. Antonia: "Effect of different initial conditions on a turbulent round free jet", Experiments in Fluid, vol 33, pp. 677-683, 2002

[41] W.R. Quinn: "Upstream nozzle shaping effects on near field flow in round turbulent free jets", European Journal of Mechanics B/Fluids, vol. 25, pp. 279–301, 2006

[42] J. Mi, G.J. Nathan and D. S. Nobes: "Mixing Characteristics of Axisymmetric Free Jets From a Contoured Nozzle, an Orifice Plate and a Pipe", Journal of Fluids Engineering, vol. 123, pp. 878-883, 2001

[43] J. Mi, P.Kalt, G.J. Nathan and C.Y. Wong: "PIV measurements of a turbulent jet issuing from round sharp-edged plate", Experiments in Fluids, vol. 42, pp. 625-637, 2007

[44] T. Malmström, A. Kirkpatrick, B. Christensen and K. Knappmiller: "Centreline velocity decay measurements in low-velocity axisymmetric jets", Journal of Fluid Mechanics, vol. 246, pp. 363-377, 1997

[45] H. Fellouah, C.G. Ball and A. Pollard: “Reynolds number effects within the development region of a turbulent round free jet”, International Journal of Heat and Mass Transfer, vol. 52, pp. 3943–3954, 2009

[46] Yan Antoine, Fabrice Lemoine and Michel Lebouché: “Turbulent transport of a passive scalar in a round jet discharging into a co-flowing Stream”, European Journal of Mechanics B/Fluids, vol. 20, pp. 275–301, 2001

[47] H. Mahmoud, W. Kriaa, H. Mhiri, G. Le Palec and P. Bournot: "A numerical study of a turbulent axisymmetric jet emerging in a co-flowing stream", Energy Conversion and Management, vol. 51, pp. 2117–2126, 2010

[48] H. Wilkening, D. Baraldi and M. Heitsch: "CFD simulations of light gas release and mixing in the Battelle Model-Containment with CFX", Nuclear Engineering and Design, vol. 238, pp. 618–626, 2008

[49] P. Wang, J. Fröhlich, V. Michelassi and W. Rodi: "Large-eddy simulation of variable-density turbulent axisymmetric jets", International Journal of Heat and Fluid Flow, vol. 29, pp. 654–664, 2008

[50] H. Foysi, J. Mellado and S. Sarkar: "Large-eddy simulation of variable-density round and plane jets", International Journal of Heat and Fluid Flow, vol. 31, pp. 307–314, 2010

[51] K.K.J. Ranga Dinesh, A.M. Savill, K.W. Jenkins and M.P. Kirkpatrick: “LES of intermittency in a turbulent round jet with different inlet conditions”, Computers & Fluids, vol. 39, pp. 1685–1695, 2010

[52] T. Almeida and F. Jaberi: "Large-eddy simulation of a dispersed particle-laden turbulent round jet", International Journal of Heat and Mass Transfer, vol. 51, pp. 683–695, 2008

[53] B. J. Boersma, G. Brethouwer and F. T. M. Nieuwstadt: “A numerical investigation on the effect of the inflow conditions on the self-similar region of a round jet”, Physics of Fluids, vol. 10, pp. 899-909, 1998

[54] B. Chernyavsky, T.C. Wu, F. Peneau, P. Benard, P. Oshkai and N. Djilali: “Numerical and experimental investigation of buoyant gas release: Application to hydrogen jets”, International Journal of Hydrogen Energy, 2010

[55] M.F. El-Amin: “Non-Boussinesq turbulent buoyant jet resulting from hydrogen leakage in air”, International Journal of hydrogen energy, vol. 34, pp. 7873-7882, 2009

[56] M.M. Scase, C.P. Caulfield, S.B. Dalziel and J.C.R. Hunt: “Time-dependent plumes and jets with decreasing source strengths”, Journal of Fluid Mechanics, vol. 563, pp. 443–461, 2006

[57] G.N. Ivey, K.B.Winters and J.R. Koseff: "Density Stratification, Turbulence, but How Much Mixing?", Annual Review of Fluid Mechanics, vol. 40, pp. 169–184, 2008

[58] K. Noto: “Dependence of heat island phenomena on stable stratification and heat quantity in a calm environment”, Atmospheric Environment, vol. 30, pp. 475-485, 1996

[59] K. Noto and K. Nakai: "Direct Numerical Simulation of Turbulent Thermal Plume in Stably Stratified Ambient: Formulation, Numerical Methodology, Reverse Transition, Relaminarization, and Turbulent Enhancement", Numerical Heat Transfer, Part B: Fundamentals, vol. 53, pp. 313-357, 2008

[60] J.R. Taylor, S. Sarkar and V. Armenio: "Large eddy simulation of stably stratified open channel flow", Physics of Fluids, vol. 17, pp. 116602-1-116602-18, 2005

[61] B. Galperin, S. Sukoriansky and P. Anderson: "On the critical Richardson number in stably stratified turbulence", Atmospheric Science Letters, vol.8, pp. 65–69, 2007

[62] D. Stretch, J. Rottman, S. Venayagamoorthy, K. Nomura and C. Rehmann: "Mixing efficiency in decaying stably stratified turbulence", Dynamics of Atmospheres and Oceans, 2009

[63] S. Sarkar: "The Effect of Stable Stratification on Turbulence Anisotropy in Uniformly Sheared Flow", Computers and Mathematics with Applications, vol. 46, pp. 639-646, 2003

[64] Y. Lin and P. Linden: "The entrainment due to a turbulent fountain at a density interface", Journal of Fluid Mechanics, vol. 000, pp. 1-28, 2005

[65] E. Laurien and H. Oertel jr.: "Numerische Strömungsmechanik", 3. Auflage, Vieweg+Teubner, Wiesbaden, 2009

[66] Y. Zhu: "Numerical Investigation of the Flow and Heat Transfer within the Core Cooling Channel of a Supercritical Water Reactor", Universität Stuttgart, 2010

[67] A. Zirkel and E. Laurien: "Investigation of the Turbulence Mass Transport During the Mixing of a Stable Stratification with a Free Jet using CFD-Methods", Proceedings of the CFD4NRS-3 workshop, Washington D.C., USA, 14-16 September, 2010

[68] T. Szirtes and P. Rozsa: "Applied Dimensional Analysis and Modelling", vol. 2, Elsevier, 2007

[69] B. Bird, W. Stewart and E. Lightfoot: "Transport Phenomena", John Wiley & Sons, New York, 1960

[70] H. Siekmann and P. Thamsen: “Strömungslehre”, vol. 2, Springer, Berlin, 2008

[71] W. Rodi: Turbulence Models and Their Application in Hydraulics, A state-of-the-art review", vol 3, A.A. Balkema, Rotterdam, 1993

[72] D. Wilcox: Turbulence Modelling for CFD, vol. 2, DCW Industries, La Canada,2004

[73] W.P. Jones and D. Lentini: "A realisable non-linear eddy viscosity/diffusivity model for confined swirling flows", International Journal of Heat and Fluid Flow, 2008

[74] F. Menter: "Two-Equation Eddy-Viscosity Turbulence Models for Engineering Applications", AIAA Journal, vol. 32, pp. 1598-1605, 1994

[75] E. Laurien and T. Wintterle: "On the numerical simulation of flow and heat transfer within the fuel-assembly of the high-performance light-water-reactor", Proceedings of the KTH-Workshop on modelling and measurements of two-phase flows and heat transfer in nuclear fuel assemblies, Stockholm, Sweden, 10-11 October, 2006

[76] C. Speziale, S. Sarkar and T. Gatski: "Modelling the pressure-strain correlation of turbulence: an invariant dynamical systems approach", Journal of Fluid Mechanics, vol. 227, pp. 245-272, 1991

[77] W. Rodi: "Examples of calculation methods for flow and mixing in stratified fluids", Journal of geophysical research, vol. 92, pp. 5305-5328, 1987

[78] J. Fröhlich: "Large Eddy Simulation turbulenter Strömungen", Teubner, Wiesbaden , 2006

[79] R. Fox and A. McDonald: “Introduction to Fluid Mechanics", vol 3, John Wiley & Sons, New York, 1985

[80] ANSYS CFX User Documentation

[81] C. Shannon: "Communication in the Presence of Noise", Proceedings of the IEEE, vol. 86, no 2, 1998

[82] H. Lüke: "The origins of the Sampling Theorem", IEEE Communications Magazine, April 1999

[83] P. Bergé and M. Dubois: “Rayleigh-bénard convection”, Contemporary Physics, vol. 25 no. 6, pp. 535-582, 1984

Appendix

A1 Boundary Conditions

Reference density for buoyancy treatment	$0.179 \frac{kg}{m^3}$
Gravity constant	$9.81 \frac{m}{s^2}$
Initialization and reference pressure	$1.168\,\text{bar}$
Initialization temperature	$24.3\,°C$
Momentum source of the experimental case	$10.43 \frac{kg}{m^2 s^2}$
Inlet velocity of the steady case	$2 \frac{m}{s}$

A2 CFX Customized Solver

The customised solver used for the simulations with the TSF model is a CFX 12 solver executable compiled for a 64 bit Linux operating system which is commonly used by high performance computing clusters.

To use the customised solver, several environment variables have to be set.

- export CFX=/path/to/CFX
- export SOLVERDIR=/path/to/customised_solver_folder
- export OS_LOCALE=linux-amd64
- export CFX5_CCL_LIBS=$SOLVERDIR/RULES:$SOLVERDIR/VARIABLES: $CFX/etc/execrules.ccl
- export SOLVER=$SOLVERDIR/linux-amd64/double/solver-pvm.exe

The variable $SOLVER is a convenient shortcut to the double precision solver. To start a parallel run the path to the solver executable has to be given twice, for the solver and for the partitioner.

- cfx5solve -def <definition-file>.def -solver $SOLVER -partitioner $SOLVER

To use the TSF model an additional step is necessary. The definition file has to be edited manually. This is done by adding several lines to the CCL (CFX command language) part of the definition file. First, the CCL has to be extracted:

- cfx5cmds -def <file>.def -text <file>.ccl -read

The resulting <file>.ccl is a text file and can be edited with a text editor. To activate the TSF model, the lines

```
TURBULENT FLUX CLOSURE:
  Option = Transport Equation
END
```

have to be added in the components section for the passive scalar.

```
FLOW:
  DOMAIN: Fluid
    FLUID MODELS:
      COMPONENT: He
        Kinematic Diffusivity = 7.35E-5 [m^2 s^-1]
        Option = Transport Equation
        TURBULENT FLUX CLOSURE:
          Option = Transport Equation
        END
      END
    END
  END
END
```

Access to the different models of the customised solver is available through the user section. In the first section the four different modelling options have to be set true (t) or false (f). The relevant lines are “SolveTSFYVAR” for the general activation of the TSF model with the variance and “BuoyancyProdTSF” to enable the buoyancy production terms in the TSF transport equations. The model coefficients are also set in the user section of the CCL.

```
USER:
  SolveTSFYVAR = t
  BuoyancyProdTSF = t
  UseChassaingTDF = t
  UseScalarFluxesInTDF = t
  TSFCoefficientC1Y = 2.9
  TSFCoefficientC2Y = 0.4
  TSFCoefficientC3Y = 0.55
  TSFCoefficientC4Y = 0.0
  TSFCoefficientCY = 0.15
  TSFCoefficientCYY = 0.2
  TSFCoefficientC1YY = 1.0
END
```

Two values have to be set in the expert parameters section. The transient initialisation override has to be set to true because the customised solver only supports trivial initial conditions. It was necessary for the steady case to define the pressure as static pressure. This is done with the pressure value option set to 3.

```
  EXPERT PARAMETERS:
    pressure value option = 3
    transient initialisation override = t
  END
```

Institut für Kernenergetik und Energiesysteme

Universität Stuttgart

Pfaffenwaldring 31

70550 Stuttgart